Technische Universität München
Physik Department

Master's Thesis in Physics

Mechanical Design and Shielding against Optical Photons for the ComPol-ISS In-Orbit-Verification Mission

Mechanisches Design und Abschirmung optischer Photonen für die ComPol-ISS In-Orbit-Verifizierungsmission

Katrin Geigenberger

June 23, 2022

Max Planck Institute for Physics

First Examiner: Prof. S. Mertens
Second Examiner: Prof. Oberauer

Contents

Abstract

In-Orbit-Verification (IOV) missions are conducted to demonstrate the proper function and reliability of a novel space application operated in the harsh space environment: vacuum, high energy particles, and particularly intense solar radiation.
Nowadays, IOV missions of larger satellites are often conducted with CubeSats, which are small satellites of standardized shape and size. In contrary, the ComPol project, will fly the final science mission on a CubeSat. It will carry a Compton telescope to measure the X-ray polarization of the black hole binary Cygnus X-1. The degree and plane of the polarization depends on the X-ray generation mechanism and can therefore distinguish between underlying geometrical models, that match the spectral observations of the source equally well.
ComPol-ISS, the IOV mission of this CubeSat telescope will be conducted on an external platform aboard the International Space Station (ISS) in 2023. A scaled-down version of the instrumentation will be operated together with essential parts of the future CubeSat bus. The detector system is comprised of Silicon Drift Detectors (SDDs) and a scintillation crystal, read out by an array of Silicon Photomultipliers (SiPMs). Both, SDDs and SiPMs, are highly sensitive to even a low background of optical photons. With an average solar intensity of 1370 W/m^2, a shielding strategy against optical photons is essential for the success of the IOV mission.

The focus of this thesis was to design the first mechanical model for ComPol-ISS, that meets all space-constraints, while addressing the background of optical photons. For the first time all individual components were combined into a single CAD model. The assembly approach of the resulting stacked setup was verified with a 3D-printed mock-up. It is space-compatible and in principle ready for production. Even though a change of the design is decided for the future implementation, most of the current design solutions can be reused. This also includes the multi-staged light mitigation, whose central component is a dedicated aluminum housing around the detectors. This detector light shield was evaluated and improved in an iterative design loop, eliminating the light leaks. The final version is able to suppress the light of a laboratory LED to 1.3% above the dark rate, however, it is not light-tight for the illumination with 34% of the solar intensity. While all previously addressed leak sources are confirmed to stay light tight, the PCBs themselves are identified to be the major leakage source, resulting in an excess of 66.1%. By covering the PCB face, the relative light excess is reduced to 4.7%. It needs to be evaluated in the future, if the all light shielding components together result in a reasonable low excess or if the PCB must be shielded by additional means.

Chapter 1

The ComPol Project

ComPol, short for **Com**pton **Pol**arimeter, is a planned 3U-CubeSat mission to perform a long-term measurement of the black hole binary Cygnus X-1 in the hard X-ray range. During the mission, the CubeSat will focus on Cygnus X-1 for at least one year to reach a sensitivity on the degree of polarization of 13% [1], what matches the expected level of $\lesssim$20% for energies below 400 keV [**Laurent2011**, 2]. The instrument components are engineerd by research groups of the Max-Planck-Institute for Physics (MPP) in München, the Technical University München (TUM), the Commissariat à l'énergie atomique (CEA) in Paris, the RadLab at the Politecnico di Milano (Polimi), and the Laboratory for Rapid Space Missions (LRSM) of the TUM in Garching, funded by the ORIGINS excellence cluster at the TUM.
An adaptation of the instrument is currently being prepared for an In-Orbit-Verification (IOV) mission on an external platform aboard the International Space Station (ISS) in 2023 with the main goal to prove the functionality and durability of the instrument in the space environment of a low earth orbit (LEO). To better distinguish between this prototype and the final CubeSat version, which will carry an up-scaled instrument compared to the IOV mission, it is called **ComPol-ISS**. The focus of this thesis is the mechanical implementation of ComPol-ISS. The key aspect of the hardware design is the shielding concept against optical photons in order to protect the sensitive detectors.

This Chapter provides an overview of the ComPol project, starting with a discussion of Cygnus X-1 (section 1.1), including previous observations, physical models and how ComPol can add to solve scientific questions. This will be followed by an introduction to both the ComPol and the ComPol-ISS mission (section 1.2).

1.1 Scientific Motivation

A black hole binary (BHB) consists of a stellar mass black hole (BH) and its binary companion, orbiting each other. Typically, the BH has a mass from a few solar masses to tens of solar masses $M_\odot$ [3]. The second object can either be a star, or a compact object like a white dwarf, neutron star or a second black hole.

When the companion is a star and comes close enough to the BH, the envelope of the star is attracted by the BH and forms an accretion disk. The gravitational potential energy of the stellar gas gets converted into kinetic energy as it moves inward, and the frequent particle collisions due to the high density creates an environment where various processes can lead to the production, scattering and emission of X-rays. Thus, BHBs with an accreting stellar companion are often detected by their X-ray emission and are then referred to as BH X-ray binaries (BHXB) [3].
Cygnus X–1, which belongs to the brightest X-ray sources in the sky [4], was the first binary system with evidence for a black hole [5]. It is located in the Swan constellation (Latin: Cygnus) and has a distance of ∼1.9 kpc from Earth (determined by trigonometric parallax [6]). The most likely values for the masses of the BH and its companion, the blue supergiant star *HDE 226868*, are 27 and 16 $M_{\odot}$, respectively [7]. Their orbital period is 5.6 days [8].
Today, Cygnus X-1 is well studied over the whole electromagnetic band, including simultaneous multi-wavelength observations (e.g., with radio telescopes). These observations give insights into the highly dynamical behavior of BHXBs and serve as a basis for the development of physical accretion models and the complex interplay between the system's geometry and X-ray emission. These models are, however, not sufficient yet to clearly distinguish between the partially competing models, which will be described in subsection 1.1.3.
For compact objects, like BHBs, it is hardly possible to use direct imaging to obtain geometrical information about the sources. Instead all knowledge must be extracted from observations of spectra, variability and polarization. At the same time, many factors need to be considered to create a complete description of BHXBs. Thus, the extension of the dataset and the combination of different observation types is of key importance to address the remaining questions and gain an even better understanding of BHXBs.

The ComPol instrument will address this task with simultaneous spectroscopic and polarimetric observations, being sensitive in the energy range from 20 keV - 2 MeV and 20 keV - 300 keV respectively [1] (more on this energy range in section 2.1). So far, hardly any polarization measurement has been performed in the range from 20 keV to 200 keV. This and the strong, persistent nature of Cygnus X-1, makes it not only the optimal target for a small CubeSat telescope like CubeSat, but also a specifically interesting test for the current models.

1.1.1 The Emission States of BHXBs

BHBs are known to be highly variable objects. Most BHXBs are transient objects, meaning that they have occasional X-ray outbursts. Cygnus X-1 however, is one of a few BHXBs, that show persistent X-ray emission [9]. Both, transient and persistent sources are observed to change between emission states, that show characteristic spectral and temporal behavior [3, 9]. Prominent states[1] of accreting BHXBs are the high/soft state (HSS), the low/hard state (LHS), and diverse intermediate states (IS). Figure 1.1 shows typical spectra of Cygnus X-1 in these states, including the projected sensitivity range of the ComPol instrument highlighted in yellow and orange. ComPol's sensitivity starts at 20 keV and will record spectra of the full hard region and parts of the high energy tail. The polarization measurement will cover the maximum of the low/hard state. The terms high and low refer to the luminosity

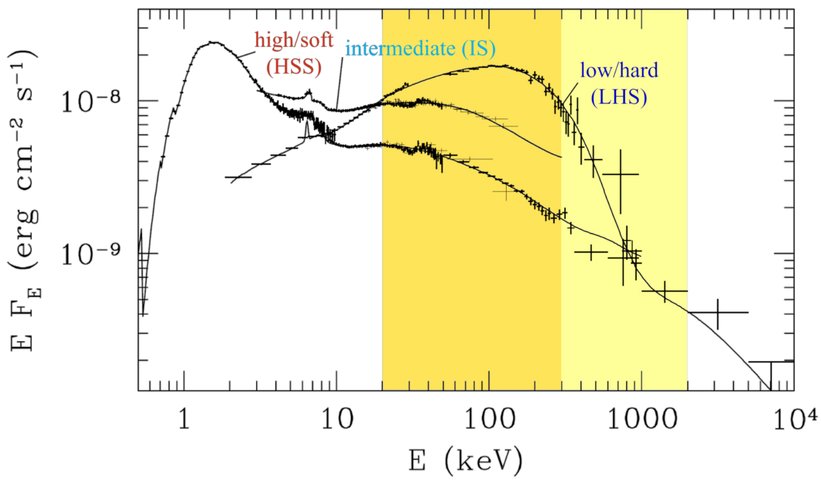

Figure 1.1: *Typical spectra of Cygnus X-1 in the high/soft state (HSS, red), intermediates state (IS, cyan) and low/hard state (LHS, blue). The marked areas highlight the projected ComPol sensitivity for spectral (20 keV - 2 MeV, yellow) and polarimetric (∼20 keV - 300 keV, orange) measurement. Adapted from [10].*

of the states, whereas soft and hard refer to the dominant energy range of the X-ray emission. The intermediate state shows spectra in between the HSS and LHS. It is observed in times of state transitions and therefore also called transitional state. However, there are also occurrences of this state, after which the system returns to the initial state. Such observations are interpreted as *failed* transitions [11].

Cygnus X-1 shows a high/soft state with a maximum emission between 1-2 keV and a low/hard state peaking at ∼100 keV. All three states can be characterized as a weighted combination of three main spectral features: A low energy part (up to a

[1] There are more types of states that are well described together with the observed transitions and distinction markers of the states in *Chapter 3.5: Definitions of Source States* of [9]. They are more important for the characterization of transient sources, but occasionally also appear in publications about Cygnus X-1.

breaking energy $E_{break} \sim 10$ keV) represented by a power law with soft spectral index Γ_1, a high energy part described by a power law with a harder spectral index Γ_2, and a hard exponential tail for energies > 400 keV [1, 11, 12]. Together, they form the empirical *broken power law with exponentially cutoff* model and describe the observed spectra quite successful, when adding a Gaussian Fe Kα fluorescence line at ~6.4 keV [11]. The physical models of the spectra will be discussed in subsection 1.1.3.

1.1.2 State Classification Methods

It is important to note, that the spectra shown in Figure 1.1 are archetypes and that the actual populations of the respective states show a continuous variation in intensity and hardness. Two diagrams are typically applied for the classification of BHXBs states and will be explained in the following:

1) Hardness-Intensity Diagram (HID): The total intensity (alternatively count rate) is plotted against the hardness ratio, which is the ratio of counts in two different energy bands. Here, two spectral characteristics are compared.
The upper panels of Figure 1.2 show examples of HIDs. On the left the data of ~5 years of Cygnus X-1 observations by MAXI (Monitor of All-sky X-ray Image, onboard the ISS) are forming two rather distinct state populations in the HID [13]. On the right, ~9.5 years of Cygnus X-1 observations by RXTE-PCA (Proportional Counter Array, onboard the Rossi X-ray Timing Explorer) are shown in a HID together with RXTE-PCA observations of the transient BHXB GX 339-4 for comparison [9]. Here, the Cygnus X-1 data (gray circles) create more of a continuous spread from the hard to the soft regime than in the left HID, but the histogram reveals the presence of two peaks at different hardness that are also correlated with the bend in the HID. Compared with the HID of the transient (black dots) the spread follows the same shape, but Cygnus X-1 never reaches the soft regime. The high/soft states of Cygnus X-1 stay relatively hard and are comparable with the hardness of the intermediate states of the transient sources, which suggests, that the production mechanism of hard X-rays plays a larger role in Cygnus X-1. All transient BHXB are observed to walk trough the HIDs with a hysteresis: Starting in the vertical right branch (low/hard states), moving through intermediate states of high luminosity to the high/soft states on the left and returning back to the low/hard states by crossing the intermediate regime with lower luminosity. For Cygnus X-1 no hysteresis was observed, what could be a feature of its persistent nature. Weaker outbursts of transients show smaller hysteresis and the comparably slow accretion rate of Cygnus X-1 could result in an immeasurable small hysteresis [9].

2) Hardness-RMS Diagram (HRD): The fractional RMS (root mean square/mean) of the observation quantifies how strong the observed light curve

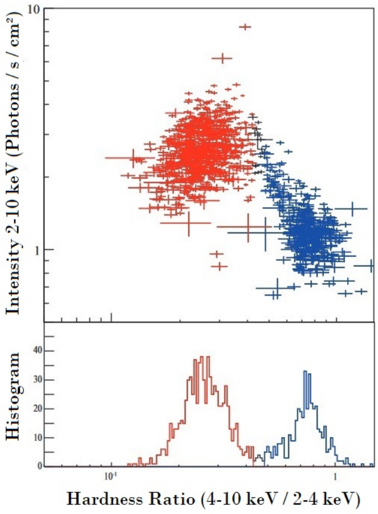

(a) *HID with hardness histogram of Cygnus X-1. States are colored: HSS (red), IS (black), LHS (blue).*

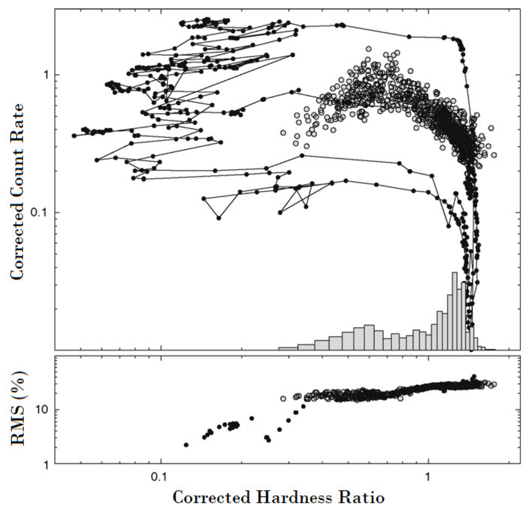

(b) *HID (top) and HRD (bottom) of GX 339-4 (black dots) and Cygnus X-1 (gray circles), with hardness histogram for Cygnus X-1.*

Figure 1.2: *Examples of the two fundamental diagrams for state classification: The Hardness-intensity diagram (HID) and the hardness-RMS diagram (HRD). The hardness ratio is defined as the ratio of counts in two distinct energy bands. The RMS is the fractional root mean square of the time variability, calculated for a chosen frequency and energy range. (a) shows the HID with hardness histogram of Cygnus X-1 data, observed between August 2009 and September 2014, by the MAXI mission, aboard the ISS. The color labels the state, in this case defined on basis of the histogram. Adapted from [13]. (b) is a HID combining all RXTE-PCA observation of Cygnus X-1 between February 1996 and October 2005, plotted over the HID of the GX 339-4 outburst from 2002/2003, corrected to bring the source to the same distance as Cygnus X-1. It is shown together with the HRD of both sources and the hardness histogram for Cygnus X-1. Adapted from [9]*

fluctuates on average and is plotted against the hardness ratio. Here, a spectral characteristic is compared with a temporal one.
The RMS is a function of the timescale (frequency of the variation) and the photon energy. The timescale-dependency of the variations is typically analyzed by means of a power spectral density (PSD), which is essentially the squared Fourier coefficients[2] of equally binned time sections of the observed light curve (for mathematical definition, see [14]). Showing the signal portion carried by each frequency component,

[2] Typically renormalized by frequency.

PSD plots reveal different timing features of the different BHXB states. For an instructive comparison of PSDs for the three states see [15].
Mostly used, however, is the RMS averaged over a broad frequency range, building the basis for HRDs. With this method it is possible to reveal timing features of the individual states, like in the bottom panel of Figure 1.2 (b). Here, the RMS of Cygnus X-1 experiences a kink around the change from its hard to its soft regime[3], just as the data of the transient source. The difference however is that Cygnus X-1 does not show the strong RMS drop seen for intermediate and soft range of the transients, but maintains a high variability even for its softest states.

For the exact boundaries between the states various definitions exist on the basis of these diagrams, their individual parameters or mapping of against with parameters from spectral models timing analysis. Some of those are heavily instrument-specific, others require a deep understanding of spectral modeling and they are all slightly inconsistent with each other [12].
The most simplistic approach was taken by Sugimoto et al. (2016) [13] on the HID shown in Figure 1.2 (a), fitting Gauss distributions to the hardness histogram and defining the boundaries of the HSS and LHS states to the intermediate regime as 3σ from the gaussian center. This and similar approaches, however, face the risk of overlooking physical differences of the transitional regime. They require a large sample of observations and well enough separated spectral properties, that are not necessarily given (see the less clear separation in the hardness histogram of Figure 1.2 (b)).

A sophisticated method, that can be translated to single observations of other instruments, was developed by Grinberg et al. (2013) [12] and was since then widely used. The method makes use of the distinct timing behavior in the different states. Namely, a change of temporal properties (i.e., the fractional RMS) was found to correlate with specific values of the soft photon index Γ_1 of the empirical broken power law fit. These Γ_1 values were subsequently used as boundaries to define the states of all available observations by RXTE-PCA, which is an instrument sensitive to a wide energy band [16], and thus allows the fitting of the broken power law (to extract Γ_1). Grinberg et al. then combine the classified individual pointed observations with long-term observations of multiple all-sky monitors (RXTE-ASM, Swift-BAT, MAXI and Fermi-GBM), that lack the spectral sensitivity for the broken power law fit. Observations of these instruments, that were taken at the same time (or nearly at the same time) as the Γ_1-classified pointed observations, inherited this classification and were compared with all non-simultaneous observations of the same instrument in terms of spectral parameters. They find that for these instruments

[3] Although hard to see on the log-scale since the RMS of Cygnus X-1 is in the range of 15-40%. For a better plot to see the RMS spread of Cygnus X-1 see [12] figure 3.

neither intensity nor hardness alone are sufficient to safely discriminate between the states, but define instument-specific cuts (i.e., location within the HID) on the basis of minimizing the contamination of Γ_1-classified states. The separation of low/hard and intermediate states stays difficult and is only possible with the method when the used all-sky-observation includes data below 5 keV [12].

Most importantly, the classification method remains useful even beyond the decommissioning of RXTE in 2012, since it can be transferred to other observations in two ways still today:
1) Direct Γ_1-classification: Find the Γ_1 values by fitting the observed spectra with the empirical exponentially cut-off broken power law model, and apply the Γ_1-boundaries found for Cygnus X-1 (Γ_1). For this approach spectral data of a wide energy range is necessary.
2) Indirect all-sky classification: Classify data with simultaneous (or quasi-simultaneous) all-sky observations by applying the HID/spectral parameter cuts. This approach requires (quasi-)simultaneous observations from MAXI, Swift-BAT or Fermi-GBM. [4]. This was for example used to classify the high energy observations of the IBIS instrument aboard the INTEGRAL satellite [2, 17].

For ComPol, like for IBIS, the direct Γ_1-classification is not applicable, since that would require spectral data below $E_{break} \sim 10$ keV. Where (quasi-)simultaneous all-sky observation are available the classification of ComPol data can be performed by the indirect approach. For all other data, it will be necessary to investigate the population in the HID and HRD including a comparison of the behavior of the all-sky-classified data, to find instrument-specific classification cuts for ComPol.

The full power of this classification method is shown in Figure 1.3: Whenever Cygnus X-1 is in the field of view of the respective all-sky monitors, it provides a continuous long-term view on the state evolution of Cygnus X-1, allowing matching of individual observations as well as statistical analysis. The complete dataset as of 2013, for example, revealed that the LHS is the most stable state of Cygnus X-1 with a probability of more than 85% for staying in that state more than one week, followed by the HSS with about 75% probability. The intermediate states are rather short-lived with a stability in the range of days and a 50% probability that the state changes within three days. Thus it is essential to have a continuous observation to catch short time variability and quick state transitions, which are important to understand the underlying physics of the source.

[4] Separation of hard and intermediate states is only possible with MAXI data

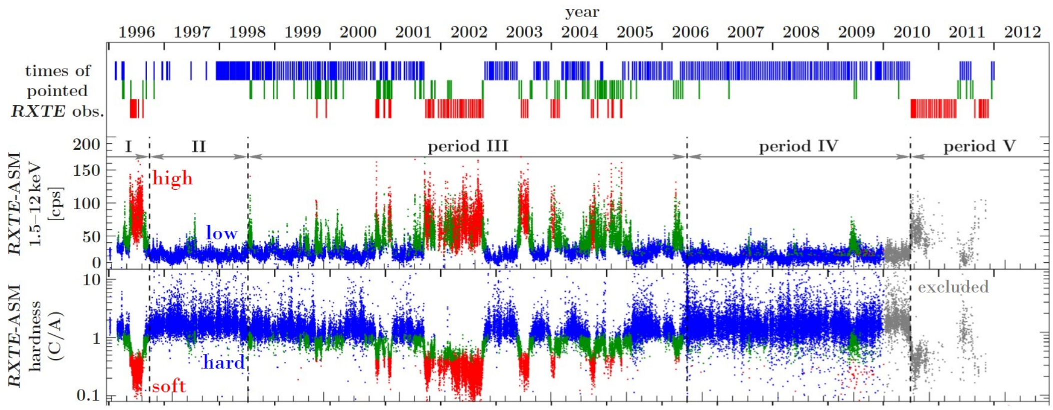

Figure 1.3: *16 years state evolution of Cygnus X-1 on the basis of RXTR measurements. States shown in blue (LHS), green (IS) and red (HSS). Adapted from [12].* ***Upper panel:*** *States obtained directly from Γ_1 fits of the spectra of individual pointed observations of the RXTE-PCA instrument, that is sensitive from 2 - 60 keV [16].* ***Lower two panels:*** *Light curves of the ASM instrument, classified by cuts on count rate and hardness ratio. Here, defined with the count rates in band C (5.0 - 12 keV) and band A (1.5 - 3.0 keV). Grey plotted data starting 2010 remained unclassified due to the instrumental decline during the end of the instrument's lifetime.*

1.1.3 X-ray Generation Mechanism and State Dependent Models

The empirical behavior of the spectra can be recreated by several physical processes with the main being thermal emission, synchrotron radiation and inverse Compton scattering [1]. In the following, these processes and their implications for the models of the state spectra are discussed, focusing on the energy range where ComPol will be sensitive. For the high energy tail ($<$ 400 keV) and polarization measurements of this regime, see subsection 1.1.4.

1) Thermal emission of the disk: The further the stellar gas approaches the BH in the accretion disk, the hotter the gas becomes, until it reaches the innermost stable circular orbit (also ISCO) at a couple Schwarzschild radii[5]. The thermal black body emission of the outer (rather) cold disk centers around a few 100 eV, producing only very soft X-rays [11]. More energetic X-rays are produced in the hotter inner parts of the disk. The temperature of the inner disk is a few keV [1], and thus the peak of the high/soft spectrum can be well described by thermal emission of this 'standard' accretion disk [11]. Models for the low/hard state involves a hot optically thin but geometrically thick sphere of hot plasma, called accretion disk corona (ADC),

[5]Explicit distance depends on the spin of the BH.

hereafter simply corona. This corona partially overlaps and truncates the accretion disk before it can reach the ISCO, what would explain the low intensity in the soft regime. See Figure 1.4 (top) for an illustration of the corona and (bottom) for the standard disk, reaching the direct vicinity of the BH.

2) Inverse Compton scattering: In a hot corona around the BH, soft photons (from the disk or the jet) can perform inverse Compton scattering on thermal electrons. This process is called thermal comptonization. An electron temperature of ∼70 keV fits the observed peak in the low/high state [17], and competes with the proposed synchrotron origin of the high energy part (see below). The radiation from comptonization models is expected to be unpolarized, even if the incident soft photons were polarized, because the multiple scattering that is present in a medium with an optical depth $\tau \geq 1$ will dilute the original polarization [2].
For the high/soft state, models with a hot corona do not fit the data. Geometries without corona as in Figure 1.4 (b) show better agreement [1]. It is however under debate, if a cold corona could be present instead [1]. For the faint but present high energy component of the high/soft state, a possible source would be inverse Compton scattering on free-falling electrons into the BH [18].

3) Synchrotron radiation: When charged particles move on curved trajectories with relativistic speed (e.g., in strong magnetic fields), they emit synchrotron radiation. This radiation has a continuous broadband spectrum with a peaking energy that increases with higher curvature (small radii, strong magnetic field). A characteristic feature of synchrotron radiation is its linear polarization.
One origin of synchrotron emission are **relativistic jets**. Jets are focused beams of particles that do not fall into the BH but instead are accelerated perpendicular to the accretion disk. They produce hard synchrotron radiation in their formation region close to the black hole, where the charged particles are strongly bent by magnetic fields. In the outer region of the jet, softer synchrotron radiation in the radio and infrared energy range are emitted.
Radio telescope observations confirm radio flares during the low/hard state and a radio peak in the beginning of the transition from the hard to the soft region for many sources [2, 19]. For Cygnus X-1, there is a "strong correlation between the 10–50 keV X-ray flux and the radio luminosity" [11], which indicates that these X-rays are originating from synchrotron radiation in the jets. Therefore, ComPol has a good chance to detect a polarization in this energy region.
In the high/soft state the radio emission of Cygnus X-1 drops significantly and also shows phases, where radio emission is reduced below the measurable level [11]. The remaining amount of radio emission can be interpreted as (fading) interactions of jet remnants with the interstellar medium (ISM), while the jet as "core radio emission"

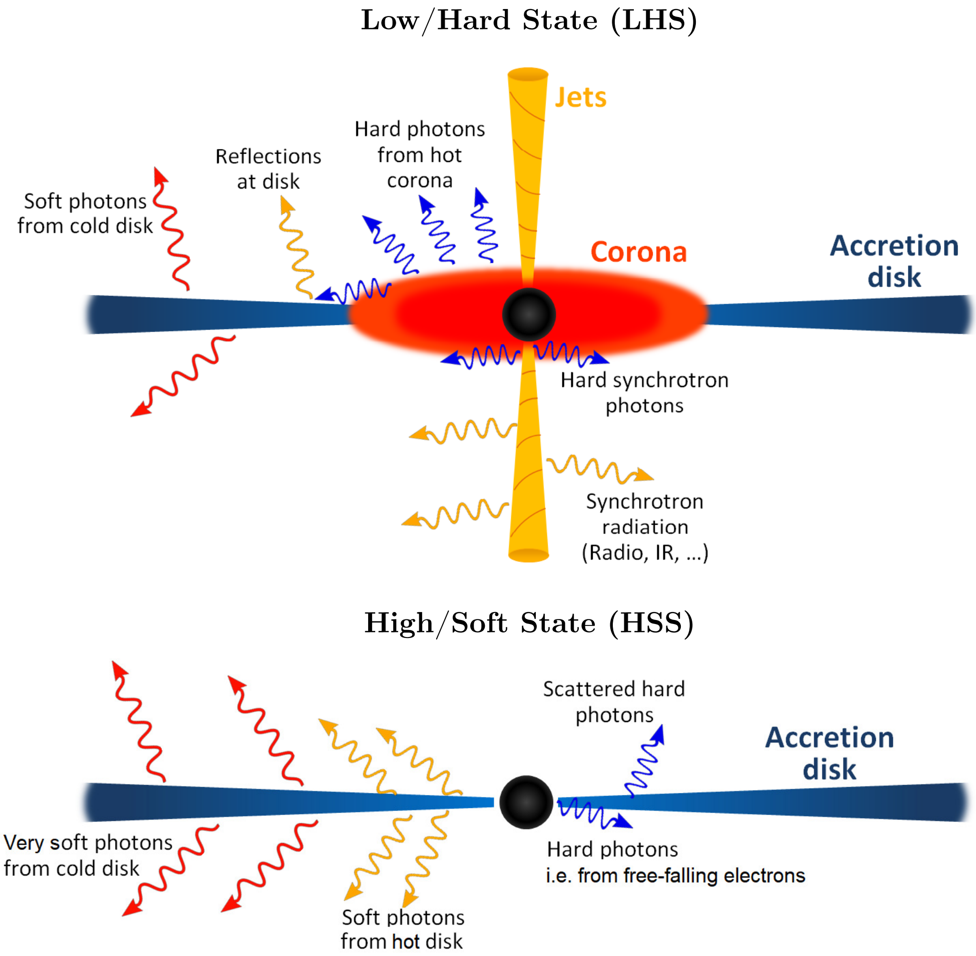

Figure 1.4: *Illustration of two geometry models and their respective X-ray generation mechanisms. The black hole is represented by a black circle in the center, the accretion disk is shown with a thick blue line that gets truncated at a certain radius.*
Low/Hard State (LHS): *The canonical model includes a hot corona, that truncates the disk and reduces the soft contribution. Soft photons from the cold outer disk gain energy by inverse Compton scattering on the hot electron plasma of the corona. Additionally radio jets are observed in the LHS. The environment in the formation region of the jets leads to the generation of hard synchrotron radiation.*
High/Soft State (HSS): *Without the hot corona, the disk can reach closer to the BH, getting hotter, what leads to the dominant soft component in the HSS spectrum. The hard component comes most likely from the central region, e.g., from free-falling and thus accelerating electrons.Illustrations from [1].*

has actually switched off in the soft states, but an intermittent, optically thin, jet is also possible in the soft state. [19]. Fender et al. (2009) state that there is still a "uncertainty about when exactly the jet production mechanism shuts off" that needs to be addressed. Since ComPol will measure the polarization in the 20-50 keV region, it would be able to search for the correlation of polarization from an active formation region (though suppressed in strength) with the presence/absence of radio emission during a soft period, if radio observations will be performed simultaneously. If a change in polarization correlates with the radio luminosity, the faint hard part of the soft spectrum could be explained by a weak jet. If not correlated, an imminent jet is discouraged and the ISM-theory is probably the source of the radio emission.

In summary, the physical models of the high/soft state are dominated by the thermal emission, while for the low/high state there are competing models for the origin of the hard X-ray emission: *Comptonization of soft photons or synchrontron-radiation from relativistic jets?* Both models are compatible with the observations with comparable precision [11] and the dividing signature is presence/ absence of polarization. The two mechanisms are however not mutually exclusive and can be present together, with the question: *How much does each process contribute and is there a dominant one?*

This is a simplified picture and all models suggest a complex interplay between the geometrical features of the BHXB system, which can be disturbed by changes of external parameters like the mass accretion rate and potentially trigger a state transition [11]. Also scattering and reflection of photons on the disk or within a corona plays a role [1]. To understand the BHXB system the models of the X-ray generation mechanism need to involve all these effects. Furthermore they do not only need to fit the individual spectra, but also need to explain the transitions between the spectral states. Therefore the observation of both successful and failed transitions accompanied by the short-lived intermediate states is of key importance. *What causes the transition from one state into another? What is the origin of the fast variability? Why do some transitions get to a halt during the intermediate state and return to the initial state?* Those are just some of the unsolved questions to which ComPol aims to contribute with continuous pointing observations. A state-resolved polarization measurement is of particular interest, as it has the potential to investigate the presence of a jet in the high/soft state and to discriminate between the jet and comptonization models, proposed for the low/hard state. Both models are indeed able to reproduce the low/hard spectra, but have different signatures in the polarization. Already non-state resolved measurements will, however, greatly add to the present data, since that already comprises information on the averaged influence of jet and comptonization models.

1.1.4 Result of Past Polarization Measurements

Due to the decreasing flux above ~400 keV, ComPol will not be sensitive to the polarization of the high energy tail, but be limited to spectroscopy. I this energy region however, a significant polarization was detected, while in the energies below so far only upper limits could be set. Therefore, a brief discussion of the high energy tail follows.
In the energy range above 400 keV, inverse Compton scattering is not efficient anymore and thus another mechanism must be in place that produces this hard X-ray emission. One candidate is the already explained relativistic jet. Probably enhanced trough synchrotron self-Comptonization, where synchrotron radiation Compton-scatters off the electrons that produce the synchrotron radiation in the first place. Other models involve hybrid thermal/non-thermal corona emissions, e.g., [20]. The hard energy tail was observed in both soft and hard states, being detected for the HSS up to at least 500 keV [17]. So, in case these high energies are produced by powerful jets, there is an intrinsic difference to the hard tail of both states, since the HSS radio observations are not consistent with a strong jet but with a trimmed jet, if at all.

However, a strong polarization of ~70% was detected in the high energy tail with the IBIS and SPI instrument [21]. Laurent et al. (2011) also placed an upper limit of 20% on the degree of polarization below 400 keV. A state-resolved re-analysis by Rodriguez et al. (2015), determines the polarization of the low/hard state to be 75% ± 32% above 400 keV, while the high/soft state and the 300–400 keV data of all states were compatible with no or immeasurable small strength of polarization. This indeed suggests a jet in the high state and questions the contribution of a jet in the low state. An upper limit for the 300–400 keV polarization fraction in the low/hard state was given to be 22% [2][6].
Therefore, it is reasonable to assume a similar or slightly lower polarization in the directly adjacent energy region (leq300 keV). With a simulated minimal detectable polarization of 16.8% after half a year of observation time [22], ComPol reaches below these limits. It is senitive up to at least 200 keV, maybe more if enough Compton events are collected, i.e. when the CubeSat livetime is longer than the minimally expected 1 year.

Within the nominal sensitivity region of the ComPol mission ($20 - 200$ keV [1]), the balloon-borne PoGO+ polarimeter placed an upper limit of $\leq 8.6\%$ for the energies from $19 - 181$ keV. This limit is considerably below the polarization sensitivity of ComPol. However, it was given for the whole 162 keV wide energy range with a

[6] The similarity to the result of Laurent et al. is not surprising, since most of the available data was in the low/hard state.

median of 57 keV being in the lower energy region of ComPol's sensitivity. Also, it leaves an window between 181 and 300 keV, where hardly any polarization measurements were conducted. Especially there, ComPol will largely extend the polarization measurements and and maybe even replace the upper limits with the first polarization detection below 400 keV. This eventually could consolidate one of the described models.

1.1.5 Conclusion

Throughout the section various characteristics of the future ComPol data were highlighted. This is not meant to be a comprehensive list but an insight into the potential capabilities of ComPol. Furthermore it is important to understand that depending on the applied state classification technique[7], this discrimination as well as the polarization determination (see **??**) needs a large amount of data in the individual states. Depending on the time which Cygnus X-1 will stay in the respective state, it might be necessary to average over all occurrences of a specific state during the observations by ComPol. Nevertheless, it is not possible to predict the state-variability of Cygnus X-1 during the mission duration and it is possible that the occurrence of a specific state is so rare, especially in the short intermediate and maybe the soft state, that despite averaging, only the hard state accumulates the necessary amount of data for meaningful results.
So it is crucial to make the most out of the observation time of ComPol and to gain the maximal possible statistic. Therefore it is important for the success of the mission to investigate shielding techniques for the best possible reduction of the background of high energy particles (see Master's thesis of Cynthia Glas for background simulations [22]) as well as optical photons, investigated in this thesis (chapter 4).

1.2 The CubeSat Mission for Hard X-ray Polarimetry

Earths atmosphere blocks electromagnetic radiation in the X-ray energy range and thus, for X-ray observations it is necessary to observe at least above the troposphere with high altitude stratosphere balloons or to launch space borne telescopes. In the last decades, this meant to build large and costly satellites for long-term space missions in cooperation with space agencies, which usually carried more than one telescope. Example for these are NASA's CGRO (Compton Gamma Ray Observatory, 1991 - 2000 [23]) satellite and ESA's INTEGRAL (INTErnational Gamma-Ray Astrophysics Laboratory, 2002 - ongoing [24]) satellite, with 4 instrument each.

[7] Using (quasi-)simultaneous all sky measurements, statistical analysis of the grouping/population of spectral properties, or a combination if both.

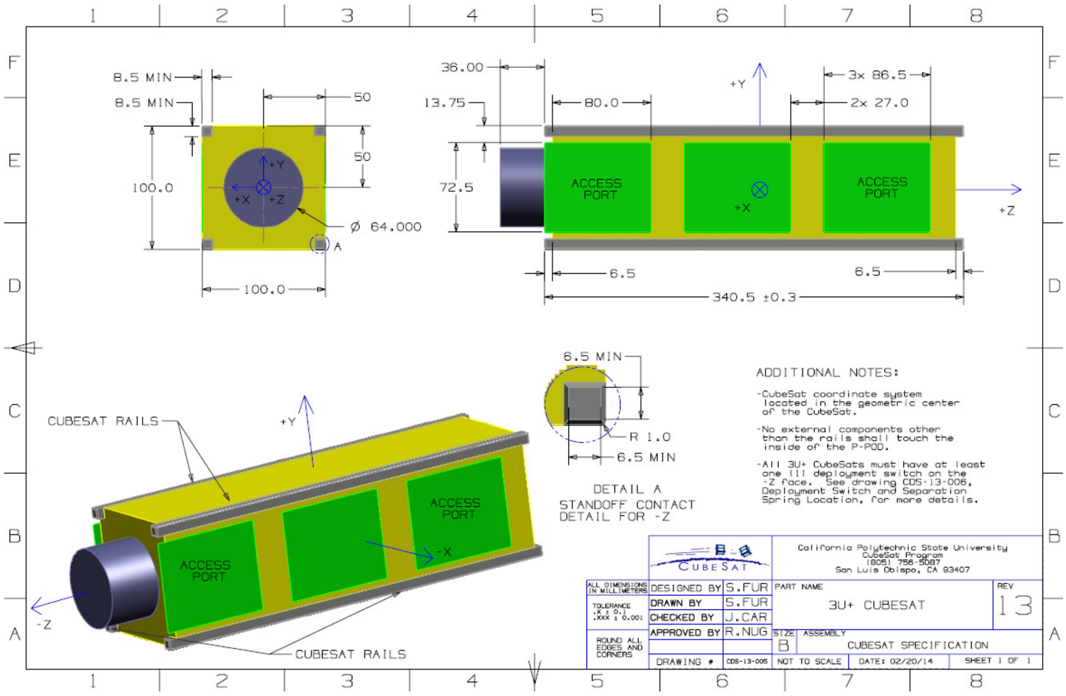

Figure 1.5: *3U+ CubeSat ("Tuna Can") Design Specification Drawing from the CDS Revision 13 [26]. This is a guideline for the early design phase and matches most launch provider. Still the mission-specific requirements can deviate.*

With the current opening of space to economic endeavors ("new space"), this picture has changed. Nowadays, small micro- and nano-satellites are on the rise. Especially CubeSats, which are nano-satellites with a standardized form factor, become increasingly popular. CubeSats are named by how many cube-like units ("U") they combine to one nano-satellite. The current CubeSat Design Specification (CDS) defines generic requirements for CubeSats and currently comprises sizes from 1U to 12U CubeSats. One unit has a volume of 100 x 100 x 113.5 mm^3 and a mass of up to 2 kg as of CDS Revision 14.1 [25]. The CDS also provides dimensional drawings and acceptance check lists to be used for the early phase of CubeSat designs. In Figure 1.5 the specification drawing for the 3U+ CubeSat configuration is shown as an example. This extended variant of the usual 3U CubeSat, offered by some launch providers, allows for an additional cylindrical volume (called "Tuna Can") added to the -Z face of the standard 3U CubeSat volume, while all other dimensions remain.

The drawings and requirements in the CDS are compatible with the majority of CubeSat launch providers. The official set of requirements that are to be met for the launch are defined by the launch provider or mission integrator in the mission-specific interface control document (ICD) and can deviate from the CDS. However, the CDS is written rather conservatively to fit with as many launch opportunities as possible and in some cases will even be more strict than the ICD. So there is a high chance to stay within the ICD requirements when the CDS is fulfilled.

All CubeSats have deployment rails in each corner (in Figure 1.5 they are labeled as CubeSat rails). These rails allow the launch and deployment with standardized CubeSat dispensers. Each dispenser can carry one or multiple CubeSats depending on their respective size and multiple dispensers can be mounted onto one rocket together with a larger satellite (or nowadays with multiple small or medium sized ones). Due to their small size, the availability of components of the shelf (COTS) and frequent launch possibilities, CubeSat missions are much cheaper, have a shorter development time, but are equally capable of performing science missions.

1.2.1 ComPol: The 3U+ CubeSat Compton Polarimeter

In the past the few satellite observatories, that were instrumentally able to detect x-ray polarization, were primarily designed for another goal (e.g., imaging) and their polarimetric performance was relatively limited [27, 28]. Polarization measurements were secondary and for long stayed behind. Though this has just recently changed in the end of 2021 with the launch of NASA's Imaging X-ray Polarimetry Explorer (IXPE) for soft X-rays, polarimetry is only starting to catch up with the comparatively comprehensive spectral observations.
The current dataset of hard X-rays still remains sparse and in the energy gap between ∼180 and 300 keV hardly any polarimetry was yet performed. Even more importantly in the case of Cygnus X-1, the majority of polarization measurements were conducted during the low/hard state, while in the high/soft state only a reduced amount and in the intermediate state no notable amount of data exists [2].

The ComPol project now takes the advantages of CubeSats to bring a dedicated hard X-ray polarimetry mission into orbit that tackles this shortage of polarization data. ComPol is a planned CubeSat mission that carries a Compton telescope of the COMPTEL type (see chapter 2 for instrument description). It will work as a spectrometer and polarimeter simultaneously, covering the energy range of 20 keV - 2 MeV and 20 keV to minimal 300 keV, respectively. Thus it will be able to close the energy gap between ∼180 and 300 keV and enhance the existing database.
The CubeSat will be launched in a few years from now and so far the following three key studies were performed:

1. A first feasibility study (ODYSSEUS Space Inc., 2018) [29]

2. A first sensitivity study (Matthias Meier, 2019) [1]

3. Background, activation and shielding study (Cynthia Glas, 2022) [22]

The above shown volume constraints for a 3U+ CubeSat and the maximal 3U CubeSat weight of 6 kg [25], naturally limit the detector size. The fast and relatively cheap CubeSat approach however allows for a one-source commitment and counterweights the small detection area by exposure time. Opposed to large missions with long target lists, ComPol will focus on Cygnus X-1 at least for one year, probably extending for the full lifetime of the detector. This greatly enhances the chance for the intermediate and soft states to occur during the observation time and adds a long-term component to the dataset.
The feasibility study proposes an orbit of 500 km with a 40° inclination estimates the observational time will be around 64% on average[8]. After a typical detumbling and commissioning phase of one month, a minimal remaining science phase of 11 months would therefore result in ~0.6 years of data. The background and shielding study shows that a summed pointing time of half a year in an orbit with a maximal background contribution from the flight through the SAA and polar regions (550 km altitude, 85° inclination) resulted in a minimal detectable polarization (MDP) between 17.6 and 16.8% with a passive shielding for different materials. If ComPol could stay out of these regions, a MDP of 13.2% would be possible. This however is only possible with an inclination of 0° and a rare orbit for CubeSat launch providers [29]. Instead the option of an active veto shielding is currently being discussed and could lead to a further reduction of the MDP.

A conceptual design as proposed by the feasability study is shown in Figure 1.6 At the current state, around 1 - 1.5U are planned for the ComPol instrument and the other 1.5 - 2 U for the CubeSat bus, consisting of the required satellite subsystems:

- **Attitude Determination and Control System (ADCS):** sensors that read out the position and attitude (e.g., star trackers) and actuators (e.g., reaction wheels, magnetorquer) that control the orientation of the satellite. High pointing accuracy towards Cygnus X-1 is needed and a slow spin of a few revolutions per observation would be optimal to diminish systematic effects in polarization measurement [29]. Thus ADCS is the most critical subsystem for ComPol.
- **Electrical Power Supply (EPS):** generation, buffering and distribution of power. This will involve solar panels, batteries and electrical boards to distribute power and generate instrument-specific voltages.

[8] Day-to-day dependent duty cycle is determined by the occultation of the source as well as SAA-flight-throughs and field-of-view illumination by Sun and Moon.

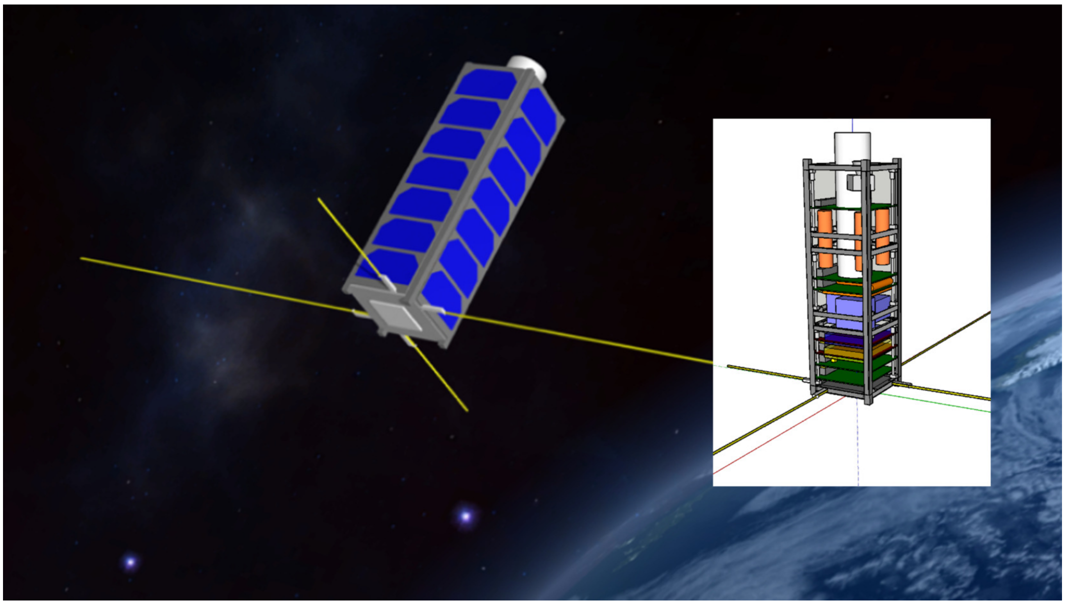

Figure 1.6: *ComPol rendering from feasibility study by ODYDDEUS 02/2018*

- **Communication System (COM):** radio transceiver system for uplink (commanding) and downlink (housekeeping, science data) to the ground station(s). The antenna will unfold after launch and protrude the CubeSat volume.
- **Command and Data Handling (CDH):** processing the command pipeline, and handling of the data (collection, caching and transmission preparation).
- **Thermal Regulation:** keeping the satellite components within thermal operation limits. There is a choice between active and passive regulation.

It is planned to use COTS hardware or present solutions of the LRSM, where possible.

1.2.2 ComPol-ISS: The In-Orbit-Verification Mission aboard the ISS

The first big milestone of the ComPol project is the in-orbit-verification (IOV) of the detector system in 2023. The novel ComPol instrumentation has a rather low, so called, technology readiness level (TRL). This is a measure for the maturity of technology and it plays an important role in spaceflight, specifically in the cost and risk management [30, 31]. The joint operation of a size-reduced ∼1U instrument together with parts of the future CubeSat bus in orbit will mark the first real life demonstration of the ComPol systems in space environment (background radiation, vacuum and thermal cycle). Not only important information for the further development of ComPol will be collected, but the detector system will also gain the status of a flight-proven prototype which is equal to TRL 7, the highest TRL for prototypes [31].

The primary objective of the IOV is to receive and process coincident signals from both detectors. Additional goals are the measurement of a typical low earth orbit (LEO) background, the determination of real real influence of solar, X-ray, and cosmic radiation backgrounds on the detector system and the test of an active anti-coincidence veto. Furthermore, it is the best opportunity to check the long-term survivability of the chosen components.

For an IOV, there are in principle two possible implementations: a precursory CubeSat or a payload on an external platform aboard the ISS. To reduce the overall complexity of the IOV, it was chosen to conduct the IOV aboard the ISS, thus the name ComPol-ISS. Like this, the focus of the IOV mission is the scientific instrumentation of ComPol itself. The design is facilitated and the risk of mission failure is minimized because of the following advantages over a CubeSat-IOV:

- **The ADCS is not critcal** for the success of the IOV mission. Mounted onto an external payload platform, the prototype will be fixed in place and will not control its attitude. The position determination is provided by the ISS. The attitude sensors can be tested and compared to the values provided by the ISS.
- **Sufficient electrical power** is provided at all times. The ISS EPS system takes over the generation and distribution of power to the payloads. Only the system-internal power distribution and generation of high voltage to bias the instrument remains. The total accessible power is considerably greater than the power a CubeSat is typically capable to generates with its own solar cells between the eclipse times. No power shortage due to power-consuming maneuvers like detumbling must be considered.
- **Powerful up- and downlink** via the ISS. No separate COM necessary for the IOV. No risk of mission loss due to communication problems.
- **Launch vibrations and shocks are reduced to a minimum.** Different from the CubeSat dispenser mounted to the launch vehicle, the ISS payloads can be launched soft stowed.
- The center of mass and the **mass distribution is irrelevant.** Since it is no free-floating CubeSat, the moments of inertia need no special care.

The only drawback is, that the telescope will be fixed in the reference system of the ISS and no target pointing is possible. Instead, the instrument will view everything passing the zenith over the ISS. Consequently, no polarization is expected since a signal of random X-rays from various sources is expected to average out in a week or non-existing polarization. If in contrast a significant portion of detected X-rays happen to be polarized, it will be worth to compare the data of current all sky observatories for further information, especially MAXI being an ISS-observatory should should normally be able to provide simultaneous observation and can add spectral information between 0.5-30 keV [32, 33]. The performance of the system can be checked equally well without polarization. Since the IOV instrument has a smaller detector area then the final instrument, it was not the intention of the IOV to contribute to the observation of Cygnus X-1. Instead, ComPol-ISS will result in valuable knowledge about the system and help to further understand the diffuse background of X-rays, cosmic rays and solar radiation that ComPol will have to deal with.

Chapter 2

Introduction to the 'ComPol' Instrument

The ComPol instrument is a CubeSat sized Compton telescope. This type of telescopes uses the well known kinematics of Compton scattering for imaging, spectroscopy and polarimetry. Two famous examples for Compton telescopes are the COMPTEL telescope onboard the Compton Gamma-Ray Observatory (CGRO) [23] and the IBIS (Imager on-Board the INTEGRAL Satellite) instrument onboard the INTEGRAL observatory [24]. The fist part of this chapter will introduce the working principle of Compton telescopes and how they can determine the polarization. Afterwards the detector system and the individual detectors of the ComPol project are discussed, for both the planned ComPol setup and ComPol-ISS implementation.

2.1 Polarimetry with Compton Telescopes

The main types of Compton telescopes have either one detector ("compact" systems, e.g., COSI telescope [34]) or two parallel detectors (e.g., COMPTEL and ComPol), that are sensitive to the energy and position of particle interactions of the incident photon with the detector material. The measurement principle relies on Compton events, in which the incident X-ray first conducts Compton scattering and afterwards is fully absorbed in an second interaction (see Figure 2.2). In the two detector case, the fist detector is called scatterer and the second one absorber or calorimeter. Other particle interactions occur in both detectors as well, and need to be separated from the useful Compton events by cuts based on the kinematics of Compton scattering.

The predominant interaction type of photons depend on their energy and the detector material. The differential cross-sections for a silicon detector are shown in Figure 2.1. In the soft X-ray regime, the majority of photons get absorbed via the photoelectric effect. At higher energies, the production of electron positron pairs is possible and becomes the main effect in the gamma ray range. In between Compton scattering or incoherent scattering is the dominant interaction.

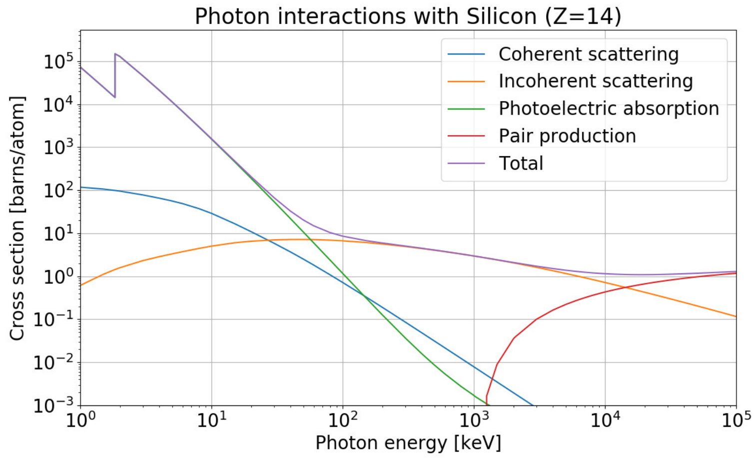

Figure 2.1: ***cross-section of photon interactions with Silicon*** *for the X-ray regime. Compton scattering (here, incoherent scattering because the correction factor is included) is dominant between 100 keV and 10 MeV. Plot taken from [1]. All data has been taken from the XCOM: Photon cross-sections Database [35].*

Compton Scattering is the inelastic scattering of a photon on a free or nearly free electron ($E_{\text{Ionization}} \ll E_{\text{Photon}}$) [36]. For the scattering on a bound electron such as in a detector material, this type of scattering is correctly called incoherent scattering and differs from the free Compton scattering by a correction factor in the differential cross-section, that becomes attenuating for small energies and small scatter angles (more see [1]). However, the effect of incoherent scattering is approximately the same of Compton scattering for a wide energy range and thus is commonly referred to as Compton scattering except of the special cases when the difference to free Compton scattering is highlighted. This naming convention is adopted in this thesis.

The energy that is transferred by the inelastic scattering from the photon to the electron, results in an decreased energy of the outgoing photon $E' = E - E_1$ that is deflected by the scatter angle θ as shown in Figure 2.2. The corresponding wavelength shift $\Delta\lambda$ is linked to the deflection of the photon by the Compton formula:

$$\Delta\lambda = \lambda_C(1 - \cos\theta) \quad \text{with} \quad \lambda_C = h/m_e c \tag{2.1}$$

If subsequently a photoelectric absorption ($E_2 = E'$) occurs, the scattering angle θ can be calculated from the detected energy difference of E_1 and $E = E_2 + E_1$. For an unknown source location a single Compton event results in an annulus of possible origins of the detected X-ray, as depicted in Figure 2.2 and 2.3. For one

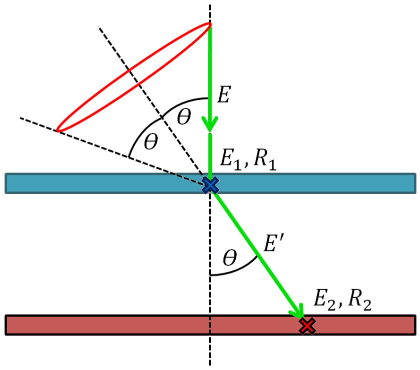

Figure 2.2: ***A Compton event in a two-detector Compton telescope:*** *An incident high energy photon undergoes Compton scattering at position R_1 (blue cross), leaves a small energy E_1 in the first detector and is deflected by the linked scattering angle θ. It is then absorbed in the second detector at position R_2 (red cross), depositing its remaining energy E_2. Determination of the angle θ from the measured energies results in an origin cone. Figure taken from [1].*

X-ray source and perfect detectors, one would need exactly three Compton events to determine the position of the source and perform imaging observation. For real world detectors and additional off-source particles, only a significant number of detected Compton events allows to pin down the location of the source, as it is illustrated by the red circles in Figure 2.3. The so far described detector system is actually a Compton camera and would observe the entire solid angle of 4π (including all background photons). To function as a directional Compton telescope, it is necessary to add background suppression by means of a focusing optics (e.g., a collimator) and shielding towards the other directions [22]. ComPol will restrict itself to one specific observation direction by means of a narrow collimator (see ComPol setup in section 2.2). With the approach of precise pointing, the reconstruction from the event cones is not strictly necessary anymore. While it can still help to identify background events through the non-intersection of the respective circles, the pointing allows for a different approach to select the useful events.

Event selection: For all events, that occurred in both detectors simultaneously and sum up to a reasonable energy, the scatter angle θ is calculated in two ways:

1. **Geometrically** from the measured interaction positions R_1 and R_2 and the knowledge about the source location as well as the instrument pointing.
2. With **Compton kinematics** from the measured energies E_1 and E_2 via the Compton formula Equation 2.1.

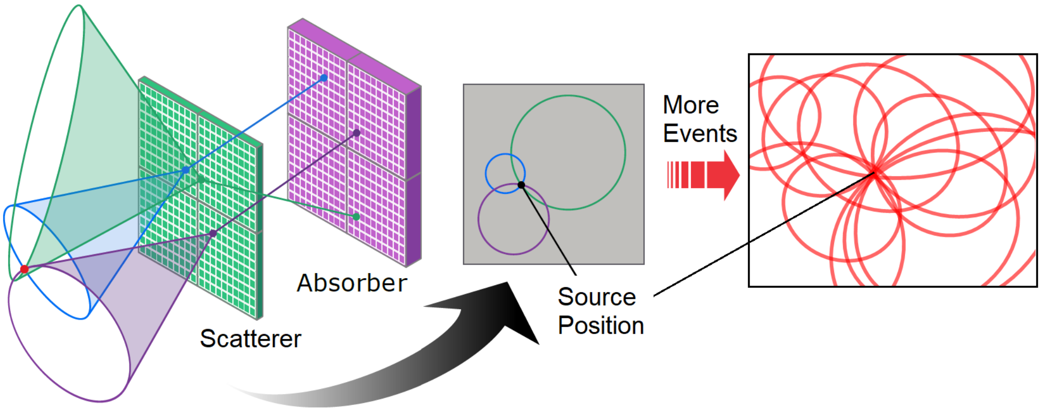

Figure 2.3: ***Source reconstruction for a Compton camera.*** *For a perfect system, three Compton cones from source-photons would give a source position. For a real detector and background photons, a large number is needed for a precise reconstruction. Adapted from [37] and [1].*

For a real Compton event the results of both approaches must match within a margin, that is determined by the resolution of the energy and the position measurement, as well as the pointing accuracy. Therefore the performance of both detectors as well as a precise ADCS is essential for the cleanest possible event selection.

Determination of the Polarization: Compton events allow not only for the creation of spectra (summed energies) and imaging (reconstructed source position), but also for polarization measurements. This is the main goal of the ComPol project.

Every electromagnetic wave caries an intrinsic polarization, given by the orientation of the electric field vector and denoted by the polarization vector ξ. When talking about the polarimetry of astrophysical objects, the measured property is the macroscopic polarization, which is the average of the polarization states of the individual waves [38]. If all orientations of the individual polarization vectors are equally probable, the overall radiation is in total unpolarized. If the radiation source imposes a preference to a certain orientation of the electric field vectors, then a certain value of ξ becomes more probable then others. The macroscopic polarization is given by the average over all photons. The resulting light is partially polarized what is expressed by the **degree of polarization** $P = I_P/I_{total}$ giving the fraction of the polarized light intensity compared to the total intensity typically expressed in percent. The observed orientation is given by the polarization plane, which is

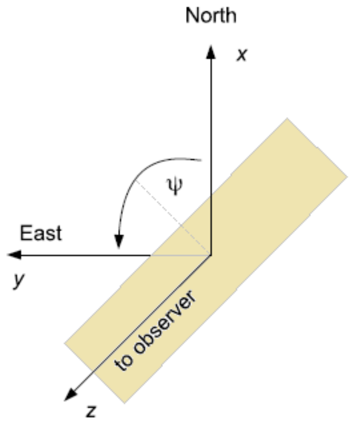

Figure 2.4: *The polarization plane of astrophysical observations is defined by the (parallactic) polarization angle Ψ with respect to the north direction. Adapted from [38].*

parallel to the propagation direction and inclined by the (parallactic[1]) **polarization angle** Ψ measured counterclockwise from the north-south axis, see Figure 2.4. With Compton scattering both the degree P and the angle Ψ of the polarization can be obtained from the knowledge of the polarization dependent Compton cross-section.

When a photon performs Compton scattering the possible outgoing paths are located on a cone with the opening angle θ. These paths can be further parameterized by the azimuthal scatter angle ϕ measured with respect to the initial polarization vector ξ of the individual photon (see left side of Figure 2.5). The differential cross-section of Compton scattering $\frac{\mathrm{d}\sigma}{\mathrm{d}\Omega}(E, E', \theta, \phi)$ contains the angle dependent component $\propto\ -\sin^2\theta\cos^2\phi$, where the polarization dependence is expressed on basis of the azimuthal scatter angle ϕ. The angle dependence is visualized in the polar plot in Figure 2.5 that shows the differential cross-section of incoherent scattering for 100 keV photons for different scatter angles θ. This has the following implications [39]:

- The preferred scattering direction is perpendicular to the initial polarization vector ξ since the term is minimal for $\phi = 90°$ and $\phi = 270°$.
- Since for higher energies the average scatter angle is smaller, the polarization signal decreases with energy.

[1] The standard polarization angle is defined via the Stokes parameters in the fixed reference frame of the source and must not be confused with Ψ [38].

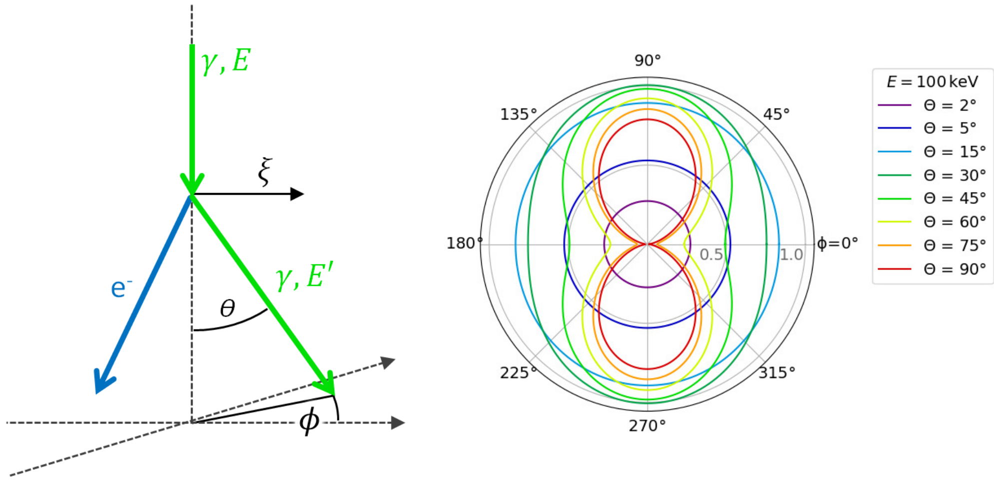

Figure 2.5: ***Polarization dependence of Compton scattering.*** *The incident X-ray with a polarization vector ξ is deflected by the scatter angle θ with respect to the incident path of the photon. The angle between the outgoing path of the photon is described by the azimuthal scatter angle ϕ. The polar plot shows the differential cross-section of incoherent scattering in silicon for different scatter angles θ (radial distance in units of barn/atom). Large scatter angle θ show a clear dependency of ϕ and thus on the initial polarization vector ξ. Both figures are taken from [1].*

- For small and very large ($\sim 180°$) scattering angles θ, the polarization signature is weak as $\sin^2\theta$ approaches zero.

Therefore it is beneficial to perform the polarization analysis only after an additional event selection cut on the scattering angles: There is an optimal scatter angle for which the cut $\theta > \theta_{min}^{opt}$ balances the strength of the polarization imprint and the total amount of remaining events in such a way that the best possible sensitivity is obtained. The value can be approximated analytically from the geometrical maximum detectable scattering angle or be obtained by simulation data, see [1].

After this additional cut, the polarization can be determined from the modulation of the signal strength for different outgoing paths (azimuthal angles). Since the polarization vector ξ is individual for each photon and thus the individual azimuthal scatter angles ϕ are unknown, a new angle Φ is defined with respect to the reference frame of the detector system. From the resulting signal distribution $f_P(\Phi)$, which is shown in Figure 2.6 for exemplary simulation data, it is possible to derive the degree of polarization P and the polarization angle Ψ. It follows a cosine with amplitude A that is shifted upwards by an offset C and shifted by the angle small ψ. This angle

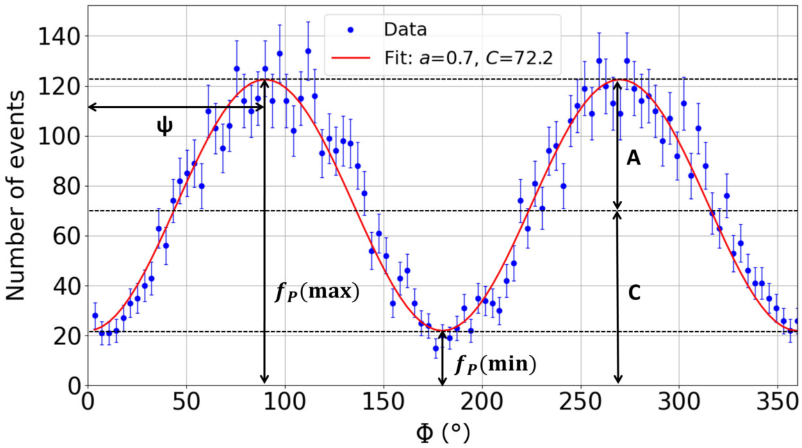

Figure 2.6: ***The imprint of polarization:*** *Simulated and fitted cosine modulation of the event numbers for specific detection locations given by the angle Φ. The position of $f_P(max)$ gives the polarization angle ϕ in the reference frame of the instrument and can be coordinate-transformed to the absolute polarization angle Ψ. The modulation amplitude a is defined as fraction of the cosine amplitude A divided by the offset C. The parameter a is proportional (but smaller) than the degree of polarization P. Figure taken from [22].*

ψ is defined in the reference frame of the instrument and the astronomical polarization angle Ψ (as defined above, see Figure 2.4) can directly be obtained through a coordinate transformation into the Earth's coordinate system. For a completely unpolarized source, the signal is a flat distribution with the height of C, corresponding to the total number of events. The amplitude A describes the amount of events that deviate from the unpolarized case. For a perfect detector and if the cross section would not be a statistical distribution, the degree of polarization would now be given by the modulation amplitude $a = A/C$. However, with the cross section distribution, the the amplitude A never reaches the full value C. Additionally, in a real detector some of the intrinsic polarization amplitude is smeared out. Therefore $A = C$ is not reached for a 100% polarized light but a maximum modulation amplitude $a_{max} = \mu < 1$ [40]. With that, the polarization fraction of partially polarized light is given by $P = a/\mu$. Note that the degree of polarization is therefore always larger than the measured modulation a.

2.2 The Detector Setups for ComPol and ComPol-ISS

In the following the general layout of the detector system is presented. After a brief introduction to the detectors and their energy range, the conceptual mechanical setup of the ComPol instrument is explained side-by-side with the design of ComPol-ISS, as implemented in this thesis. Afterwards the single detectors are discussed more deeply.

2.2.1 The Detectors and their Energy Range

Compton telescopes are most sensitive between 10 keV and 10 MeV, as Compton scattering is the dominant particle interaction in this energy range. The exact values depend on the used detector material. To efficiently collect Compton events, the first detector must be sensitive to the small energies that are transferred to the electrons during Compton scattering. This can be as low as a few percent of the initial X-ray energy [1]. Furthermore, it requires a good energy resolution for the Compton event selection and the amount of photoelectric absorption in the scatterer should be as small as possible. Therefore the first detector should be geometrically thin and have a preferably small atomic number Z, since the absorption scales with Z^5 [1]. Qualities that make **Silicon[2] Drift Detectors (SDDs)** the ideal scattering detector for the ComPol project. The second detector in contrary needs to stop and absorb the the majority of the photon energy. Therefore a high Z material is advantageous. In the ComPol project this is realized with a **Cerium(III) Bromide ($CeBr_3$) scintillator** that is read out by an **array of Silicon Photomultipliers (SiPMs)**.

For the energy measurement, the thresholds for the individual detectors of the ComPol instrument are $E_{min,SDD} = 1$ keV for the scatterer and $E_{min,CeBr_3} = 10$ keV for the absorber [1]. For a successful detection of Compton events, the X-ray must not be stopped in the SDD, but the SDD must be transparent for the particle. For a 450 μm thick silicon detector this transparency is starting at about $\gtrsim$7 keV [1]. The sensitivity study for ComPol further shows, that the simulated Compton events reach useful rates around $\gtrsim$ 20 keV. Below this energy the cross-section of incoherent scattering becomes increasingly small for silicon. Above 20 keV about 1% of the incoming X-rays undergo Compton scattering and approximately half of them are subsequently absorbed in the $CeBr_3$ [1]. The relative rate of Compton events reaches its maximum of around 0.7% at 90 keV. At higher energies, the 10 mm thick CeBr3 detector commences to become transparent too and the rate decreases but is still above a significant level (0.4 %) up to 300 keV. In summery, the sensitivity

[2] The atomic number of silicon is $Z_{Si} = 14$.

range of the ComPol polarimeter is between 20 keV and 300 keV.

2.2.2 The Mechanical Layout of the Instruments

The instrument of the ComPol CubeSat consists of a 31-pixel SDD with a thickness of 450 μm and an approximately 80 x 80 x 10 mm^3 scintillator crystal. Figure 2.7 (a) shows a scaled drawing of these detectors as mounted to their respective readout PCBs (printed circuit boards), shown in green. For the PCBs a standard thickness of 1.60 mm has been assumed. The depicted area of 90 x 90 mm^2 is a common size for CubeSat PCBs. These dimensions as well as the dimensions of the $CeBr_3$ (red) are not final yet. The scintillator crystal will be optimized to cover the largest area as possible within the CubeSat structure. The current ~20 mm difference to the outer CubeSat volume of 100 mm will be used for the CubeSat frame and mounting structures[3]. Also the need of an additional active veto around the crystal is under discussion and could lead to a reduced area of the crystal. The shielding study showed, that the best passive shielding configuration against high energy photons and cosmic radiation background (including the SAA contribution) is a ~2 mm lead or tin shielding plate (gray) right above the SDD detector [22]. For the real implementation there will be a non-zero distance between the shielding and the SDD-readout PCB that will be determined by the final electrical components on the board. In the drawing and the so far performed simulations the distance between the SDD and $CeBr_3$ was set to 5 mm [1, 22]. For the final implementation, this has to be revised and optimized (see section 3.3). The collimator (gray) is planned to have a maximal length of 100 mm that could be shortened to a minimum of ~50 mm [22]. As shown in the 3U+ CDS drawing (Figure 1.5) the collimator is only allowed to protrude the CubeSat structure by 36 mm. The difference of this and the final collimator length will allocate the ComPol instrument within the CubeSat volume. Depending on the final length the space above the shielding plate can be used for other CubeSat subsystems. Since the final ComPol system is not fixed yet, all dimensions are preliminary. They can however serve as instructive basis for the comparison with the upcoming ComPol-ISS layout.

The instrument of ComPol-ISS will have two 7-pixel SDDs and a 25 x 25 x 15 mm scintillator crystal as main components, see Figure 2.7 (b). The distance between the two detectors is decided to be 6.1 mm, see section 3.3 for the reasoning. What was omitted in the other sketch due to the preliminary character of the ComPol design, was the fact that the calorimeter does not solely consist of the crystal. Cerium(III) bromide $CeBr_3$ is a hygroscopic material and therefore must be packed

[3] not shown in the instrument sketch

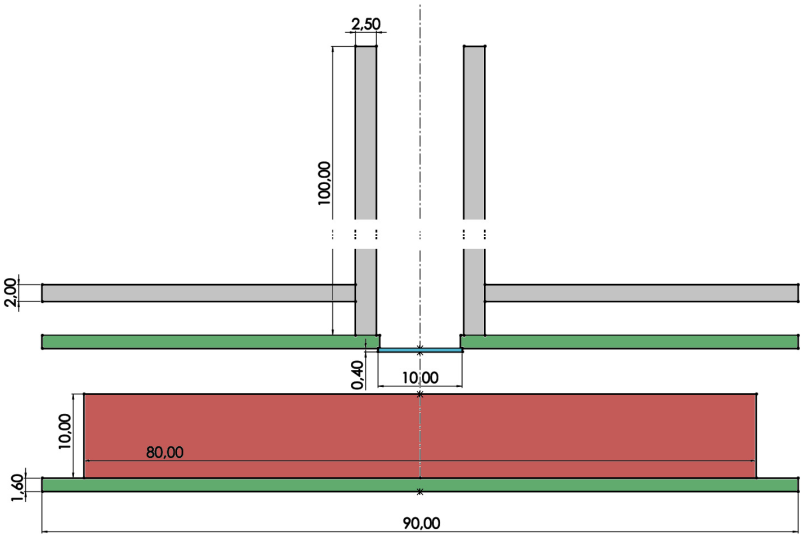

(a) *ComPol instrument layout.*

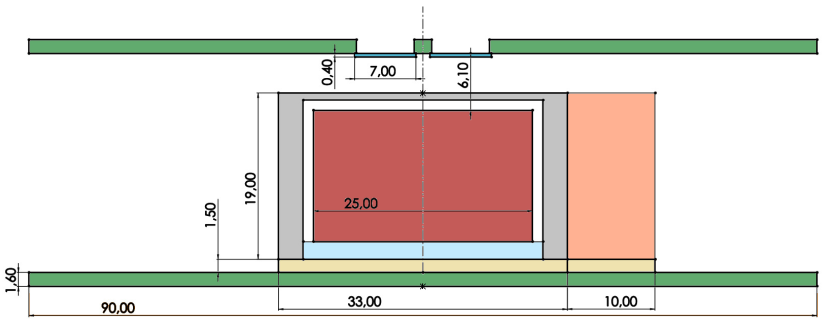

(b) *ComPol-ISS instrument layout.*

Figure 2.7: *Cross sections of the planned ComPol and ComPol-ISS setup. The main components are the $CeBr_3$ crystal (red), the SDDs (dark blue) and the detector PCBs (green). In the ComPol layout (a) the shielding plate and collimator are shown. Both are currently planned to be of lead. The drawing for ComPol-ISS (b) is more detailed. The $CeBr_3$ is encased in an aluminum housing (gray) with an quartz window (light blue). To one side of the $CeBr_3$, a plastic scintillator (coral red) is added as veto. SiPMs (yellow) are below both scintillators. All components have approximately a square base, except the veto scintillator. The drawings are true to scale, but are based on partially preliminary dimensions.*

in an airtight housing (gray). Below the crystal, a quartz window (light blue) allows the scintillating light to pass to the readout detectors: an array of SiPMs (yellow).

The thickness of the SiPMs themselves is 1.35 mm, but an optical glue will be applied in between the SiPM and the casing, resulting in a total thickness of ∼1.5 mm. Since currently an active veto is in discussion, the IOV mission will also demonstrate the parallel readout of an ∼10 x 33 x 19 mm^3 plastic scintillator (coral) placed next to one side of $CeBr_3$ casing. It will be an active veto for charged particles and as such give valuable real life data for this part of the background in LEO orbit, which then can be compared with simulations.
The ComPol-ISS instrument will neither have a collimator nor a heavy shielding. As mechanical protection, a ∼3 mm aluminum case will surround the whole payload with a window cutout in the observation direction. This window is needed to let in the soft X-rays, that otherwise are would be attenuated due in the aluminum case. For hard X-rays, however, the effect of the aluminum becomes increasingly weak, so that ComPol-ISS will be penetrated by hard X-rays not only trough the window. Thus, ComPol-ISS will actually not be a Compton telescope but a Compton camera. Like this it will record more Compton events in total, resulting in a larger data set and furthermore will characterize the background in greater detail. Also as Compton camera, ComPol-ISS will however not observe the whole 4π. It will be mounted on an external ISS-platform together with other experiments, whose materials will shield ComPol-ISS at least from one side, possibly from multiple sides. Additionally the ISS covers a large solid angle and acts as specially thick shield in the respective direction. On the other hand it for visual photons however, the ISS on the end of the spectrum, it contrarily acts as a gigantic reflector for optical photons and will enhance both the duration and total intensity of the illumination with sunlight. Even when neither Sun nor Moon are in the field of view of the window cutout, an substantial amount of reflected light might come from the direction of the ISS. Therefore, the shielding strategy against visual light (see chapter 4) plays an essential role in the design of the ComPol-ISS layout.

2.2.3 The Silicon Drift Detectors (SDDs) and Signal Readout

In this section, the scatter-detector is discussed. First, the Silicon Drift Detector technology is briefly introduced by using the SDD of the ComPol project as example. Then the readout system as implemented for the ComPol-ISS mission is presented with focus on the response to the background of optical light.

Silicon drift detectors are semi-conductor detectors and rely on the same basic electron-hole pair detection as in the depletion zone of a simple reverse biased p-n junction. The depletion zone is a region without free charge carriers that builds up at the interface of an p-doped and n-doped semiconductor. It acts as an intrinsic barrier for the holes in the p-doped and the electrons in the n-typed material. The application of an external voltage in the (non-conductive) reverse direction, the dimension of the natural depletion zone can be further increased. When optical photons with an energies greater than the band gap of the respective semiconductor (here Silicon with $E_{gap} = 1.12$ eV) are absorbed, they produce exactly one e^-/h^+-pair each[4]. In contrary, when a high energy particle deposits energy in the semiconductor, a certain amount of e^-/h^+-pairs is created that is proportional to the energy. In the depletion zone, these pairs are separated by drifting to the anode and cathode, respectively. Outside the depletion zone they recombine. For an SDD the working principle is the same, with the difference that:

- The external voltage is so high that the total detector volume is depleted.
- The layout is optimized to have a large detector volume (large cathode) but a very small anode, allowing for the low noise and high count rate performance.
- Drift rings around the anode are used to create an electric field that efficiently guides all electrons from the large detector volume to the small readout anode.

The above points can be seen in Figure 2.8 that shows the ring structure of one pixel of the SDD array used in the ComPol project. These SDDs were originally developed for the TRISTAN[5] upgrade of the KATRIN[6] experiment, that will search for sterile neutrinos [42, 43]. The TRISTAN SDDs are monolithic SDD arrays of multiple pixels that are aligned in an hexagonal pattern, see Figure 2.9. Each of the pixels can handle a count rate of up to 100 kcps, while having a very good energy resolution ($<$ 300 eV FWHM at 20 keV) [1].

The bias voltage that depletes the detector volume is applied at the back contact. The anode (small circle in the middle) is set on ground and the drift rings (red) are biased in a way that they become continuously more negative from ring 1 to the outermost ring X. This creates an electric potential, whose minimum is indicated with the dashed line. In the ComPol project the back contact side will face the observation direction. This side is also called the entrance window. When an X-ray scatters off a silicon-electron, the transferred energy leads to the production of e^-/h^+-pairs. The path of the electrons follows the minimal potential to the anode where they are passed to the readout system.

Bonding wires establish the electrical connection to the SDD, see Figure 2.9 (b). Two of these wires reach to the middle of each pixel, one to the anode and one to the first drift ring. The anode is connected to the readout system. The first drift rings

[4] The remaining energy will not produce an other e^-/h^+-pair but lattice vibrations of the semiconductor.

[5] TRISTAN stands for TRitium Investigations of STerile to Active Neutrino mixing.

[6] KATRIN stands for KArlsruhe TRitium Neutrino experiment.

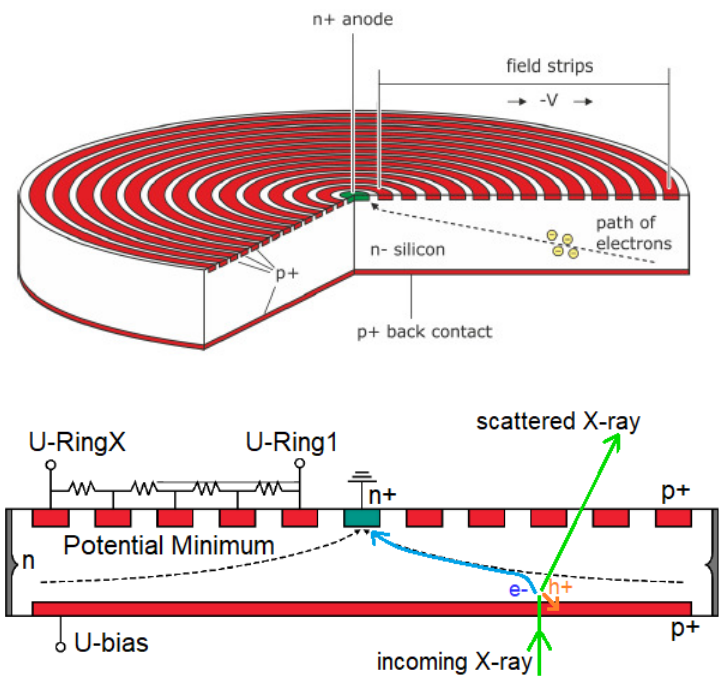

Figure 2.8: *Graphic of the SDD ring structure (from [41]) and section of one TRISTAN SDD pixel (adapted from [1]). The p+ doped regions are shown in red, the n+ doped anode in green. When an incoming X-ray (green) scatters at an electron bound to an silicon atom in the depletion zone (white area), the transferred energy creates e^-/h^+-pairs (blue/orange). The electron follows the minimal potential to the anode.*

are connected to the hexagonal frame around all pixels to keep them on a shared voltage and keep the bonding as short as possible. The outermost rings are internally connected, so one shared bonding wire is sufficient to supply the *n-th ring* voltage V_{NR}. The other ring voltages are generated from V_{NR}. On the entrance window side are two bonding wires, one to the back contact, supplying the cathode with the bias voltage *back contact* V_{BK} and one to an additional frame around the cathode. This optional *back frame* voltage V_{BF} is slightly more negative than the cathode and shapes the electric field in the outer region of the depletion zone such that electron losses at the edge of the sensor are reduced.

Figure 2.9 (a) shows the planned layout of the large 31-pixel SDD for ComPol and (b) is a microscope photograph of the 7-pixel pre-prototype SDD for ComPol-ISS. The only difference between this laboratory pre-prototype and the version for

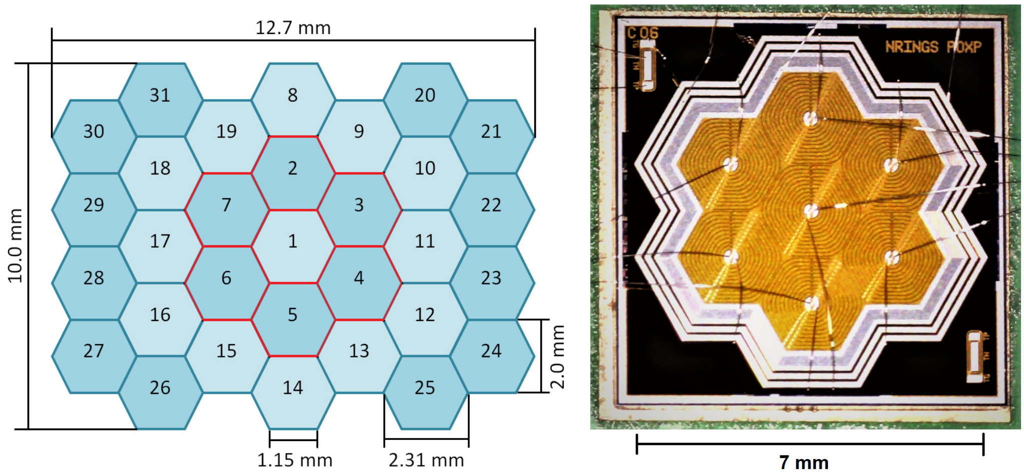

(a) *31-pixel array as planned for ComPol [1].* (b) *7-pixel prototype for ComPol-ISS.*

Figure 2.9: ***Silicon Drift Detector.*** *One pixel has the size of 2 mm and corresponds to one hexagon in the schematic sketch of the ComPol SDD-array (left), and to one drift ring in the microscope photograph of the ComPol-ISS prototype (right). The total prototype size is marked red to guide the eye. Each pixel has two bonding wires: one is attached to the anode in the center of each pixel, the other to the innermost drift ring. The outer drift rings are all connected to the silver frame and have one shared wire connection.*

the IOV flight model will concern the optimization of the wire bonding for space applications. Even though the launch vibrations will be reduced drastically for the ISS mission compared to the CubeSat launch conditions, the bonding will be implemented to be as short as possible to prevent larger oscillations that could damage or produce a short between the wires.

The SDD readout system starts with one pre-amplifier per pixel that generates a voltage signal from the collected charge. The second step is an ASIC (named SFERA) that pulse-shapes the voltage signal and digitizes the pulse maxima. The final step is an FPGA for the data acquisition. In the following only the first step is further discussed since it is sufficient to understand the impact of visual photons.
The electrons arriving at the anode are read out for each pixel individually by a charge sensitive pre-amplifier (CSA). They are placed as close to the SDD array as possible to reduce the distance to the anode. A simplified sketch of the electronic circuit can be seen on the left of Figure 2.10. It converts the incoming charge to a voltage signal proportional to the amount of collected electrons and thus to the deposited

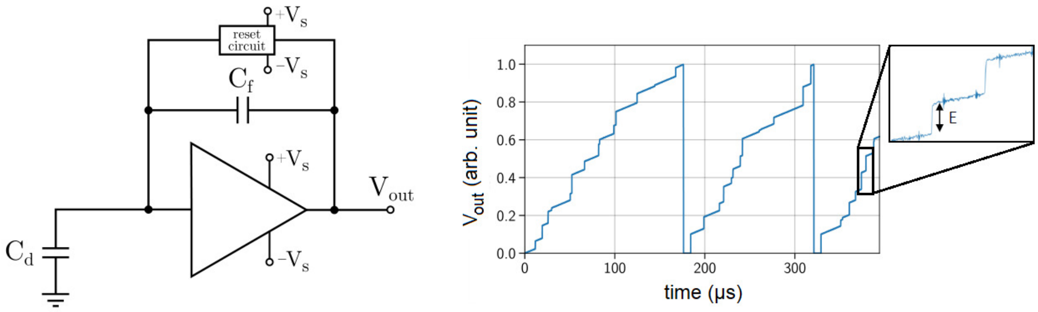

Figure 2.10: *The pre-amplifier of ComPol-ISS translates the collected charge into a voltage ramp. It is reset when the saturation voltage is reached. Adapted from [44].*

energy. The accumulated charge cannot escape via the op-amp or capacitor. It needs to be discharged by either a resistor (continuous reset) or a dedicated reset circuit (active or pulsed reset). For ComPol-ISS the latter was implemented. This creates the characteristic voltage ramp, as shown on the right of Figure 2.10. When an event occurs in the detector volume, it is seen by a step-like voltage increase. This continues until a saturation voltage is reached and the reset circuit triggers the discharge. Every reset is accompanied by a dead time.

In between the events, the voltage slowly rises due to background effects: In semi-conductors there is always a small intrinsic drift of charge carriers from the doped regions across the depleted zone, that results in a leakage current or so called drift current. Also, thermally generated e^-/h^+-pairs are generated at all times and drift to the anode as well. All electrons, that are collected at the anode summed up, result in a small but continuous rise of the voltage. While they are clearly distinct from the voltage step of an high energy event signal with much more e^-/h^+-pairs, they slightly decrease the time until the next reset and thus increase the total dead time. With a band gap of 1.12 eV, silicon based detectors experience a relatively low leakage current by thermal e^-/h^+-pairs, when compared to semi-conductor materials with smaller band gaps (such as germanium). Optical photons however carry enough energy to overcome the silicon band gap and can thus lead to an substantial impact on the leakage current. When too many photons reach the detector volume, the saturation voltage is reached much faster. The slope of the voltage ramp rises, the reset is reached earlier and the total dead time is increased. For this reason already laboratory SDD experiments are undertaken in light-sealed dark boxes. As explained above, the IOV mission will experience an enhanced illumination, which underlines the need of special protection against optical photons.

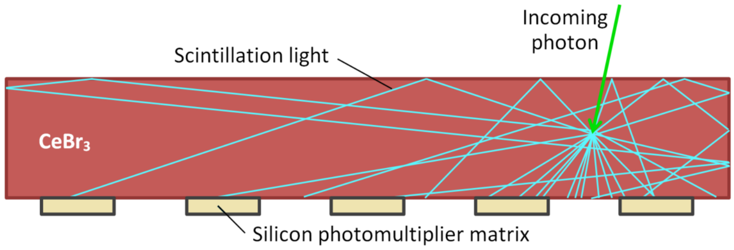

Figure 2.11: *Graphic of an scintillation event in the $CeBr_3$ calorimeter. The absorption of the incoming X-ray (green) generates scintillation light (cyan) that is read out by the SiPM array below. The measured light distribution depends on the interaction point and the scattering of the scintillation light. It will be analyzed by a neural network to retain the interaction point. Figure taken from [1].*

2.2.4 The Calorimeter: $CeBr_3$ Scintillator with SiPM Readout

In this section, a short overview about the calorimeter will be followed by an introduction to the physics of SiPMs and their response to optical illumination.

The calorimeter of the ComPol project is made of a cerium(III) bromide ($CeBr_3$) scintillating crystal that is read out by a matrix of silicon photomultipiers (SiPMs). $CeBr_3$ is an inorganic scintillating material with a maximum emission at 380 nm [45]. Scintillation light is created when ionizing radiation transfers energy to the crystal. The amount of light is proportional to the deposited energy, so that for a full absorption the energy of the incoming X-ray is measured. Other than the SDD array, this detector is not pixelated. The interaction point is reconstructed from the measured light distribution, that is illustrated in Figure 2.11. A neural network, trained with simulation data, will analyze and calculate the position with an accuracy of a few millimeter, like in [46, 47]. In ComPol and ComPol-ISS, the distribution of the scintillation light will be read out by an 8x8 SiPM and 6x6 SiPM array (Figure 2.12 (a)), respectively. An subsequent ASIC sets the trigger threshold and processes the signals before they are transferred to an FPGA for the data acquisition. When one SiPM of the array crosses a threshold, all SiPMs are read out. In this case also the active veto system, consisting of a plastic scintillator on top of two single SiPMs (of the same type as the array), is read out by the ASIC.
In principle, SiPMs are able to measure single photons (more in the SiPM paragraph below). For the $CeBr_3$ readout the threshold however, is artificially increased to 4-5 photons. This is a trade-off between collecting the maximal scintillation light and reducing the dark counts that are intrinsic to SiPMs. SiPMs are by design very sensitive to visual photons. The used SiPMs are even optimized to have a very

high photo detection efficiency (PDE) of about 50% at the SiPM peak sensitivity at 450 nm and more than 40% at the $CeBr_3$ peak 380 nm, see Figure 2.12 (b) [48]. Since SiPMs are this sensitive to the full optical spectrum, the calorimeter part of the instrument and the active veto must be shielded against light very well. The housing of the $CeBr_3$ crystal itself is light-tight. The plastic scintillator however is not pre-packed and also the interface between the scintillators and the SiPMs are potential positions for a leakage. If optical photons enter between the SiPM array and the $CeBr_3$ crystal, this background would reduce the sensitivity to the scintillation signal, since the SiPM cannot distinguish between wavelength. In the worst case it could even distort the position reconstruction of the absorption events. Especially, when the leakage of optical photons arrive at the detector asymmetrically (and changing in time), as it is the case for sunlight that is reflected from the surfaces of the ISS. If it enters the plastic scintillator, it could over-illuminate the active veto.

Silicon Photomultipliers (SiPMs) are semiconductor sensors, designed for low-light applications. They are the technological successor of photo multiplier tubes (PMTs) and have several advantages that are especially important for the application in a CubeSat. They are small, mechanically robust and need only low voltages compared to PMTs. Like the SDDs they rely on the basics of a reverse biased p-n

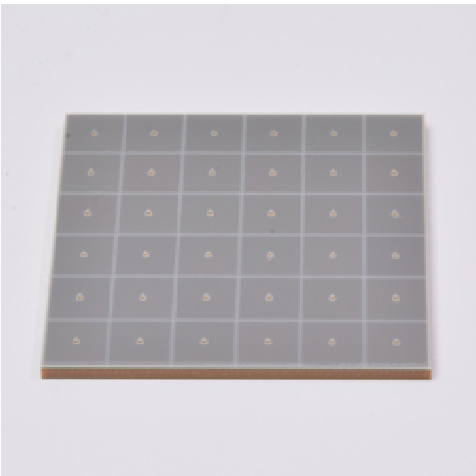

(a) *6x6 SiPM array of ComPol-ISS.*

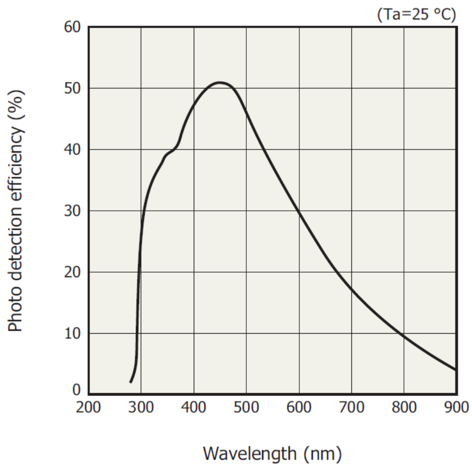

(b) *Photo detection efficiency of the corresponding SiPM series.*

Figure 2.12: *Photograph and exemplary sensitivity of Hamamatsu SiPM S14161-4050HS-06, as given in [48].*

junction. One SiPM consists of a vast number of photo-sensitive micro-cells, between

100 and several 1000/mm^2 [49]. Each micro-cell includes one photodiode, operated in the so called Geiger mode, and a quenching resistor, see Figure 2.13.
For the Geiger mode the reverse bias voltage V_{in} is set slightly higher than the break-

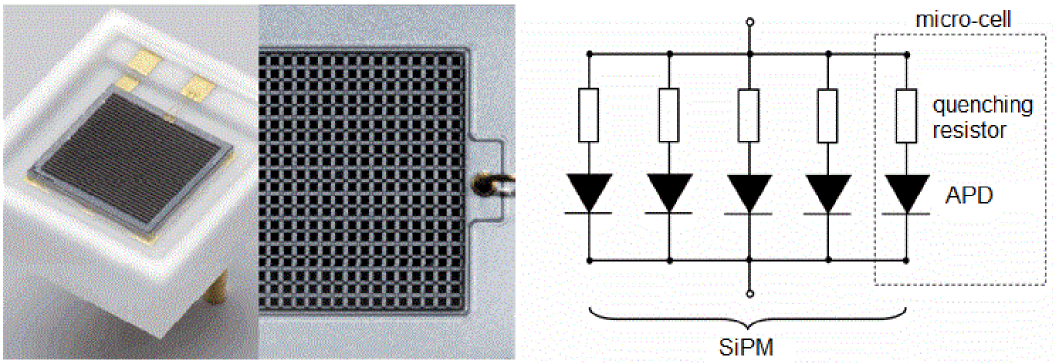

Figure 2.13: *Microscope photograph (left) of a SiPM making the individual microcells visible. The equivalent electrical circuit (right) shows the quenching resistor and the avalanche photodiode (APD), which is biased closely above its breakdown voltage. Adapted from [50].*

down voltage V_{BD} where the photodiode leaves its linear response regime. The high electric field created in the depletion zone, will accelerate the e^-/h^+-pair (created by a photon) to a kinetic energy that is sufficient to evoke secondary e^-/h^+-pairs by impact ionization. They are in turn accelerated, leading to even more charge carriers [49]. Like this one absorbed photon (one e^-/h^+-pair) results in an avalanche of 10^5 to 10^6 additional charge carriers, depending on the overvoltage V_{OV} [50]. This overvoltage is the difference of V_{in} and V_{BD}. The diode breaks down and becomes conductive in the reverse direction. Therefore, diodes operated in this way are also called Single Photon Avalanche Diodes (SPAD) or Avalanche photodiodes (APD). To limit the current and eventually stop the avalanche, a quenching resistor is placed in series with the diode. As the avalanche current builds up, the voltage at the resistor rises, while it decreases across the diode. The lowering voltage reduces the field strength and makes impact ionization less probable [50]. When the voltage seen by the diode drops below V_{BD}, the avalanche is completely quenched. The voltage at the diode increases back to the bias voltage and the APD is ready to detect the next photon. This cycle creates a current pulse that is proportional to V_{OV}, but not to the initial amount of e^-/h^+-pairs created. Thus for a single APD, the same signal is evoked upon by one or multiple photons and a single APD yields no information about simultaneous photons.
SiPMs combine single micro-cells (APD + resistor) to a dense array of independent single photon detectors to overcome exacly this missing proportionality. Each micro-

cell can "fire" and recharge independently. Due to the large number of micro-cells, the total number of fired cells is proportional to the illumination with photons.
Every cell gives the same fixed amount of charge in case of a photon detection [49]. This results into a discrete signal as seen in Figure 2.14. The distinct peaks corresponds to the simultaneous triggering of n micro-cells.
Just like for the SDDs, also thermal e^-/h^+-pairs are produced. While in the SDD that added single additional charge carriers, in the case of the SiPMs every thermally created e^-/h^+-pairs initiates an avalanche in the respective cell. The signals produced by a e^-/h^+-pair of a photon and a thermally created e^-/h^+-pair, are identical. The current of all simultaneous thermal pairs add up to the dark current and are forming a p.e. spectrum just like described above. The dark counts can be reduced by cooling. A remaining dark current, however, is inevitably present as a background in all SiPM measurements. Therefore SiPM p.e. spectra are always discussed with respect to a dark p.e. spectrum.

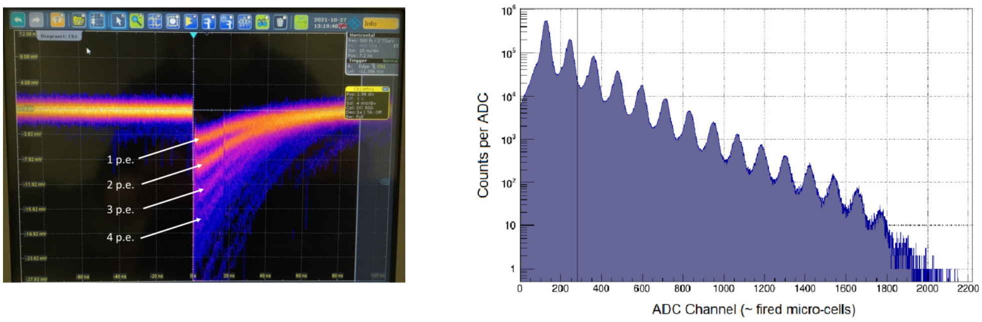

(a) *Distinct SiPM waveforms.*

(b) *SiPM photo-electron spectrum.*

Figure 2.14: *Exemplary SiPM signals showing the discrete nature of the SiPM: When a specific number of micro-cells fires simultaneously, it creates a signal proportional to this number. (a) The analogue waveform output increases step-wise for every additional photo-electrons (p.e.). (b) The digitized and histogrammed signal creates the characteristic SiPM p.e. spectrum, with the peak resulting from the p.e. steps.*

2.3 Summary on the Detector System

This chapter discussed the polarization measurement with Compton telescopes, that is based on the statistical distribution of the detected Compton events. Therefore a clear polarization signal can only be obtained from a high number of Compton events. The detectors of a Compton telescope must be selected such that as many Compton events as possible are detected. The Compton scattering itself transfers only a few percent of its initial energy, while nearly the full X-ray energy must be collected to reconstruct the full event. For the ComPol project two detectors are stacked to combine the different needs. As the scattering detector the TRISTAN-SDDs with a small energy threshold of 1 keV and a very good energy resolution are used. The second detector is a $CeBr_3$ crystal, a scintillating material with a high atomic number Z and thus a with a high absorption efficiency. The scintillation light is then read out by SiPMs, which have an particularly high sensitivity to optical photons. This on one hand allows to measure the energy that was deposited in the crystal, precisely. On the other hand, it must be particularly well protected from the intense solar radiation background in space.

The detector components were developed individually by within the respective research groups and must be newly combined in order to create the first functional and space-compatible prototype, for the ComPol-ISS mission. All components need to be arranged, according to the detector needs and space requirement, and supported by a dedicated mechanical structure. From the information collected from the different groups, a conceptual arrangement of the ComPol-ISS detector system was created and is shown in Figure 2.7 (b). This set the basis for the further development of the full mechanical setup, especially for the light shield sourounding the detectors.

Chapter 3

Hardware Design for ComPol-ISS

Designing the mechanical setup for ComPol-ISS completely from scratch, meant to decide on the exact placement, dimension, and implementation of each component of the assembly. In this chapter, first, an overview of mechanical layout and model components of the well-advanced stack version is given in section 3.1. There, also the recently decided change to a slide-in is discussed. Afterward the most important design decisions are discussed with their respective arguments in the remaining sections. Here, the presented design solutions were made for the stack model but are independent of the change to the slide-in version. The respective design decision sections are referenced in the components description of the overview section.

3.1 Mechanical Layout and Components

ComPol-ISS will be part of a joint IOV mission of the LRSM (Laboratory for Rapid Space Missions at TUM) that will be conducted at the Bartolomeo platform, which is attached to the Columbus Module of the ISS and offered by AIRBUS. Besides the ComPol prototype, an antiproton detector (AFIS) will be tested, as well as crucial parts of a CubeSat bus, developed by the LRSM. Together they make up a 3U-sized structure, which is the smallest payload size accepted for Bartolomeo. The 3U-structure is comprised of three independent boxes, one each for ComPol, AFIS, and the bus, see Figure 3.1 (cyan rectangle). They share a joint structural backplate that carries a backplane PCB establishing the electrical connection between the physics instruments and the bus. For simplicity, it is planned to have a single electrical connector per instrument as depicted in the CAD-drawing of the 3U-structure.
The backplate is then mounted to the ArgUS multi-payload adapter, see Figure 3.1 (red rectangle), that is provided by AIRBUS and allows small payloads to share one much larger standard Bartolomeo slot, that is depicted as one gray box in the conceptional drawing of Bartolomeo at the ISS. For ComPol, a slot with unobstructed zenith pointing as provided by most Bartolomeo slots is selected. Also in the LRSM structure, ComPol is located at the topmost box and was initially defined to take up roughly 1U. The x-direction (see Figure 3.1) is strictly fixed to no more than a maximal 100 mm, since the Bartolomeo mounting points for a 3U-payload

must be met. The y-direction is the most flexible. The Bartolomeo slot provides much more space than needed and the costs are dominated by the mounting surface, not the extension in y-direction. Since however, the final goal of ComPol is a 3U+ CubeSat (see Figure 1.5), the ComPol-ISS prototype will already be designed to be as close to a width of 100 mm as possible. The z-direction was initially set to the standard 1U-length of 109 mm. At the time being, the exact length of AFIS and the bus were not finally fixed yet, so that this direction is also up to a degree flexible to be either a little larger or shorter. In any way, the prototype will be designed as compact as possible in all directions.
With a thickness of $\sim$3 mm for the outer cover on both sides and an additional margin for the 3U-backplate of $\sim$2 mm, this results in the **inner dimensions of** $x = 94$ **mm,** $y = 92$ **mm, and** $z = 103$ **mm**.

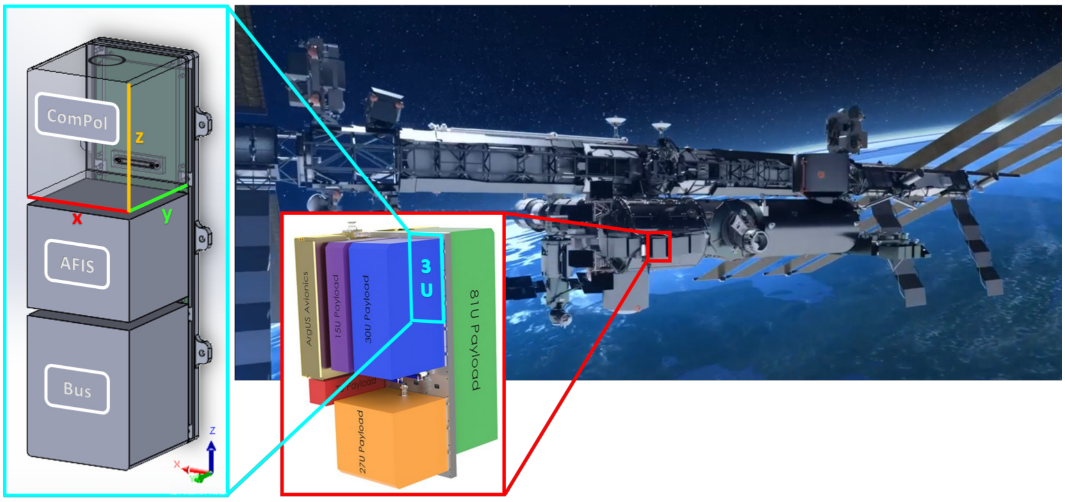

Figure 3.1: *Conceptual drawing of the ISS with the external platform Bartolomeo [51]. In the red rectangle, the ArgUS multi-payload adapter is shown, which allows sharing one standard payload volume of Bartolomeo with other small payloads starting at a minimal size of 3U. ComPol-ISS is part of a joint IOV-mission of the LRSM (Laboratory for Rapid Space Missions), having a combined size of 3U. The simplified layout of the complete 3U design is shown in the cyan rectangle. It is comprised of three independent boxes that are connected to a 3U-backplate, to be screwed to the multi-payload adapter. Embedded in this backplate, a long backplane will connect the ComPol (and the other instrument AFIS) with the IOV-bus.*

After collecting all available information from the different groups and taking reasonable assumptions for everything unknown yet, a first preliminary CAD model was built. For that, the commonly used PCB-stack approach was chosen due to its well-proven and simple nature. It possesses good structural stability and the standoffs between the PCBs are available at flexible heights. Afterward, the model was step-wise improved, including new and updating old information. Many critical design decisions about the size, location, and shape of the components were taken along the way, of which the most important are described in this chapter, starting in section 3.3 and linked in the following design description.

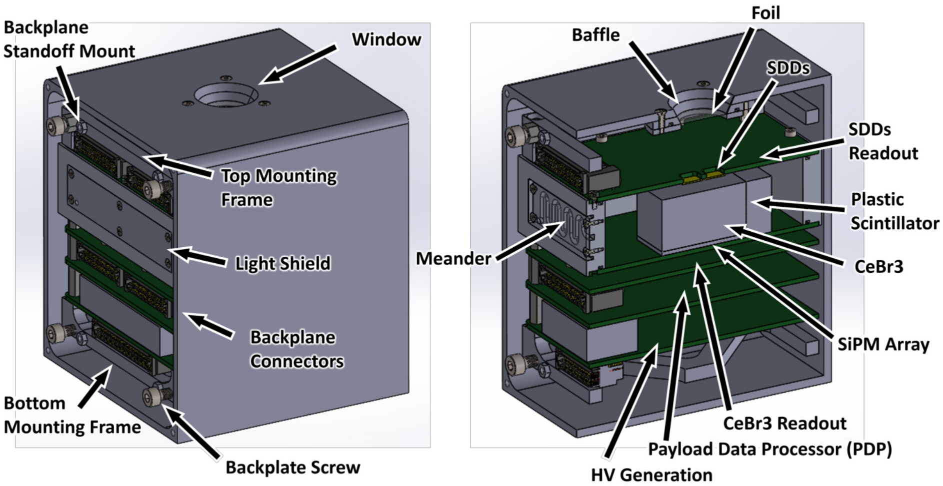

Figure 3.2: *The stack model of ComPol-ISS (Revision 4.1)*[1].
The ComPol-backplane connecting the PCBs is not shown in the picture to allow a view of the stack. Also for illustration purposes, the detector unit is turned by 180° compared to the actual design to show the meander. In the final configuration, the meander will face the box wall opposite the backplane side since that is the darkest part of the instrument. The plastic scintillator (veto) stays opposite to the meander firstly to bring a greater distance between the SiPMs below the veto and the meander, secondly because the routing on the $CeBr_3$*-PCB is such that the board-to-board connector is at the side opposite to the veto and would obstruct the tracks to the 90°-connectors to the backplane. The labeled components are further described in the list of essential parts.*

The resulting mechanical structure incorporating all the decisions is shown in Figure 3.2 and fits very well in the volume of 1U. The essential parts of this **stacked prototype**[2] are described in the following list:

[1] Version 4.1 was the latest version before the recent decision to change from a stacked approach to a slide-in model.
[2] For the reasoning of the design change to the slide-in model, see Design Change (page 46).

- The **mounting frames**[3] on the top and the bottom of the stack that provide structural stability while covering only a small area on the PCBs. Together with the 3M sized standoffs in the corners of the PCBs, they form the mechanical backbone of the stack. The small and middle standoffs are female-male standoffs with the male part pointing downwards. The third set of standoffs is female-female allowing the Bottom Mounting Frame to be screwed to the stack with countersink screws again, to spare the space of a screw head. Every mounting frame has two M4 screws to fix the stack to the 3U-backplate.

- Five 90 x 90 mm^2 **printed Circuit Boards (PCBs)**, from top to bottom: The SDD-PCB, the $CeBr_3$-PCB, the $CeBr_3$-readout-PCB, the Payload-Data-Processor board PDP-PCB, and the High-Voltage generation HV-PCB. The electrical connections between the PCBs are established by 90°-connectors and a common ComPol-internal backplane (∼1U-sized), that is based on the mounting standoffs shown in Figure 3.2. This **ComPol-backplane** is then connected to the larger general backplane. More details about the PCBs as well as the reasoning behind the order in the stack and, their electrical connections are discussed in section 3.2.

- The **detectors** themselves sitting on their respective PCBs, as described in detail in subsection 2.2.2 and summarized in Figure 2.7 (b). In section 3.3 the reasoning behind the distance of both detectors is discussed.

- A **light shield** around the detectors, that forms the fundamental component of the shield strategy against optical photons is explained in section 3.5. In subsection 3.5.1, the size of the light shield is reasoned, giving the basic design layout. The explicit implementation of the detector light shield with the shown meander to meet venting needs, as well as the thorough testing makes up the entirety of chapter 4.

- The **1U-casing**[4] is a protection box framing the stack, with a wall strength of about 3 mm. It is designed to have no contact with the stack and will be mounted to the 3U-backplate with an M3 screw in each corner.

- In the direction of the zenith the 1U-casing has a **window cutout** that allows also soft X-rays to reach into the detector volume. It defines the field of view, which is described in section 3.4.

- The window is covered with a **foil** to protect the SDD surface from the exhaust of the ISS. It can also serve as a first stage of protection against solar radiation,

[3] With the change to a slide-in approach, the stack mounting is obsolete.
[4] With the change to a slide-in approach, the casing might need to be adapted to fit in the new mounting construction.

if needed. The foil is selected in subsection 3.5.2. The placement at the window is discussed in subsection 3.4.1.

- The foil is framed by a round **foil holder** (see subsection 3.4.2) to allow detector tests with the foil independent of the 1U-casing and to facilitate the handling of the thin foil. The inside of the foil holder and the cutout of the 1U-casing are sloped to form a cone. Like this, optical light, that arrives at a steep angle is reflected away from the setup, see Figure 3.12. In tradition to the stray light mitigation in traditional optical telescopes, this is called **baffle** even though the approach deviates.

The full-stack fits in the 1U-casing with acceptable margins. An assembly test with a **3D-printed mock-up verified the compatibility** as shown in Figure 3.3. The stack can be placed in and taken out of the 1U-casing without interference with the foil holder.

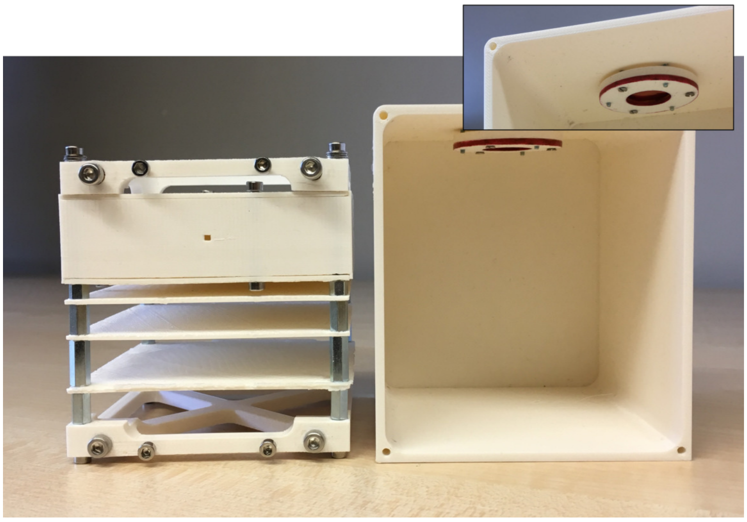

Figure 3.3: *The stacked design version 3.3 was 3D-printed to verify the assembly of the stack. The parts were later reused to test the fitting inside of the 1U-casing. The additional height of the mounting frames, that accommodate the connectors in the later version, was simulated by an additional standoff.*

The stacked layout was designed in a way that the detector unit (light shield and detector PCBs) and the subjacent PCB stack can be separated without the need to disassemble the PCB stack, comprised of the $CeBr_3$-readout-PCB[5], the PDP-PCB, the HV-PCB, and the Bottom Mounting Frame. This was achieved by four long M3 countersink screws in each corner of the Top Mounting Frame that reaches down into the short standoff[6] between the $CeBr_3$-detector- and -readout-PCB. The structural stability of within the detector unit was ensured by a threaded screw hole in the light shield corner. This specific off-standard approach requires the assembly to be started from the detector unit and afterward screwing the standoffs flush to the extended screw ends. This assembly approach and the partial disassembly and re-mounting of the detector unit were tested successfully with a 3D-printed mock-up.

Design Change to Slide-in Version

A design change from a stacked version to a slide-in version was recently prompted due to the following reasons:

- The production tolerances of the mounting frame parts, the PCBs, the standoffs and the light shield could in the worst case add up in such a matter that the backplane connectors lose their alignment with their mates on the backplane. The exact location of the backplane connectors could only be obtained by measuring the dimensions, once the setup is manufactured and assembled.
- It is advantageous to have the option of removing any sub-component from the assembled prototype on its own, not only the detector unit as implemented in the present stack model.

Additionally, it gives greater flexibility by avoiding the above described assembly process. The slide-in version is also the preferred option for the final ComPol CubeSat. The connection of the detector unit and the PCB unit with the small standoff in the stack model would surely be compatible with the soft stowed launch. However, it could be a potential failure point at the vibrational loads of a fixed-mounted launch, which needed to be found out with the vibrational test in the early design phase for ComPol already. Having the potential to slow down the design process of ComPol with further vibrational tests and the re-alignment of the backplane connection mates, the stacked version is depreciated for ComPol.

While the **stack version would still be a viable and close to flight-ready**

[5] Optionally the $CeBr_3$-readout could have been added to the detector unit by changing the short standoff to a female-female standoff and prolonging the corner screw even further.

[6] Since the prototype is launched soft-stowed, the connection in the short standoffs should be sufficient to hold both parts together.

design for ComPol-ISS[7], the above advantages and the approach to stay as close to the final ComPol CubeSat as possible, led to the **decision to change to a slide-in version.** The change from the stacked model to the slide-in one, however, does not influence the design solutions discussed later.

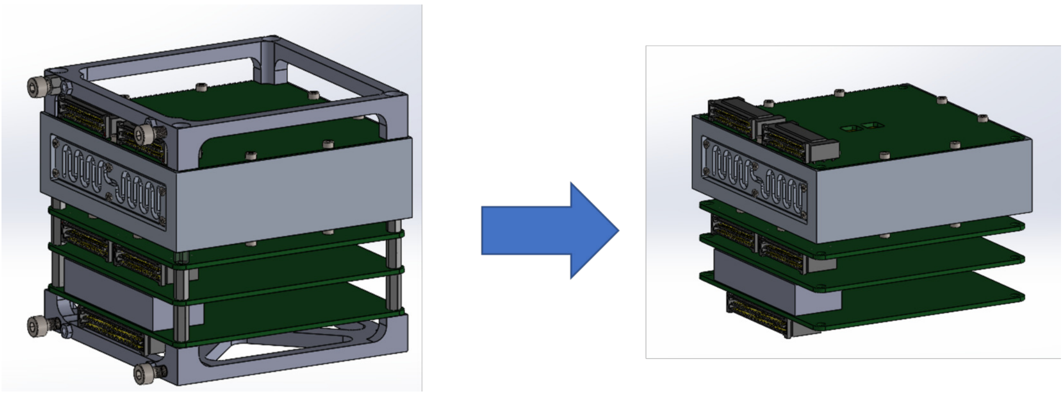

Figure 3.4: *Visualization of what remains of the stack model after the design change to the slide-in model. The necessary new mounting solution per individual sub-component is still to be designed.*

In specific terms, for a slide-in setup, the standoffs and mounting frames are removed, as illustrated in Figure 3.4. Instead of only two separable sub-assemblies as in the stacked version before[8], now a new slide-in frame is to hold all following sub-components individually:

1. The instrument unit: The light shield with the detector boards and the readout boards are mounted individually removable (without opening the light shield) on their respective detector boards with screws, see Figure 3.5 for an example of the board carrier of the SDD readout ASIC.
2. The Payload Data Processor (PDP) board
3. The high voltage generation board

This **slide-in frame** with the respective fixation points at the backplane side and the opposite side **is still to be designed.**

[7] When the backplane is slightly adapted to precisely match the potential offset of the connectors on the stack in the late design process.
[8] The detector unit and the three PCBs forming the stack below.

3.2 The PCBs and their Electrical Connections

In this section first the names and functions of all PCBs are introduced. Then in subsection 3.2.2 the options for their electrical connections are discussed with their respective reasoning and the connectors for the selected solution are presented.

3.2.1 Function and Stack Sequence of all PCBs

From top to bottom the PCBs have the following order and tasks:

1. The SDD readout board **SDD-PCB** has cutouts for the SDDs in the middle of the board. They are glued and bonded with the readout side facing the side of the light shield. Logically the SDD-PCB must be the upmost PCB in the stack[9]. It also hosts the Cubes (pre-amplifiers), temperature sensors and mounting points for a smaller add-on board on which SFERA (the SDD readout ASIC) is located. Due to its shape, shown in Figure 3.5, it is called the **SFERA-L-carrier**. For the final ComPol instrument, two SFERA-L-carriers will be mounted symmetrically on the SDD-PCB. This modular approach keeps the SDDs and SFERA independent and allows to interchange it with different versions of the SDD-PCB and SFERA-L-carrier. Also the number of available 7x7-pixel TRISTAN-SDDs for the ISS-prototype is limited, so that in case of an essential bug in the SFERA-L-carrier prototype the glued and bonded SDDs are not lost.

2. The $CeBr_3$ detector board **$CeBr_3$-PCB** carries the SiPMs, the calorimeter crystal, and the veto plastic scintillator. This is the only 90 x 90 mm^2 board not directly connected to the backplane. Instead, the signals are directly transferred via a board-to-board connector to the subjacent $CeBr_3$ readout PCB.

3. On the $CeBr_3$ readout board **$CeBr_3$-readout-PCB** the calorimeter signal processing takes place in the $CeBr_3$ ASIC. It is located at an extra board since for the final ComPol CubeSat the $CeBr_3$ will fill nearly the complete surface of the $CeBr_3$-PCB and ComPol-ISS aims to come as close to the final setup as possible.

4. The payload data processor board **PDP-PCB** carries an FPGA that combines the data from both ASICs. Using a single FPGA for both detectors allows for better time synchronization. The PDP transfers the processed data via the IOV-bus (CDH subsystem in the bottom box of the 3U-structure) to the ISS

[9] Otherwise, all above PCBs would need for a cutout as in the 1U-casing to allow the X-rays to pass undisturbed. This approach is likely for the CubeSat with the collimator going trough the overlying PCBs as in Figure 1.6.

for transmission. The broadband downlink of the ISS allows to transfer of both the raw data as well as the data after the preliminary[10] data reduction.

5. The high voltage generation board **HV-PCB** transforms the voltage supplied by the ISS to the high voltage level needed to bias the SDDs. It provides one single voltage to the SDD-PCB, where then the individual voltages (for the cathode V_{BK}, at the outermost ring V_{RN}, and the frame V_{BF}, which reduces losses, see subsection 2.2.3) are generated through voltage partition. The HV-PCB is placed as far away from the detectors as possible, resulting in the PDP being on the fourth position of the stack.

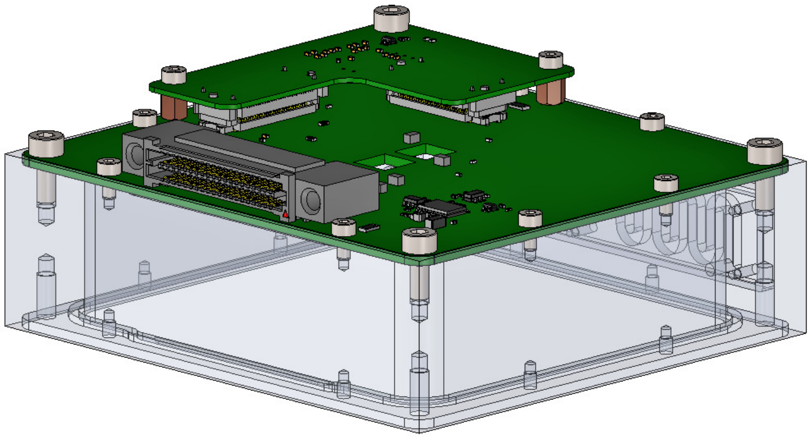

Figure 3.5: *Design of the detector unit with the modular SFERA-L-carrier. The mounting positions are kept on the border of the light shield to be compatible with the bolting constraints found for the light tightness in chapter 4. The model also shows the final surface mounted high density connectors selected after the decision for the design change to slide-in, differing from the ones in the stacked version 4.1. Instead of two connectors, now a larger one with alignment guiding posts is used. The screws on the light shield were moved to the side.*

3.2.2 Decision for a Backplane and High Density Connectors

The initial options for the connection of the PCBs were (a) direct board-to-board connectors typically used in stacks, (b) small ridgid flex PCBs with kapton cables

[10] Preliminary because it is the first version of the data reduction mechanism later needed for the CubeSat version.

to be connected to the 90 x 90 mm^2 boards, and (c) a backplane with 90° connectors.The board-to-board connectors were soon discarded for the general solution since it would require the SDD bias (and signal) voltages to pass through all five (and four) boards, taking up important space on the other boards. Only for the connection of the two $CeBr_3$ boards, it was the optimal solution. In principle the $CeBr_3$ ASIC output could have passed to the PDP-PCB by a board-to-board connector too, but it was preferred to keep the connection to the PDP uniform.

For the remaining connections, the options for bypassing intermediate boards were thought through. The small add-on PCBs with kapton cables would be the most modular and flexible version, also allowing for the minimal height of the respective standoffs. The backplane on the other hand requires 90° connectors, that have a larger height compared to the add-on PCBs. The capton cables, however, pose a higher risk for loose contacts when exposed to the launch vibrations. While still better than traditional cables, since they are enclosed in capton, it was discouraged for the final ComPol version, but not yet excluded for ComPol-ISS. The major caveat was however, that the small add-on PCBs would require for explicit designing, where the design effort would scale with the amount of connections. Also a large amount of connections by capton cables would take up a significant amount of room between the PCBs and the 1U-casing. That could have resulted in the need to make the PCBs smaller to stay within the defined internal volume. The backplane on the other hand only needs as little room as the PCB thickness, defined by the number of needed layers. Also, the routing design is more compact and the design effort stays reasonable even for a great number of signals. Together, this lead to the design-changing decision to use an approximately 1U-sized ComPol-internal backplane.

For both the $CeBr_3$ board-to-board as well as the 90° backplane connectors, high density pin connectors from the SAMTEC SEARAY™ series with a pin pitch of 1.27 mm were selected. They are available with and without alignment guiding posts. An example of the used SEAM and SEAF-RA connectors with is guiding posts shown in Figure 3.6 In the stacked model Figure 3.2 first the version without guiding posts was used, due to space constraints by the mounting frame. The design change to the slide-in version gives the room to use the ones with guiding posts, shown in 3.5. The screws of the light shield and the design of the interface sealing were being adapted to the new connector after all tests described in chapter 4.

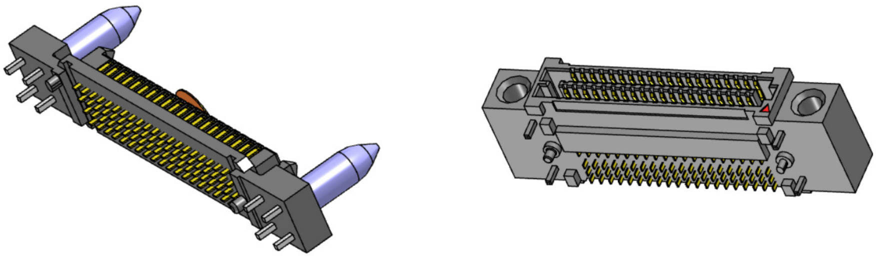

(a) *The male SEAM connector for the backplane.*

(b) *The female 90° SEAF-RA connector for the PCBs.*

Figure 3.6: *Exemplary high density 90° SEARAY™ connectors of SAMTEC. The shown 20 pins times 4 rows SEAM/SEAF connector pair is used to connect the SDD-PCB and the backplane. The alignment guiding posts are optional but make the assembly fail-safe and the connection more rigid.*

3.3 Distance of SDD and $CeBr_3$

For the final ComPol instrument, the distance between the SDD and $CeBr_3$ has to be optimized carefully [1]. It is a trade off between angular resolution and the total number of Compton events: The resolution on the scatter angle decreases with decreasing distance, due to the limited position resolution of the detectors (SDD pixels, scintillator light distribution). A poor angular resolution washes out the modulation in the Φ distribution (Figure 2.6) and impacts the final sensitivity onto the degree of polarization. Simultaneously, the solid angle covered by the calorimeter gets larger with decreasing distance. This results in an enhanced polarization signal, since the Compton cross section depends on the scatter angle (see Figure 2.5). Also, the total number of coincident events in both detectors is increased.

For ComPol-ISS this decision is less critical, since it is not expected to record scientific data. The overall polarization of recorded X-rays from random sources is expected to be unpolarized. Instead, the performance of both detectors individually and together is to be checked. Therefore losing angular resolution is preferred over losing events in the scintillator. Choosing the smallest possible distance of the detectors also helps to fit everything inside the small volume.
The closest possible location is determined by the level of the SDD readout bonding plus a safety margin. All together it was decided to leave a distance of 4.5 mm between the SDD and the aluminum case of the $CeBr_3$ (CAD in appendix Figure 1). with the location of the crystal within this case, the resulting total distance is 6.1 mm.

3.4 Window Cutout and Protection Foil

The wall strength of the aluminum 1U-casing around the detector setup is 3 mm. While hard X-rays can in principle penetrate this thickness, the X-rays in the energy region of interest would be heavily attenuate, see Figure 3.7, especially below 200 keV, where the detectors are sensitive to polarization.

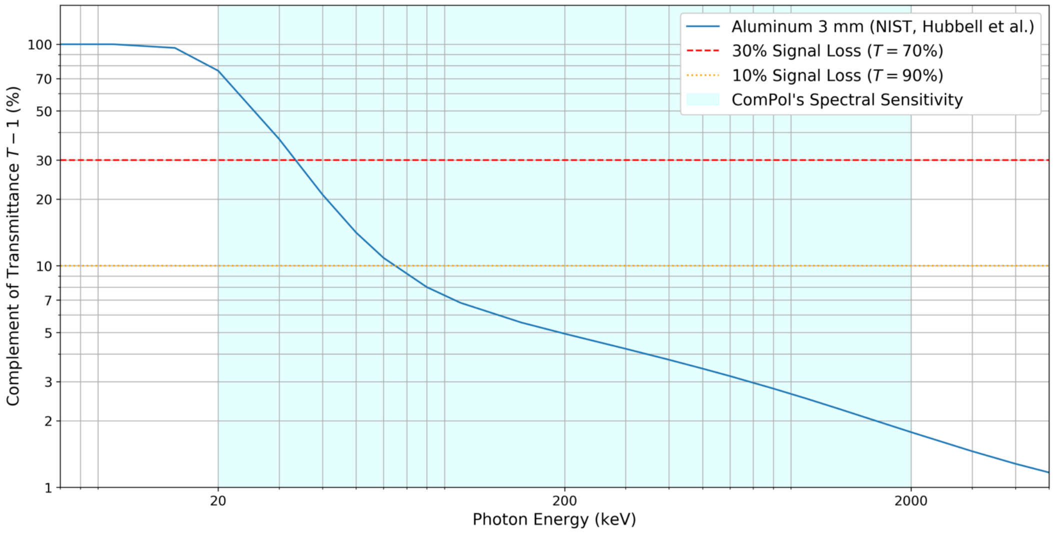

Figure 3.7: *The graph shows the fraction $(1-T)$ in % of the X-rays that get stopped by a 3 mm thick aluminum sheet. The transmittance T is calculated from [52] as described in subsection 3.5.2.*

Therefore, in the viewing direction (zenith) a window cutout is removed from the casing. The exhaust of the ISS, consisting of a haze of various waste molecules, could now enter through the cutout. For the electrical and structural components, it poses no particular thread. In contrast, the SDD surface must be protected by means of a protection foil to prevent these gas molecules from accumulate on the detector, what could eventually alter its detection characteristics. The foil it is not only used as exhaust protection, but also as a first stage of the protection from optical photons, the foil selection is discussed in subsection 3.5.2. The critical design decision, where to place the foil is discussed in subsection 3.4.1. Hereafter, the joint design of the foil holder and 1U-casing cutout is presented in 3.4.2, including a paragraph about the machined processing of the foil.

The size of the cutout and the design of the foil holder not only determine the field of view for the X-rays but also for the background from solar radiation. Therefore, as well as to be closer to the pointed observation mode of a Compton telescope (op-

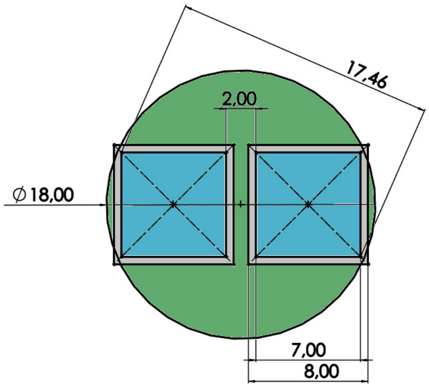

(a) *Dimensional sketch of the sizes of the SDDs (blue with gray handling area) and the window diameter (green hints at the PCB).*

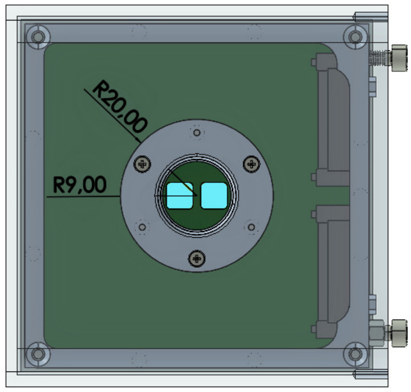

(b) *Design of the foil holder below the cutout shown in relation to the whole (transparent) 1U-casing.*

Figure 3.8: *The window size is defined to be about the largest dimension of the sensitive SDD area. In (a) the dimensions are illustrated: with a distance of 2 mm between the 7 x 7 mm^2 detection area, this results in 17.46 mm. In (b) the implementation of the foil holder in the model version 4.0 is shown. The inner wall of the foil holder and cutout in the 1U-casing are angled as depicted in Figure 3.12. Therefore the innermost diameter of the foil holder defines the window size to 18 mm.*

posed to a Compton camera), that only uses straight incoming X-rays as described in section 2.1, it was decided to limit the cutout size to the outer dimension of the two SDDs.
The total size of each SDD is 8 x 8 mm^2. With a handling area of 500 μm on the readout side, the detection area of the SDDs is 7 x 7 mm^2. With a distance of 2 mm between the SDDs detector areas, the largest diagonal plus a small margin results in a window diameter of 18 mm, see Figure 3.8 (a). Since the foil holder will determine the window, this diameter is not the size of the cutout in the 1U-casing. This cutout size is adapted to the exact design of the foil holder, and is therefore outlined in subsection 3.4.2.

3.4.1 Decision for the Foil Location

The primary task of the protection foil is to shield the SDD detector against the exhaust gas of the ISS. To accomplish that, it could either be placed directly above the SDD on the PCB (Figure 3.9 (a)), or mounted to the cutout in the 1U-casing(Figure 3.9 (b)). The first option would allow the exhaust to enter the box at the cutout, the second would require an venting hole, since no considerable volume is allowed to be gas tight in space applications. Depending on the performance of the main light shield around the detectors, this venting hole could be a simple cutout (placed far enough away from the SDD) or a meandering venting hole as designed for the light shield in section 4.1.

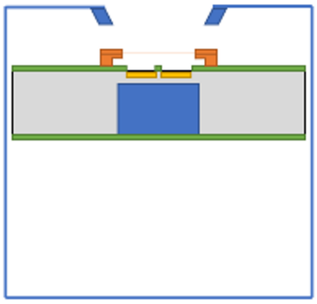

(a) *Foil mounting on the SDD-PCB.*

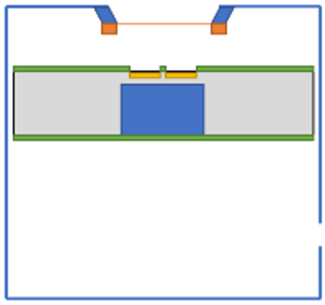

(b) *Foil mounting on the 1U-casing.*

Figure 3.9: *Schematic drawing of the two foil holder options. In (a) the foil is mounted to a cap sitting on the SDD-PCB and only protects the necessary part. In (b) the foil is mounted to the bevel below the cutout, that depicts the baffle (at that time visioned larger). It shields the full box, but also closes the volume. Every closed volume of notable size requires for a venting hole, allowing the necessary gas exchange going from pressure to vacuum (more on venting requirements and solutions in section 4.1).*

Multiple arguments were selected for both concepts, most of them favoring the PCB mounting solution, e.g. (1) that no venting solution for the 1U-casing is necessary, that would either make the box wall thicker or let in the exhaust gas at a different location; (2) that detector tests could already be conducted without the outer box, but with the foil in place, i.e. before the assembly, when the components are still individual and connected via cables (flat satellite configuration).
However, it faced major counterarguments that lead to its exclusion:

- The foil holder could potentially activated by cosmic radiation, see [22] for further information. Placed close to the detectors an activated holder would be a major background issue. Therefore any structure should be kept as far away from the detectors.
- During the mounting process the SDD surface or bonds could potentially be damaged, since the mounting on the PCB would be very close to the SDDs by design. This could pose a mechanical showstopper to the mission, as the number of available TRISTAN-SDDs are limited and only few are spared.

Consequent, the foil holder was designed to be mounted to the 1U-casing.

3.4.2 Foil Holder and Baffle Design

In the previous section one of the drawbacks of the mounting option on the 1U-casing was that the detectors could not be tested with the foil before the finished assembly. To mitigate this downside, a two-sided foil holder was designed, that holds the foil in place without the need of the 1U-casing. That allows to easily remove and attach the foil to the 1U-casing at any time. In the following, first the general layout together with the 1U-casing cutout is discussed. Afterwards the frame itself and the screwing that allows the modular handling is presented. At the end, attention is drawn to the processing and handling of the foil as well as two ongoing minor design questions.

General Layout

The foil holder is comprised of two concentric rings, between which the foil can be fixed with six screws. To meet the 1U constraints without changing the 1U-casing, it is mounted to the inside of the 1U-casing, as shown in Figure 3.2. If for the flight version it is preferred to place it outside the 1U-casing and reduce the box size by the height of the holder, it can be easily re-designed by adapting the opening diameter and the screws holding the adapter together. The rings have a common slope with the cutout to form the baffle, further explained in section 3.5. The minimal diameter is defined to 18 cm and together with the slope, resulting in the remaining diameters. For the time being, an arbitrary slope ratio of $z/x = 2$ was chosen, giving an angle of $\sim 63°$.

To make the foil holder itself as light tight as possible, a groove[11] for a 1.5 mm o-ring was included in the design. A first assembly test was conducted with 3D printed parts and a 10μm kapton foil, sparing the special foil for the test. It showed very clearly, that the mounting with the o-ring was very difficult. It was nearly impossible to keep the foil even and tensioned while fixing the screws. Therefore, firstly the groove was simplified by moving the cutout into the upper ring only, giving at least one planar ring, and secondly an aluminum version with and without groove were produced for further tests.

Modular Mounting with Particular Screwing

To allow for a mounting and dismounting without the assembled foil holder, it is screwed in a special way: Three of the screws hold the rings together, when not mounted on the 1U-casing. They are short, so that they are not extending above the

[11] With the knowledge from the ongoing light shield evaluation, that two flat metal surfaces are not necessarily light tight when screwed together

surface level of the other ring, as depicted in Figure 3.10. The three remaining screw holes are used to mount the foil holder to the 1U-casing with longer countersink screws.

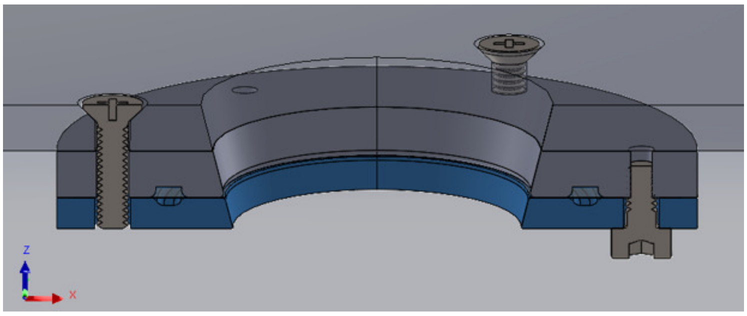

Figure 3.10: *Detailed view on the foil holder, showing the o-ring grove and the bolting.*

Foil Processing, Assembly and Open Questions

The remaining task was to produce small circles of the foil (given as coil from the manufacturer). To process the foil, two viable options were found. It can either be cut by a laser cutter or by hand with a customized stamping tool with sharp edges. The commercially available stamping tools for leather processing comes close to the needs, but were not available in exactly the needed size. The laser cutting option gave acceptable results, as shown in Figure 3.11. However, laser cutting is

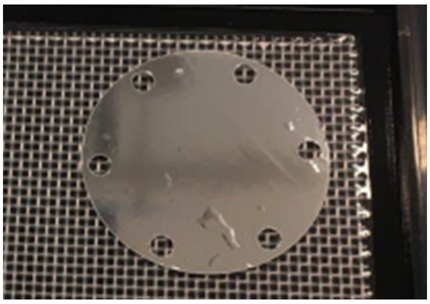

Figure 3.11: *Protection foil, that was cut into the desired form by laser cutting. The bubbles are only due to the used storage container.*

far away from clean room conditions, which are used at the assembly of aerospace hardware. The laser is cutting by burning a small border in the material. Therefore it is unavoidable to have remainders of burned material on the foil. It is unclear if this is limited to the cutting edge, or if it affects the whole foil circle. It is to be tested if an influence on the performance (reflectivity, permeability) of the foil is notable and if cleaning with e.g., ethanol, could reduce that impact. The cutting with a stamp should be kept in mind as an alternative, in case an impact is found to be above the acceptable level remains even after cleaning. This would require a customized sharp stamping tool to be designed and produced explicitly for the cutting of the ComPol-ISS foil.

As a summary, the remaining questions are:

- Is laser cutting a usable processing technique?
- Is the foil holder without the groove easier to assembly and does it hold the foil tightly and light-tight?

3.5 Protection from Sunlight

Orienting the Earth every 90 minutes, the ISS will will be in Earths shadow and in the intense solar radiation, half of the time each. During the day-times, one must differ between the times, when the Sun is in the field of view and radiates directly through the window, and times, where the Sun is outside the field of view. When the Sun is in the field of view (as calculated from the attitude of the ISS), the detectors will be shut down. Additionally, the on-board software will disconnect the detectors when rates of a problematic size are occurring. When it is outside the field of view it is nevertheless not dark. The solar radiation is reflected off the ISS surfaces, e.g., the Columbus module, the solar arrays or the slightly elevated 7th Bartolomeo slot [53]. With various reflective surfaces in many directions, there will be reflected light shining onto the window of ComPol-ISS most of the time. Even though it will be only reflected light, for the intense solar radiation in space with an average intensity of 1370 W/m^2, even a fraction is quite a substantial illumination condition. As discussed in the detector introduction chapter 2, both, SDDs and SiPMs are highly sensitive to optical photons. It is therefore essential to shield the intense solar radiation from penetrating the setup and reaching the detectors. Most of the directions are already shielded by the 1U-casing, however, as seen in the previous section, with a wall strength of about 3 mm it is necessary to have a window cut-out to avoid losses especially in the soft part of ComPol's sensitivity.

The window cutout will be the major light contribution, but also at the interface between the 1U-casing and the 3U-backplate an intrusion of optical photons is expected. The impact of the window is mitigated by selecting a metallized protection foil, that reflects a portion of the incoming light (see subsection 3.5.2). The light, that is arriving at flat angles and would normally get reflected into the 1U-casing, is reduced by a sloped cutout in the 1U-casing and the adjacent foil holder. In Figure 3.12 the working principle is illustrated with a light ray entering at the same flat angle onto a sloped and straight cutout. They are reflected away for the sloped and inside the 1U-casing for the straight version.

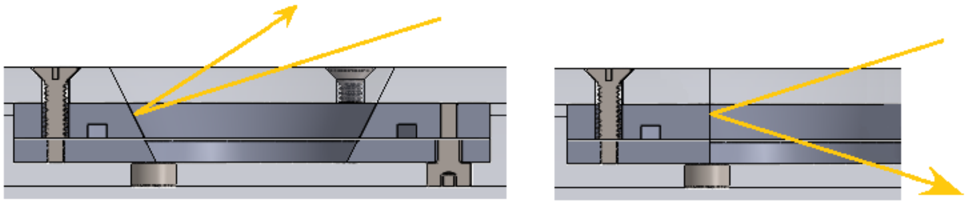

Figure 3.12: *Stray light reduction by an angled inside of the foil holder and the window cutout in the 1U-casing. Light entering at large angles is reflected away from the foil. As comparison, the same light ray is shown on the right for a straight inside. There it is reflected towards the foil.*

Preferably all photons, remaining after the baffle and the foil, as well as those entering at the 3U-backplate interface, should be blocked by the light shield between the detector PCBs, being the central part of the shielding strategy against optical photons. The size of the light shield, determining the general layout of the light shield, is discussed in subsection 3.5.1. Inside the light shield the SiPMs will be additionally shielded by a handcrafted packaging. This is still to be created by the CEA team and is therefore not regarded further. The entrance window side of the SDDs must face the window directly and thus are not incased in the light shield. Instead the standard TRISTAN-SDD was equipped with an extra layer of aluminum with a thickness of 100 nm.

3.5.1 The Size of the Light Shield

The light shield is the major component of the protection against sunlight. It is a frame of aluminum between the SDD-PCB and the $CeBr_3$-PCB, that encloses the readout side of the SDD, the calorimeter, and the veto system.

Apart from the material choice, that resulted in well-machinable aluminum, the other major design decision was the size of the light shield. The options in question were a minimally sized light shield that leaves the minimally required distance to the $CeBr_3$ and veto, or a large light shield with the outer dimensions of the PCBs, as seen in Figure 3.13 (a) and (b) respectively. The small version has the advantage, that it encloses only the volume that needs shielding from optical photons. The interface area is the smallest possible, while for the large version it is the largest possible. Additionally, the PCBs would be more easily accessible for testing and

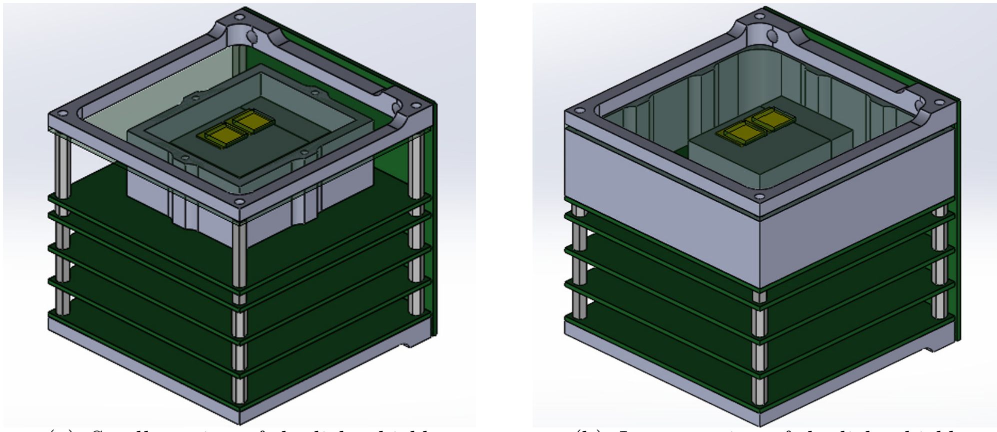

(a) *Small version of the light shield.* (b) *Large version of the light shield.*

Figure 3.13: *The preliminary CAD-designs of the light shield for the two size options, shown in the early design version 2.3 of the stack.*

debugging after the assembly.

The small design has however the major drawback that it covers a substantial surface in the middle of the PCBs. While the large light shield covers more surface in total, it does so at the edges of the PCBs, which are less important than the space in the middle of the PCB. Namely in the middle, it could interfere with the placement of the components on the SDD- and $CeBr_3$-PCB as well as the yet undefined $CeBr_3$ mounting. If deciding on a small light shield, that could block design options or necessitate intertwined design changes at a later well-advanced design state. Also, both the PCBs as well as the light shield had an ongoing iterative design process ahead, conducted by the group at the CEA ($CeBr_3$-PCB and mounting), the group at Polimi (SDD-PCB) and our group at TUM/MPP (light shield). That would call for very good and fast communication between all three groups to keep track of the changes right away and avoid incompatible designs. Even though this could be accomplished it adds a substantial amount of effort to the design process. **The large light shield version keeps the design process easier**, as it is nearly independent of the PCBs, while having the following three **additional advantages**:

- The surface of the interface can be the blank first copper layer of the PCB, without forcing the crossing signal tracks to change into another PCB layer. This improves the contact between the aluminum light shield and the PCB and avoids a leakage of light through the light-permeable solder resist (green finish) on the PCBs. Furthermore, this contact area can be put on chassis ground.

- It is possible to overlap the PCB edges and case them with a thin boarder of aluminum, as it can be seen in Figure 4.5.
- The size is already compatible with a larger $CeBr_3$ as it is planned for the final ComPol mission. This reduces the design effort at changing from ComPol-ISS to ComPol.

On basis of the above reasoning, it is **decided to implement the large light shield version** with the following **implications to be observed**:

- For testing and debugging, the PCBs must be designed such, that all test points are accessible from the outside after the assembly of the light shield.
- The decision further means that the interface between the light shield and the PCBs is much larger. That makes it generally more difficult to get it (close to) light-tight as it poses a larger area for a light leakage to occur. Therefore, the light shield interface was handled with special care during the detailed design as well as during the evaluation cycles of the light shield, that are described together in chapter 4.

3.5.2 Selection of a Partially Reflective Window Foil

The foil has the primary task to block the exhaust molecules from entering the window, but can also be used as first stage of the shielding against light. Being an option first, the results of chapter 4 make it clear, that all possible means of light reduction should be used. To perform both tasks, the foil needs to meet the following three requirements:

1. Mechanical stability and chemical robustness to comply with the primary task.
2. Good signal transmittance at least above $\gtrsim$20 keV. With the detectors having individual thresholds of $E_{min,SDD} = 1$ keV and $E_{min,CeBr_3} = 10$ keV, a small ($\lesssim$1 %) signal loss down to these energies would keep a larger energy range available for the individual testing of the detectors.
3. Shielding at least 99% of the light in the visible range ($\sim$1.6-3.3 eV) and preferably also above since all photons with an energy of the Si-bandgap or larger, can evoke e^-/h^+-pairs.

Combining those, the best option was a metallized plastic foil, that combined the stability of plastic with the reflection properties of the metal. The plastic should be a few μm to maximal 10 μm, the metal in the ranges of several tens of nm.

The commercially available plastic foils thinner than 10 μm and having a thin one-sided metallization, were pre-selected for a closer examination. They are listed in Table 3.1 and are mostly made from polyethylene terephthalate (PET). All were metalized with aluminum. The plastic PET is chemically equal to Mylar®, that is used in its biaxially-oriented variant boPET in the thermal multi-layer-insulation (MLI) protection commonly used in aerospace [54]. Therefore it should be well suited for the use in ComPol-ISS. Polycarbonat (PC) was the only other choice and was discarded due to a higher moisture absorption [55].

Carrier Material	Thickness (μm)	Al metallization (nm)
PC	2	4 Ω/square
PET	2	40
PET	2	0,7 Ω/square
PET	3,5	40
PET	4	20
PET	5	40
PET	6	20

Table 3.1: *Pre-selection of foils made from polyethylene terephthalate (PET) or polycarbonat (PC) metalized one-sided with aluminum (Al). The manufacturer information given in Ω/square is likely the specific resistance $\rho_{spec}(Al) = 2.67\ \mu\Omega\cdot cm$ divided by the area of the foil, but was not explicitly defined.*

As a first selection step, the shielding of optical photons was investigated. The foil should block at least 99% of the optical light.
The complex refractive index $k(\lambda)$ of aluminum as well as PET was exported from [56]. From that, the absorption coefficient μ was calculated by

$$\mu = 4\pi \cdot \frac{k(\lambda)}{\lambda} \tag{3.1}$$

for all wavelengths λ. For a specific thickness d of the material, the transmittance is then

$$T = \frac{I}{I_0} = \exp(-\mu \cdot d). \tag{3.2}$$

The compliment of the transmittance $(1 - T)$, that is the shielded fraction of photons, is displayed for the two available thicknesses 20 and 40 nm of aluminum in Figure 3.14. The absorption of a few μm of PET was found to be negligible compared to the reflectively of the aluminum metallization. The foils with a 20 nm layer of aluminum shield less than 96% of the incoming light and are therefore discarded as options. The 40 nm reaches even down to transmitting only 0.3% of the light, and was a perfect match.

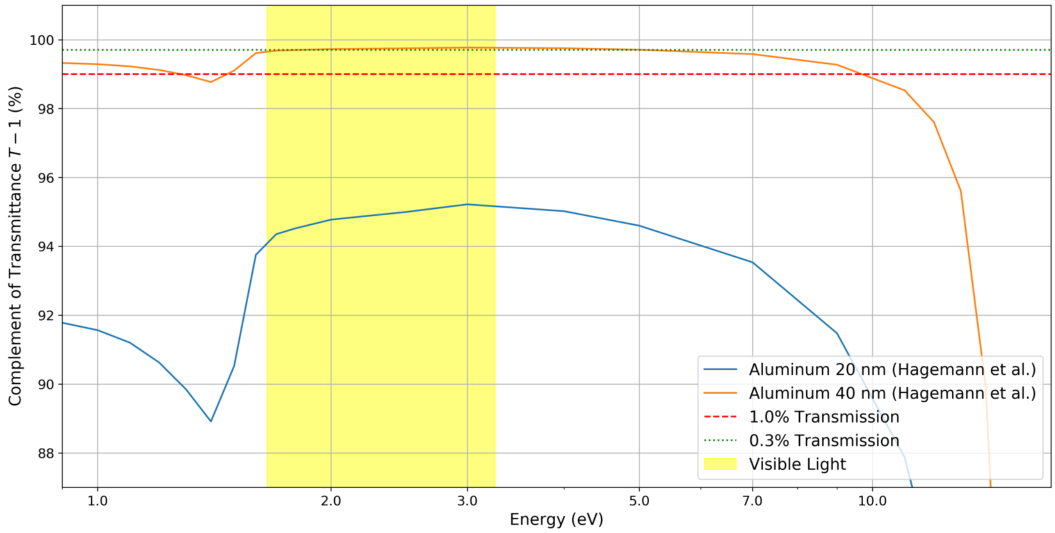

Figure 3.14: *Reflected fraction of photons in the optical range and nearby IR, UV region for the available aluminum thicknesses. The transmittance T was calculated from the complex refractive index k measured by Hagemann et al. [57].*

This narrowed the foils down to PET thicknesses of 2, 3.5, or 5 μm, see Table 3.1. The next step of the selection was based on the second requirement: The X-ray absorption of the foil should be reasonable small. Therefore, the transmittance of the foils was calculated on basis of the data available at the NIST X-ray attenuation database [52]. There, the mass attenuation coefficient μ/ρ of a great number of materials is given (in in cm^2/g). From the data for "polyethylene terephthalate (Mylar)" the transmittance was calculated through Equation 3.2 with a density of 1.38 $\mathrm{g/cm}^3$ for the different thicknesses d and displayed as $1-T$ in Figure 3.15 together with the 40 nm aluminum values obtained above from Hagemann et al. The absorption of the few μm thick PET dominates, being about one order of magnitude larger than the absorption of aluminum. Above 6 keV all available foils transmit more than 99% of the incoming X-ray radiation. In the sensitivity range of ComPol, the absorption even drops below 0.03% before 30 keV in all cases. Therefore, the thickest and therefore most robust foil was selected: 5 μm PET with a one-sided metallization of 40 nm aluminum.

3.6 Design Decision Summary and Further Steps

A well-advanced and near to flight ready stacked model was designed. With a 3D-printed mock-up the assembly and compatibility in size was verified. Recently, the

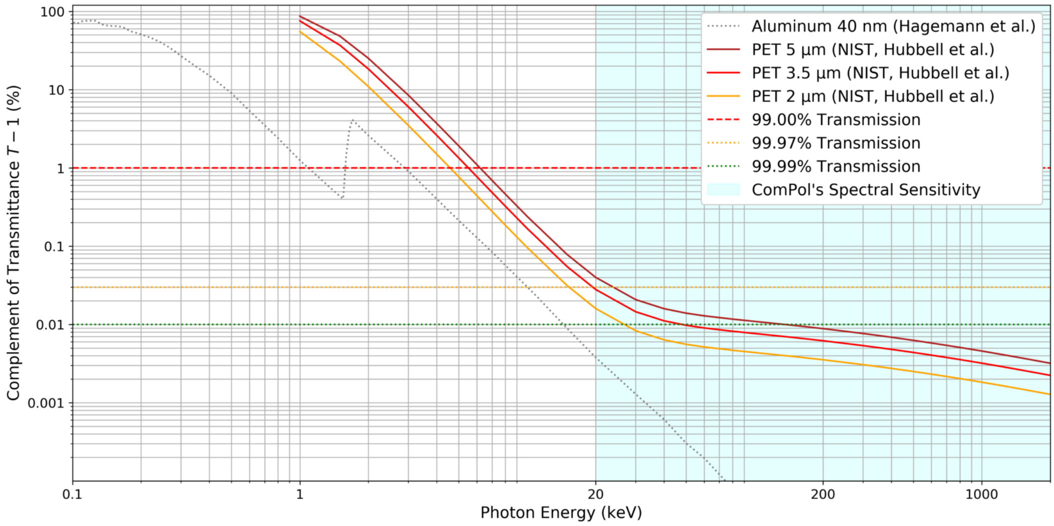

Figure 3.15: *Absorbed fraction (1 - transmittance T) of X-ray radiation going through PET foils of different thicknesses, as calculated from NIST data [52]. The values for aluminum are shown as reference and are calculated from [56, 57]*

change from the stacked version to a slide-in version was issued, making the backplane fitting easier as well as enhancing the modularity. Though the mounting structure of the stacked model become obsolete through the change, the important design decisions remain unaltered:

- The common PCB size is set to 90 x 90 mm^2.
- A common ComPol-internal backplane and the 90° high density SAMTEC SERAY connectors are used to connect the boards, except the two $CeBr_3$ boards that are connected directly.
- The distance of the SDD and $CeBr_3$ is defined to 6.1 mm.
- The light shield has the full PCB size.
- The window size is confined to a straight line of sight from the SDDs, by the foil holder with an inner diameter of 18 mm.
- The exhaust protection foil is selected to be a 5 μm PET plus 40 nm aluminum foil and will act as a first light protection stage with a light reduction to less then 0.4% of the incoming light.

- The foul will be mounted to the 1U-casing with a modular foil holder, that forms a baffle together with the window cutout. The field of view will be defined by the yet flexible slope of the baffle.

The following steps are necessary to evolve from the current prototype to a flight-ready model:

- Design the slide-in frame including mounting points for the subsystems.
- Definition of the field of view by choosing the baffle slope.
- Test of the foil mounting, verification of the low X-ray absorption, and evaluation of the cleanness after laser cutting.
- Cutouts in the wall of light shield[12] to reduce it's weight from currently 160 g (for the aluminum alloy 7075-T6 (SN), that is often used in aerospace applications) to a minimal achievable weight.
- Protection cap covering the window from the outside, to protect the foil during transport and launch. This cap is to be removed by an astronaut at the ISS after installation at the multi-payload adapter.

[12] After the mounting points of the light shield are defined.

Chapter 4

Light Shield Design and Evaluation

The light shield is the most essential part of the shielding concept against optical photons (section 3.5). Its purpose is to protect the SiPMs of the calorimeter and of the veto system as well as the readout side of the SDD from the light that reaches the inside of the box[1]. In subsection 3.5.1 an overview about the general design questions and conceptual layout was given. The more specific requirements and design solution are introduced in section 4.1 and section 4.2.

This is followed by a series of light-tightness measurements with a SiPM setup as described in section 4.3. The subsequent sections reflect the iterative approach of testing and tailored improvements of the design and are structured as follows. First, section 4.4 will cover the basic photo-current tests that were undertaken to answer specific design questions which guided the improvement of the light shield from not light-tight to close to the dark condition. The resulting best configuration is subsequently examined deeper in section 4.5, where also additional findings of the photo-current tests were addressed. Finally, in section 4.6 the light shield was evaluated in a high luminosity environment provided by a solar simulator.

4.1 Venting Requirement and Meander Solution

ComPol-ISS will go from atmospheric pressure (inside the ISS) to vacuum conditions (external platform). Therefore, besides being as light-tight as possible, the light shield is not allowed to be gas tight. The gas from the interior of the light shield must be able to escape during the pressure reduction in the air lock. The area, necessary for a fast enough venting is defined by NASA standards via the so called *Maximum Effective Vent Ratio (MEVR)* [58]. The fraction of the enclosed volume $V_{internal}$ and the effective vent area $A^{eff}_{venting}$ is not allowed to exceed:

$$MEVR = \frac{V_{internal}}{A^{eff}_{venting}} \leq 5080\,\mathrm{cm} \tag{4.1}$$

[1] Light that passed through the foil or entered at the interface between box and 3U-backplate.

The solution implemented to meet this requirement, while achieving the necessary light-tightness, is a **meandering venting hole** milled into one wall of the light shield, see Figure 4.1. This meander allows the gas to flow from the light shield interior to the outside. Photons entering from the other side need to be reflected multiple times, to make it into the light shield. From the outside the meander is lidded by a thin aluminum cover leaving only a hole on the outer end of the meander. The cover is accommodated in a rectangular groove around the meander and fits flush with the outer light shield surface. Countersink M1.6 screws are used to hold the cover tightly. Depending on the wall thickness the screw holes reach the interior of the light shield and must be checked against their potential light leakage.

Figure 4.1: *Photograph of the venting meander milled into the light shield wall. The rectangular cutout accommodates the cover with a hole to access the meander.*

The full length of the light shield was used to achieve the maximum number of windings, since untreated aluminum reflects light and the production effort[2] was only negligibly larger. Each additional turn reduces the probability that light is reflected all the way through. A further option was to anodize the aluminum to turn black. That would reduce the reflectivity but also brings the disadvantage of an additional production step as well as a roughening of the surface [59]. The later could negatively affect the light-tightness at the interface with the readout PCBs. Therefore, the performance of an untreated aluminum part was tested first.

The **cross-sectional size of the meander** was determined to be 3.8 mm^2 by means of approximating an upper limit of the interior volume while creating the **first light shield design**. This design is shown in Figure 4.2 and will be explained in the following together with the specifications made to arrive at the meander size. The 90 x 90 mm^2 sized PCBs are framed by a 1 mm thin border, to block the light arriving sideways at the interface between PCB and light shield and to facilitate the mounting

[2] Programming of the CNC mill.

of the PCBs. Together with a small tolerance to avoid double fit[3] this results in an outer dimension of 92.2 x 92.2 mm^2. The thickness of the wall is a trade-off between

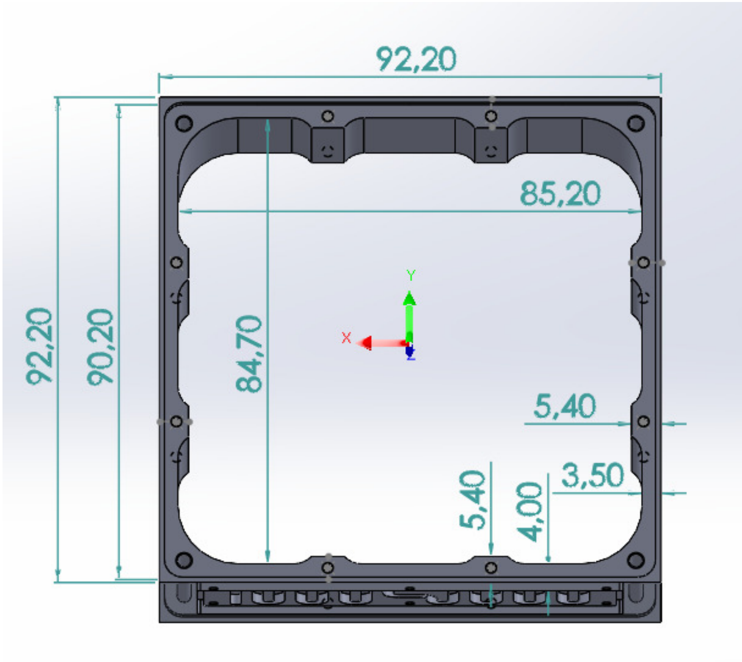

Figure 4.2: *First light shield design with measurements that were used to calculate the internal volume.*

the surface area of the interface, that establishes the light-tightness, and the usable area on the PCB. In the first design, which is shown in Figure 4.2, a deliberately thin wall strength of 3.5 mm was chosen. Since this represents the smallest still sensible interface area, the internal area is maximized resulting in the largest minimally[4] required venting area $max(A^{eff}_{venting})$.

The mechanical connection between the light shield and the PCB is established by eight M2 screws for each PCB and four M3 screws through the edges. The M2 screws need more space than available in the 3.5 mm wall. Instead of a thicker wall the screw holes are placed in protrusions. Firstly, this keeps the usable PCB area as large as possible and secondly, it also helps with the overall weight reduction. Only the wall with the meander needed to be thicker to accommodate the cutouts for the

[3] A douple fit is a type of construction error (German Doppelpassung) that occurs when two components are in contact with each other at more than one parallel surface without appropriate tolerances. Unavoidable production deviations would lead to fit problems.

[4] *Minimally required* since the effective venting area is allowed to be larger than required. *Largest required area* since the considered internal volume is an upper limit.

meander and the cover groove. For the calculation of the upper limit of the internal volume, the protrusions are neglected. Thus Equation 4.1 becomes

$$max(A^{eff}_{venting}) \geq \frac{max(V_{internal})}{5080\,\text{cm}} = \frac{85.2 \cdot 84.7 \cdot 25\,\text{mm}^3}{50800\,\text{mm}} \approx 3.55\text{mm}^2 \tag{4.2}$$

and $A^{eff}_{venting} = 3.6$ mm^2 was adopted as mminimum venting area for the maximum volume. Rounded to sensible accuracy a circular hole needs a diameter of 2.2 mm to exceed this area. Therefore the realized venting area is set to $A_{real} = 3.8$ mm^2. For a cylindrical milling head the cross section in the x-y-plane is a rectangle. To allow a one-directional cut with a typical 2 mm milling head, a depth of 1.9 mm is chosen to match A_{real} as defined by the hole.

Additionally, it should be added here, that also the surrounding 1U-casing as shown in chapter 3 must be vented. Since this box is the first stage of the photon shielding concept, it depends on the performance of the light shield, if that venting must be designed light tight or if one or more open venting holes can be used. If a multi-staged light reduction is needed, the 1U-casing could also be vented with a meander. That however would need to be considerably larger. The best position will be probably right at the bottom of the instrument (opposite of window, facing Earth) or included in the 3U-backplate.

4.2 The PCBs and their Interface to the Light Shield

Besides the meander, the second important design question concerned the light-tightness of the PCBs themselves and the interface of the light shield and the PCBs. PCBs are made of thin copper tracks divided by layers of an insulating substrate and coated with a mask of solder resist on the outside. The most common substrate, that will also be used for ComPol-ISS is the fiberglass epoxy composite FR4. Both, solder resist and FR4, are permeable to light. To make the PCBs light-tight it is necessary to include a **continuous copper plane**, which is set to ground potential. The signals of the SDD and $CeBr_3$ detectors arrive at the copper tracks on the side facing the interior of the light shield. They must be passed through the ground plane by means of wire connections to the outside of the respective PCB, where they are transferred by electrical connectors to their further readout systems. Simple through hole vias are not light-tight. Instead blind vias must be used. The difference is shown in Figure 4.3.

For the **interface between the PCB and the light shield** four reasonable design options were identified. In the following list, they are described in ascending order of complexity. Common to all options is the flat interface area on the PCBs, that is left without solder resist to have a plain metal surface.

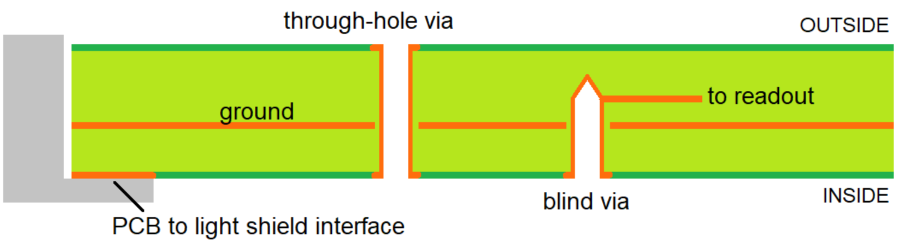

Figure 4.3: *Sketch of a PCB cross-section illustrating the PCB structure made of FR4 (light green), copper (orange) and solder resist (dark green). The continuous ground plane is needed for the light-tightness. Blind vias are the light-tight alternative to the standard through-hole vias. Also shown is that the solder resist is omitted at the interface to the light shield.*

1. **Flat interface:** The blank copper area at the edges of the PCBs is pressed onto the flat aluminum contact area by the 12 screws per PCB described above.
2. **Push-down frame:** Flat interface with an additional frame on top of the PCBs to enhance the strength and uniformity of the pressure applied to the contact between the two metal surfaces.
3. **O-ring seal:** Groove with an elastic black seal ring. Disadvantage: needs a thicker wall to accommodate the groove.
4. **Sharp-edged interface:** Small sharp elevation in the contact area of the light shield that cuts in the copper of the PCB to form a very tight metal-to-metal seal (like in CF flanges for high vacuum applications). Disadvantage: Not re-usable due to the deformation of the copper layer of the PCB.

It was decided to start with the simplest and to move down the list of interface options if it is not sufficiently light-tight.

4.3 Experimental Approach and Setup Overview

For the measurement of the light-tightness, the SDD and CeBr3 readout PCBs are replaced by dedicated light test PCBs. As sensors, SiPMs were selected to probe the light-tightness, since they are more sensitive to light than the SDDs. In addition to the photo-electron (p.e.) spectrum (see SiPM paragraph in subsection 2.2.4) that is acquired for a specific time-span and quantified during the subsequent data analysis, the SiPMs also bring the advantage of an immediate quantitative response in form of the photo-current. The later treats the SiPMs as photodiodes and is not the classical way to read out SiPMs. The comparison of the photo-current with the dark current is however the simplest and most immediate approach to answer if the design is light-tight in the first place. Once the design reaches the dark current, p.e spectra are recorded in the dark and illuminated conditions to provide a closer look. The p.e. spectra allow to answer, with higher statistics and an intrinsic average over time, how light-tight the design really is for different levels of illumination.

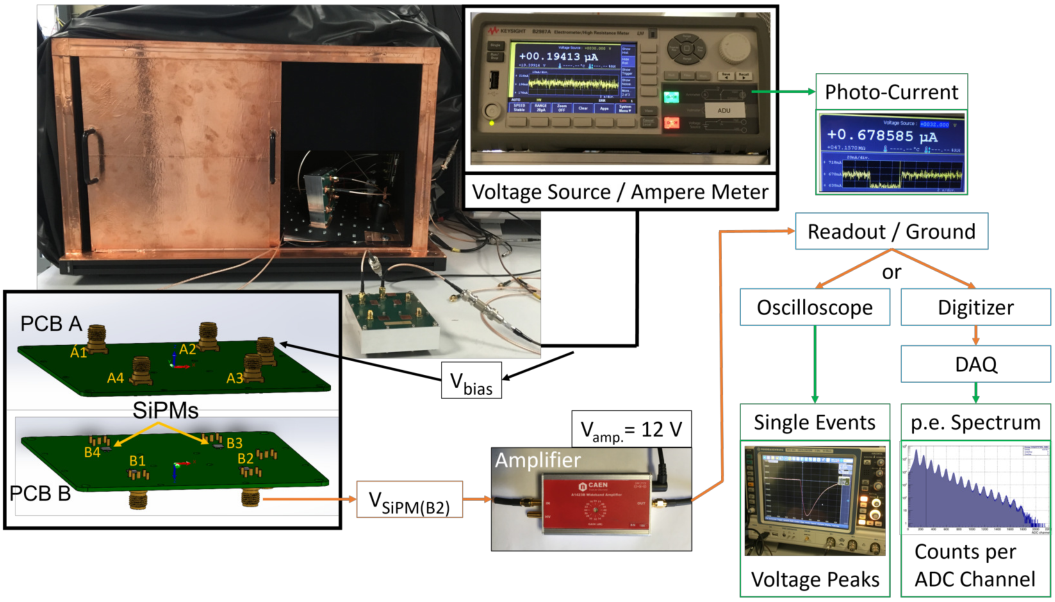

Figure 4.4: *Overview about the light-tightness measurement setup.*

The following paragraph gives an overview about the general setup, as shown in Figure 4.4. The measurement-specific details are described in the respective sections. The light-test PCBs are biased with a KEYSIGHT B2987A Electrometer/High Resistance Meter that acts as a voltage source and ammeter at the same time. The SiPMs used for the light-test are different from the final $CeBr_3$ readout. They are from the KETEK PM3325-WB-B0 series that has an active area of 3.0 x 3.0 mm^2, a nominal breakdown voltage of $V_{BD} = 26.9$ V and a peak photo detection efficiency at 430 nm of $max(PDE) = 43$ % for an overvoltage of $V_{OV} = 5$ V [60]. Each PCB holds four SiPMs, with a preceding RC circuit to filter potential noise on the supplied voltage. These four SiPMs provide redundancy and a mutual crosscheck. Furthermore it leaves the possibility open to read out the combined signals of several SiPMs at a later stage. The measurements in this thesis, however, were all conducted with one SiPM at a time. This keeps the approach simpler and matches the readout of the calorimeter, where the threshold is currently also set for one of the SiPMs to cross the value of 4-5 photons.

In the early design evaluation the light-tightness was read from the KEYSIGHT ammeter, in the second part of the evaluation, the signals from the SiPM were amplified by a CAEN A1423B Amplifier set to a gain of 54 dB. The SiPMs were positively biased (holes from the e^-/h^+-pairs are readout at the anode) but the CAEN amplifier inverts the signals. Subsequently either the negative voltage peak can be viewed on the oscilloscope or the height of the peak is digitized into ADC channels and recorded by the data acquisition system. As introduced in the SiPM paragraph, the p.e. spectrum is the histogram of these signal heights, that correspond to the number of fired SiPM micro-cells.

4.4 Photo-Current Tests of Meander and Light Shield to PCB Interfaces

In the first design evaluation, the photo-current of the SiPM for different illumination conditions were compared to the dark current to address the main design questions (see subsection 4.4.1). The used light sources are described in subsection 4.4.2 . The subsection 4.4.3 briefly discusses the performance of the initial design and leads to the further investigations of the light leakage in subsection 4.4.4 and different design configurations in subsection 4.4.6.

All photo-currents of this chapter were manually read from the KEYSIGHT ammeter. Natural **fluctuations of the current** were treated in the following way: Where reasonably precise, the displayed current was **rounded to the first non-fluctuating digit**, in all other cases the **range of the fluctuation** was observed for at least one minute and the typical[5] **minimal and maximal values** were noted.

4.4.1 Measured Dark Current and Main Questions

The SiPMs were biased with $V_{bias} = 30$ V, what is equivalent to an overvoltage of $V_{OV} \sim 3$ V. In the closed dark box without illumination, a dark current of ~300 nA was expected. This was confirmed by a **measured dark current of ~250 nA** consistently for both SiPM 1 and 2 on PCB-A (shortly named A1 and A2). After this initial readability check, the current of SiPM A2 was used as a measure (relative to the dark current range) to address the following **main design questions**:

- Is the light shield capable to reduce the light to the order of the dark current?

[5] When high/low currents occurred very briefly, these values were suspected to be outliers. In this case the observation time was slightly prolonged and the specific value reject unless it reoccurred.

- Is the meander in aluminum sufficient? Or is a reduction of the reflectivity by means of anodization needed?
- Which interface between PCB and light shield is sufficient?
- Are screws problematic? Or do the screw threads act as mini-meander?

To answer the question about the screws independently from the interface question, four M2 screws were implemented in the middle of the test PCB (see Figure 4.5).

4.4.2 Light Sources for the Photo-Current Evaluation

For the illumination during the photo-current measurements two readily available **light sources** were used:

- **Ambient diffuse light** from the laboratory ceiling lamps.
- **Directional illumination** from a phone LED inside the dark box. Manually focused or fixed at a defined distance depending on the specific test.

For both sources, the illumination intensity is not known. The LED of the used iPhone SE (1st generation) can be vaguely inferred to be in the range of 5-26 lm (lumen) by means the information drawn from technical Q&As about the precursory and succeeding phone models [61, 62]. For the laboratory light no such estimations are available. To find first answers to the above questions, however, it is not necessary to know the exact illumination. Not the absolute value of the photo-current, but the comparison relative to each other and to the dark current is decisive. For the more precise characterization by the later obtained p.e. spectra (see section 4.5 and 4.6) clearly defined illumination sources were procured (see subsection 4.5.1 and 4.6.1).

4.4.3 Performance of the Initial Design

The initial light shield design, has the simple flat interface, as introduced in section 4.2 with the dimensions as shown in Figure 4.2. In Figure 4.5 the first manufactured version is shown (a) in the partially and (b) in the fully assembled state. In (a) the SiPM placement relative to the soldered through-hole connectors can be seen. Also visible is the interface border without solder resist. Figure 4.5 (b) shows the closed meander cover, with the venting hole clearly visible. The four copper tape strips on the PCB cover the through-hole vias that were used for the first iteration of the measurement PCBs for two reasons: 1) to verify the assumption that they have a strong influence on the light-tightness and 2) because of better production availability. The vias were taped, after an **excessive light-leakage from the through-hole vias** was confirmed visually.

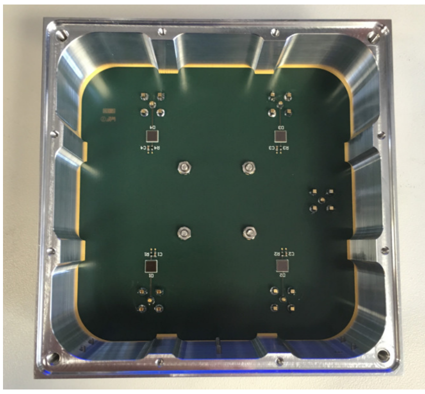

(a) *Inside*

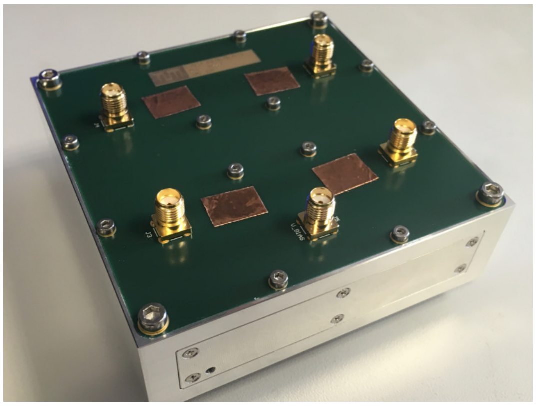

(b) *Outside*

Figure 4.5: *First Light Shield Iteration with the flat interface. (a) shows the inside of the light shield, with the visible blank copper at the edges of the PCB and the placement of the SiPMs with respect to the electrical connectors. In (b) the light shield is assembled with the meander cover and meander opening hole visible on the side. The copper tape covers the through-hole vias.*

In the configuration as seen in Figure 4.5 (b) the light shield was now tested against the dark current of ~0.25 μA under different light conditions. In the back corner of the dark box, while the door was open and PCB-A (carrying the read out SiPM A2) was facing the door, the remaining laboratory light, that was scattered into the dark box resulted in a current of 250-300 nA, being in the range of the dark current. **Low illumination by stray light is shielded well**. The next step was to move the light shield setup nearby the open door. Ergo a photo-current of $\sim 1\,\mu$A was measured. Placing the setup on the table (PCB-A pointing up), the **full illumination** by the laboratory light showed a **strong light leakage** of 6-7 μA. Placing it back to the dark box corner and illuminating the setup directly with the phone light, it even exceeded 7 μA.

Since the initial configuration was so clearly deviating from the light-tight condition, the further photo-current measurements were structured in these two stages:

1. Searching the cause of the light leakage by temporarily covering or taping the suspected areas (subsection 4.4.4)
2. Step-wise change of the light shield interface design (subsection 4.4.6)

4.4.4 Study of Light Leakage Causes

In the following, the suspected sources of the clearly observed light leakage were systematically probed by covering of the respective areas. The Table 4.1 summarizes the measured photo-current I_{ph} for the most important combinations of copper taped areas and light source, including the initial findings as reference. In the column *Covered Areas* the the newly added areas are listed. All previous listed areas stayed covered. The observations and their respective conclusions are discussed below in a list-like structure with the respective numbers referencing to the entries in the table. Afterwards, the individual results are combined in an intermediate summary, that motivates the further steps.

No	Covered Areas	Light Source	$I_{ph}(\mu A)$
Dark	only vias	closed dark box	~ 0.25
Ref-1	no change	dark box corner, open door	0.25 - 0.30
Ref-2	no change	dark box near open door	~ 1
Ref-3	no change	on table at lab light (PCB-A up)	6 - 7
(1)	+ PCB-A edges + 8x M2 screw holes	same as row above	~ 3.5
(2)	+ PCB-B edges + 7x M2 screw holes (all except one)	same	3.0 - 3.5
(3)	no change	at lab light, slightly lifted from table to reduce the shadow	> 11
(4)	+ middle screws + M3 screws	lifted from table, PCB-B up	~ 9.9
(5)	+ 1x M2 screw hole (missing one)	same	~ 9.1
(6)	no change	on table at lab light	~ 3.5
(7)	no change	dark box corner, LED focused only on meander and countersink screw	0.27 - 0.28
(8)	no change	same position, but LED focused on one connector	~ 6
(9)	+ all PCB-A plugs	on table (PCB-A up)	1.6 - 2.0
(10)	no change	dark box near open door	0.29 - 0.38

Table 4.1: *Excerpt of the photo-current measurements for different settings and the respective conclusion. The covered areas are to be understand cumulative.*

(1) Covering the edges and all M2 screw holes on the up-looking PCB-A, similar to Figure 4.7 (a), halved the photo-current and reduced the fluctuation.

Result: **The edges are a major leakage source.** The light excess in Ref-3 can either be explained by light entering at the screws heads and scattering further into the shielding through a bad contact of the flat interface (see Figure 4.6 (a)), or by light entering the tolerance gap and scattering under the continuous ground plane into the shielding (see Figure 4.6 (b)), or a combination of both.

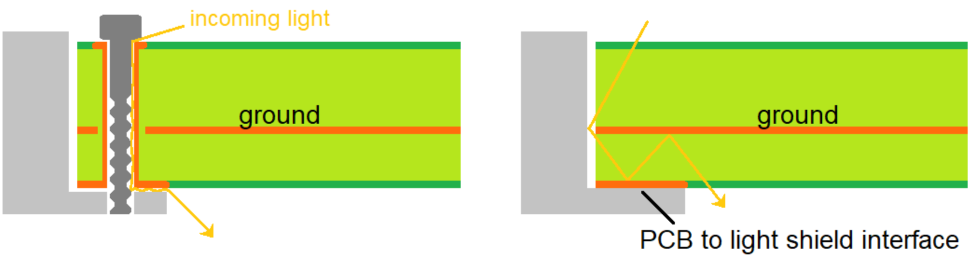

(a) *How light could enter at the screws.* (b) *How light could enter below the ground plane.*

Figure 4.6: *Illustration of the potential causes of the light leakage at the PCB edges. The gap between the light shield border and the PCB is called the tolerance gap.*

(2) The edges of PCB-B were taped as well as the M2 screw holes except of one, as shown in Figure 4.7 (a). This was meant to distinguish between light entering under the ground plane (only possible through the tolerance gap) or through the screw holes[6] and interface (ground plane excluded because holes are metallized on the inside). This taping showed surprisingly less impact than the PCB-A taping. The photo-current was only marginally reduced, if significant at all.
Result: Either the leakage of one single M2 hole dominates over the leak from the edges, or it is not reduced because it is placed on the table, with PCB-B facing down. The table is white and reflects the laboratory light partially, but the largest part under the light shield is shadowed by itself.

[6] In the assembled state, the holes would be masked by the screws. Therefore it was decided to leave only one hole open at a time

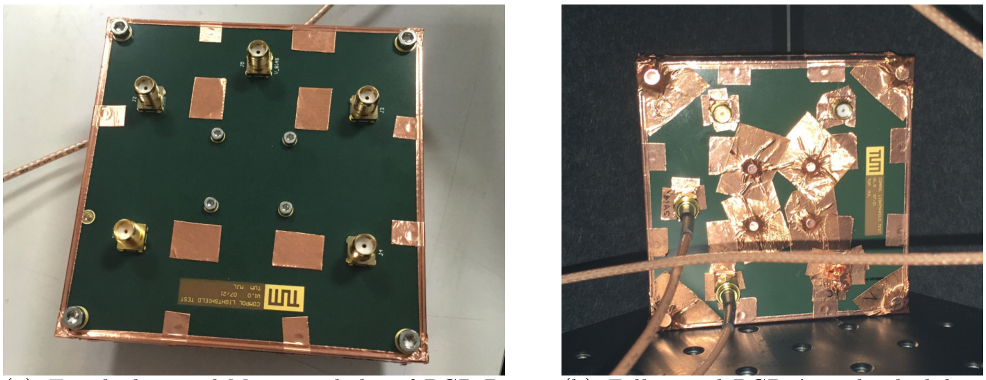

(a) *Taped edges and M2 screw holes of PCB-B.* (b) *Fully taped PCB-A in the dark box.*

Figure 4.7: *Copper tape was used to investigate the origin of the observed light leakage. (a) The PCB edges were taped to close the tolerance gap between the PCB and the light shield protrusion. The M2 screws were removed as they were placed very close to the gap and the empty screw holes were taped. The figure shows PCB-B with the taping of measurement (2). The hole, next to the SiPM B1 connector, was left open until measurement (5).*
(b) The taping was step-wise extended to all screws and the surroundings of the electrical connectors. This figure shows the setup in the corner of the dark box with the final taping attained in (9).

(3) To check if the observation of (2) could be explained by the placement on the table and to distinguish between the two hypothesis that could explain (1), the light shield was slightly lifted from table to reduce the shadow. The additional light that was now reflected by the white table led to an enormous increase of I_{ph} even above the reference measurement Ref-3.
Result: Even without the possibility to enter below the ground plane, the light leakage exceeds Ref-3. This can be explained since PCB-B was now not shadow-shielded anymore and the light, reflected from the table added to the illumination from above. Since the placement on the table has such a strong impact on the illumination reaching PCB-B, it is likely that the non-reduction of the light leakage in (2) is caused by the placement on the table. With this measurement however, it is not possible to conclude if the screw holes or the tolerance gap is the origin of the edge leak.

(4) A quick test, how much one M3 screw contributes to the leak, showed a reproducible drop of $\sim 0.5\,\mu$A, when it was temporarily covered / uncovered with a thumb. All eight M3 screws and the eight middle screws were taped without removing the screws. Now I_{ph} was measured to be $\sim 9.9\,\mu$A for when the setup

was lifted from table and turned so that PCB-B was facing up.
Result: When compared with (3) this **confirmed the contribution of the screws** to the leakage, but also showed that it is neither the only nor the dominant contribution. Still, a single screw can lead to an excess of about twice the dark current.

(5) The last open M2 screw hole was covered and resulted in a drop of $\sim 0.8\,\mu$A under the same illumination.
Result: The light that makes its way to the interface is not sufficiently blocked by the flat contact between the PCB copper and the light shield aluminum. **The flat interface is not light tight.**

(6) When placed and illuminated like in (1) and (2), the photo-current is back to the same level as in (1).
Result: While configuration (1) was clearly distinct from Ref-3, the additionally taped areas up to configuration (6) did not show a change. Firstly, this means that the slight reduction in (2) was likely not a significant change. Secondly, the leak of the M3 and middle screws, that was confirmed with the illumination of PCB-B in (4), is not visible for PCB-A. Since there is no difference that would prevent the same leak happening at the screws of PCB-A, it can be concluded, that the light entering under the ground plane of PCB-A arrives better at the SiPM A2, than the light entering at the screws of PCB-A. In this case, the leak at the screws would happen on PCB-A too, but would be nearly invisible. The same should then be true for the M2 screws on PCB-A and the difference between Ref-3 and (1) does only marginally come from the M2 screws. The light entering **the tolerance gap indeed contributes** to the light leakage. Thirdly, the light excess of $\sim 3.5\,\mu$A does not originate from the areas covered during (2)-(5) and a different cause must be found.

(7) The configuration was left unchanged and placed in the back corner of the dark box. There the phone LED was focused with a roll of black paper onto the meander opening and the nearby countersink screw. The observed current was consistent with the dark current and had only a low level of fluctuation.
Result: **The meander and its cover is light-tight** despite the reflective aluminum. The light shield does not need to be anodized.

(8) With the same approach, the LED was now focused on one of the soldered through-hole connectors.
Result: The sudden increase of the photo-current evidences that the used **electrical connectors are not light-tight.** This was an unexpected finding since the solder seals the through-hole and a penetration through the hole similar to Figure 4.6 (a) should not be possible. The only explanation would be that the

light leak stems from the gap between the ground plane and the through hole, which must be there to separate the signal and from ground.

(9) To confirm the observed leak, the surroundings of all connectors on PCB-A were taped, like shown in Figure 4.7 (b), but placed on the table as in (6). The current evoked from the laboratory light was reduced by at least 1 μA, at best 2 μA compared to (2). When the gap between the table and the PCB-B was roughly shielded with bare hands, I_{ph} repeatedly dropped below 0.9 μA.
Result: The strong impact of the connectors was confirmed.

(10) As comparison to Ref-2, the setup was placed in the dark box next to the open door, where it previously had about 1 μA. PCB-B, whose connectors were not taped, was facing away from the door to have only a diffuse illumination. Even though they were not fully covered, the partial shade was sufficient to reach 0.29-0.38 μA.
Result: For the illumination level present at the open door of the dark box, the fully taped version reduced the detected light to about a third of the initial version and achieved the level of the dark current. To accomplish this without copper tape, all investigated leaks must be addressed in an improved design.

4.4.5 Intermediate Summary and Necessary Steps

The above excerpt of the conducted photo-current measurements made clear that the light-leakage does not have a single, but multiple origins.
1. The meander and its cover including the countersink screws were found to be light-tight even for the directly applied illumination of the phone LED.
2. The strongest contribution to the observed light leakage of 6-7 μA originated from the edges of the PCBs. Taping the edges and M2 screw holes, a reduction by at least 2.5 μA and at most 4.0 μA was achieved, what corresponds to 36 - 67% of the initial leakage. Both sources that could explain this leakage, which are illustrated in Figure 4.6, were confirmed to contribute at least partially to the leakage. While the leak from the tolerance gap dominates over the impact of the screws[7] on the PCB with the measuring SiPM (PCB-A), the impact of the screws cannot be neglected. For the PCB opposite to the SiPM (PCB-B) a contribution of the M3 and middle screws of about 10% was measured. Taken by themselves one of the M3 screws can already increase the current by about twice the dark current. Only the countersink screws were found to be light tight. Additionally, it was found that the flat interface does not sufficiently shield light, once it is arriving at the contact surface.
3. The second most important leak originated from the electrical trough-hole connec-

[7] That is confirmed for the M3 and middle screws and thus likely also true for the contribution of the M2 screws.

tors. Covering them resulted in a further reduction of 1.0 - 1.9 μA, that is 14 - 32% of the initial leakage.

Necessary steps:

To achieve light tightness, it is necessary to test the alternative interface options, introduced in section 4.2. The screws, that fixate the PCB on the interface protrusion of the light shield must be either countersink screws[8] or placed outside of the sealing component of the interface.

Since the usual manufacturing process of the PCBs does only allow clearance holes (not made for countersinks), screws on the PCB besides the ones outside the sealing interface should be avoided where possible. Where necessary they must be shielded by other means. Of the considered shielding options, rubber washers were excluded since their squeezable nature leads to an ill-defined seating. The remaining possibilities are to use black Locktite to block the light in the screw thread, or to cover the screw heads with black epoxy. Since Locktite is actually to fixate screws in threaded holes and not made for clearance holes as in the PCBs, the epoxy solution is recommended.

To prevent a penetration below the ground plane (Figure 4.6 (b)) the edges of the PCBs can be metallized as shown in Figure 4.8. The impact of the electrical connectors has to be addressed by a change to surface mounted connectors.

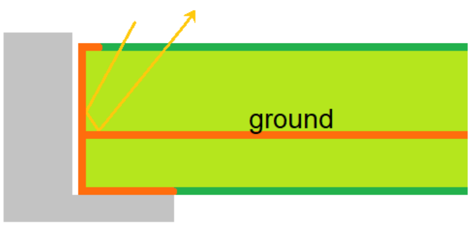

Figure 4.8: *Illustration how a PCB with metallized edges inhibits the penetration below the ground plane compared to Figure 4.6 (b).*

A new iteration of test-PCBs with surface mounted connectors, blind/shrouded vias, and metallized edges must be designed. However, the PCB borders are adapted to the respective interface layout, so that in the following section the sufficiently tight interface between PCB and light shielding will be identified first.

[8] The M1.2 countersink screws of the meander cover were light tight. It is inferred that this is due to form of the screws. If larger countersink screws are used, they still need to be tested for their light-tightness.

4.4.6 Study of Different Interface Configurations

To find the simplest still sufficient interface between the PCB and the light shield, the list of interface options (see section 4.2) is worked through starting from the top. In the previous section it was found that the simple flat interface (see Figure 4.5) was not sufficient. In the following the taped version of the flat interface (see Figure 4.7 (b)) is compared with a version where a push-down frame was added on top of the flat interface (see Figure 4.9 (a)) and a completely new light shield version with an o-ring interface (see Figure 4.9 (b)). The sharp-edged interface was not examined.

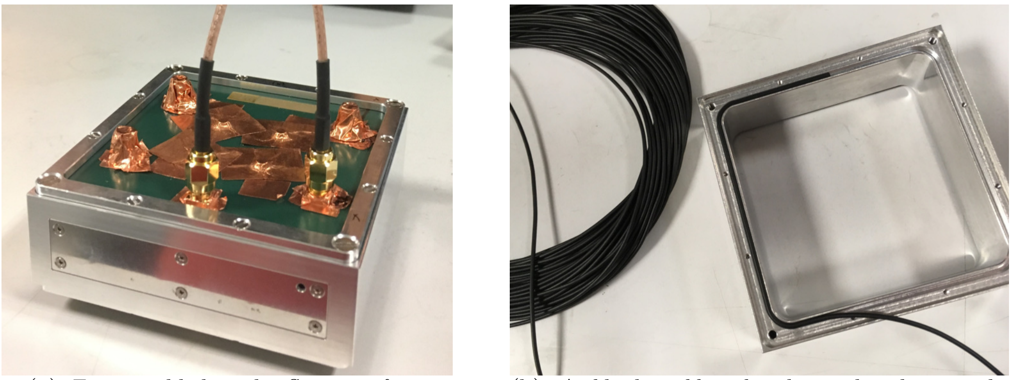

(a) *Frame added to the flat interface.*

(b) *A black rubber band is placed into the groove of the o-ring interface.*

Figure 4.9: *These two interfaces were compared with the flat interface and a transitional configuration.*

The push-down frame is flush with the inner side of the 1 mm border and conceals most of the tolerance gap. However, it does not seal it completely. Mechanically it is not possible to let it cover both the PCB and the 1 mm border without constructing a trouble causing double fit. The push-down frame is held in place by M2 and M3 countersink screws. For the o-ring interface, the wall of the light shield needed to be widened to fit a groove for 1.5 mm diameter of rubber band. The screws are all placed outside this sealing ring to avoid a leakage through the screw holes. The exact dimensions of this light shield design can be found in the mechanical drawing Figure 2 of the appendix.

For the illumination again both the directed light from the phone LED as well as the diffuse laboratory light were used. To have a reproducible illumination that allows comparrison of the different interfaces, the position of the light shield were marked in the dark box and on the table, respectively. Since auxiliary mea-

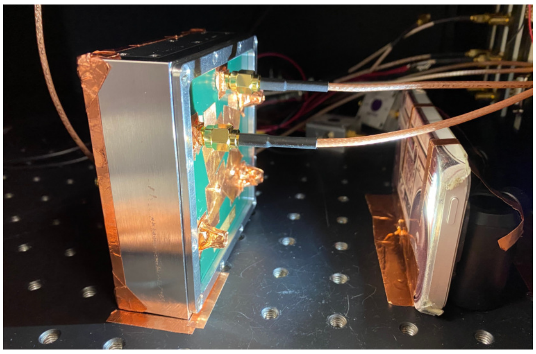

Figure 4.10: *For reproducible measurements, the position of the light shield configuration was marked. The phone was fixed in a position that aligns the LED with the vertical position of the readout connector of the used SiPM A2 (left top). For the measurements with PCB-B facing the LED, the light shield was rotated in a way that the A2 channel was on the back left top (the bias connector on the side of the door).*

surements showed that the illumination impact was strongest when the LED was directed towards readout connector of the biased SiPM, the phone was fixed such that the LED was aligned with the vertical position of this connector, see Figure 4.10.

The measurements in the previous chapter showed clearly that there is a distinction between the illumination of PCB-A and PCB-B. Therefore, in the interface test, the photo-current was measured for both sides sequentially. The dark current was also remeasured in the beginning and the end of the measurements to have typical values fluctuating in between 0.23 and 0.27 μA. The currents under these values are marked in the figure with the dark and light gray region, respectively. The photo-current was observed as described in section 4.4, and the maximum and minimum values (except outliers) were noted. The average of these values are displayed in Figure 4.11 for different configurations. Since the photo-current values were noted manually, no standard deviation can be calculated to state the statistical uncertainty. The observed fluctuation however mostly occurred in the second significant digit. Systematical uncertainties can originate from a series of reasons: The photo-current is dependent on how tight the screws are fastened during the reconfiguration process[9], on how exact and parallel[10] the placement was with respect to the light source (that

[9] The light shield body stayed the same for Ref-AX and Trans-AB. It was then changed for Config-B since earlier one screw broke on PCB-B. Config-C has obviously another light shield body, too.

[10] It was observed for Config-B that an intentionally angled placement lead to a deviation of the most significant digit of the photo-current for both light sources.

was held as consistent as possible), on how stable[11] the intensity of the light source was and un-recorded temperature differences between the measurements. Therefore it is reasonable to assume, that the systematical effects dominate over the statistical fluctuation. They were not precisely quantified, because the interesting result is not the exact values but the overall trend[12].

The measured configurations:

As a reference, the flat interface was re-measured in this more accurately defined illumination setting, both before and after taping the electrical connections on PCB-B, called Ref-A1[13] and Ref-A2, respectively. Afterwards, the edge and M2 tapes on PCB-A were removed and replaced by the push-down frame. The tape on the PCB-B side was left for an intermediate measurement (Trans-AB), to serve as a further reference point, before the same was done on the PCB-B side (Config-B). Since the photo-currents with the framed interface were still clearly higher than the dark current, a new light shield was designed with a the above discussed o-ring interface. In this configuration the current was finally compatible with the dark current in the reference position[14]. By modifying the position of the dark box, however, as a last reasonability check, the current was increased repeatedly above 0.4 μA with both the LED and laboratory light. Since even re-taping the connectors more carefully did not diminish this behavior fully, it is theorized to come from the penetration below the ground plane. This also fits with the observation that it is different for different angles, where the light possibly enters the tolerance gap better.

Outcome: While the behavior of the single configurations could be discussed in detail too, the important result for the ComPol project is the overall trend combined with the knowledge about the light leaks obtained in subsection 4.4.4. The strong reduction of the photo-currents between the un-taped (Ref-A1) and taped (Ref-A2) electrical connectors on the PCB-B, **emphasizes the immense influence of the through-hole connectors**. Logically, it is most drastic for a direct illumination of PCB-B (red). However, the effect is also apparent for the data taken with PCB-A illuminated (blue). Once the electrical connectors on both sides were taped the photo-current of the PCB-B illumination (red) stayed below its respective (dashed/dotted) counterpart with PCB-A illumination (blue), for at least three configurations. For Config-C they are nearly on the same level and the inversion of

[11] The phone was recharged during each reconfiguration phase and lab light measurement (without removing it from its fixed position in the dark box).

[12] Therefore it was also decided to not display a rough estimation of the uncertainties.

[13] Ref-A1 was found to be consistent with the measurement (9) of the previous section.

[14] The position, which was marked in the beginning, was at least for the laboratory light arbitrarily defined.

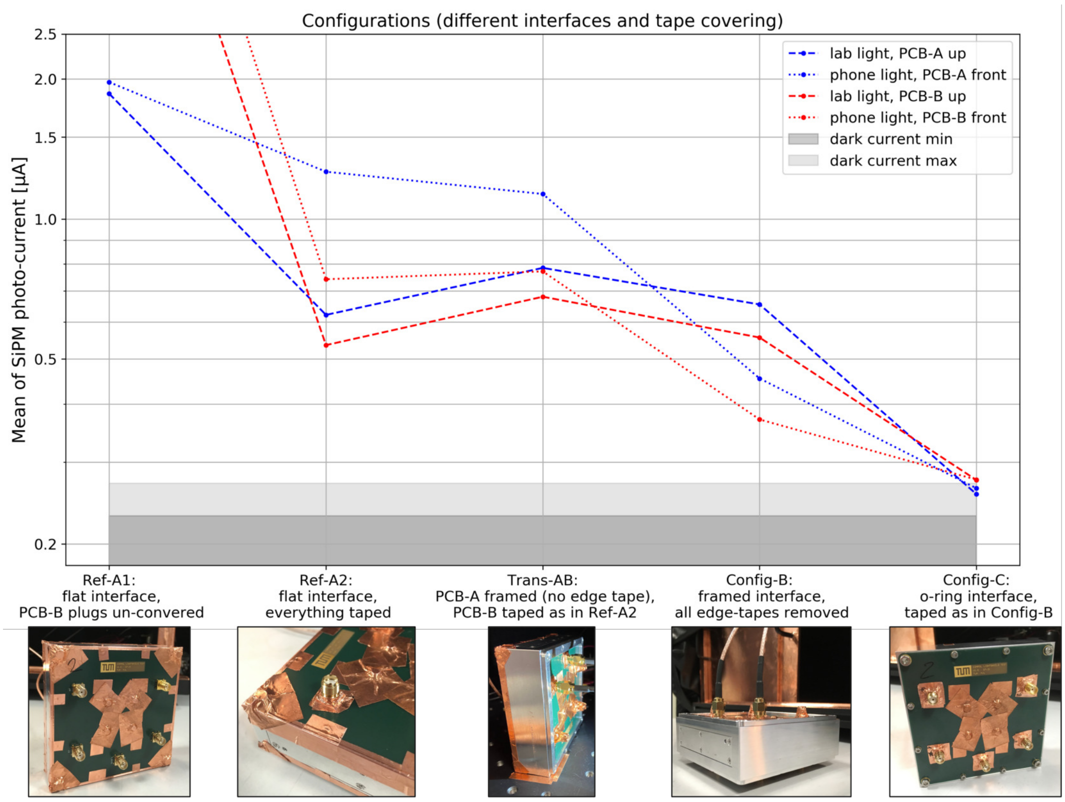

Figure 4.11: *Evolution of the photo-current for the tested interface options in four illumination setups: On the table in the laboratory light (dashed) and in the dark box illuminated by the phone LED (dotted); with each time measuring once with the PCB-A (blue) and one with the PCB-B (red) facing the light. The gray regions mark the typical values of the dark current. The mean of the photo-current is shown on a logarithmic axis to better display the difference between the measurement points.*
The first two configurations are the flat interface without and with the electrical connectors on PCB-B covered. They are taken as reference. Trans-AB an intermediate step having the push-down frame on PCB-A while keeping the taped flat interface on PCB-B. The last two configurations are the fully framed and o-ring interface. The o-ring interface reaches down near the dark current.

the points is small and might have a systematic cause. Since the light-leakage at both sides should be at about[15] the same level for Ref-A2, Config-B, and Config-C, this would suggest that the light leaking at PCB-A might arrive at SiPM-A2 better, than the leakage origination from the PCB-B side. This is contra-intuitive since the

[15] Deviations might be caused by systematic effects, like the screw connections.

light entering at PCB-A must be back-scattered to the inside of PCB-A, while the light entering at PCB-B would fall straight onto the PCB. However, the deviation could equally likely be explained with a tighter taping on the PCB-B. The complete framed interface has the overall trend to reduce the photo-current, but is not able to reach down to the dark current. That is possibly due to a small gap between the frame and the light shield body, that is mechanically enforced as described above. The o-ring configuration is finally able to reduce the photo-current down to the desired level. While doing so, the difference between the different illumination conditions is also reduced - it is light-tight from all directions.

Conclusion: Since the sharp-edged interface has major drawbacks and Config-C, i.e., o-ring interface plus taped connectors and taped middle screws, reaches the regime of the dark current, **the o-ring interface is the best option for ComPol** and the new iteration of light-test PCBs, is designed according to this layout.

4.5 Photo-Electron Spectra of the Best Design and Second PCB Iteration

The o-ring interface was found to reach down to the dark level. In this section, the o-ring interface is examined closer with the measurement of photo-electron spectra under the illumination of a stronger light source, while also adding a temperature sensor. A new iteration of the test PCB was designed and compared with the performance of the first PCB in its final taped state, as shown in subsection 4.4.6. The respective additions to the setup and the need for a temperature measurement, are further described in subsection 4.5.1. Afterwards the approach of the measurement is explained together with the definition of the examined quantities (subsection 4.5.2), before the results of the two PCBs are compared (subsection 4.5.3).

4.5.1 New Setup Components: Photo-electron Readout, Light Source, Temperature Sensor and Test-PCB-V2.0

A couple of changes were made to the measurement setup. Starting with the way the SiPMs are read out, all changes are described including the light source, the introduction of a temperature sensor, and the new iteration of the measurement PCB. Also the impact of temperature on SiPMs is briefly discussed.

SiPM p.e. spectrum readout: As sketched in Figure 4.4, the SiPM signals are first amplified. Afterwards the pulses are digitized by a CAEN DT5730S desktop digitizer and read out with the CoMPASS data acquisition software by CAEN [63]. It is run in the pileup and saturation rejection mode. Pileup rejection means that if two events fall into the same integration gate, they are not acquired, but rejected already at board level. The saturation rejection prevents the acquisition of signals that exceed the dynamic range of the digitizer and are thus clipped. Both rejections and the time that the trigger is frozen (trigger hold-off) before the next trigger is acknowledged, leads to a dead time, where the DAQ is blind to signals. This reduces the real measurement time, called *realtime* t_r, to a shorter effective recording time, called *livetime* t_l.

Improved light source: For the measurements in the dark box, a more sophisticated light source was used. It is a flicker-free LED light intended for the use in physical measurements. The light is emitted in a defined light cone of about 110°, see picture Figure 4.12, and has an uniform angular distribution herein. Compared to the phone LED this lamp has a greatly enhanced intensity of ~260 lm but its low power consumption of ~3.5 W leads only to a slightly heated LED housing [64].

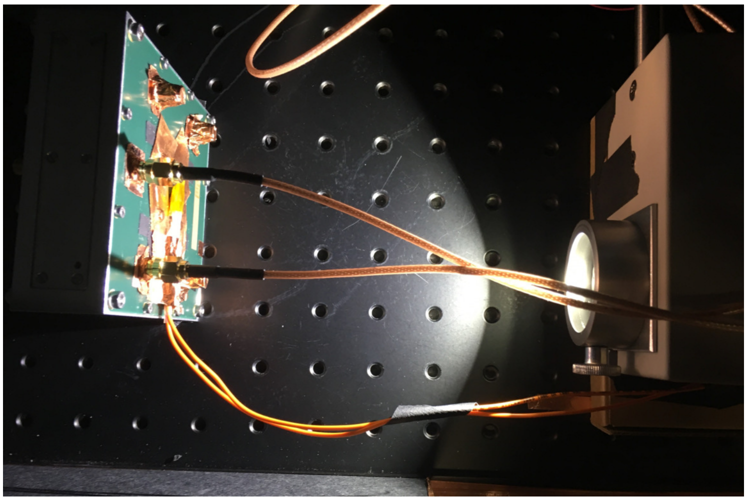

Figure 4.12: *The new LED light positioned in the dark box in front of the light shield setup with the temperature sensor fixed to the center of PCB-A.*

Temperature sensor: So the enhanced illumination, also brings the possibility of increasing the temperature. Even if the alphys-LED does not have a large heating effect, what need to be checked, the planned evaluation with the solar simulator (see section 4.6) will very likely rise the temperature.

SiPMs as all semiconductor detectors are sensitive to temperature changes. Especially the dark current, that originates from thermally produced e^-/h^+-pairs is increased with rising temperatures. The data sheet of the successor SiPM (PM3325-WB-D0 [65]) shows that the dark count rate per active area increases exponentially about one order of magnitude for every increase by 30 K. Since the PM3325-WB-B0 SiPM has a dark rate of 100 kHz/mm^2 at 21°C, the expected dark count rise was back-of-the-envelope approximated to be roughly ≈150 kHz/mm^2 for an increase to 26°C, when assuming a similar same behavior as PM3325-WB-D0.

Temperature changes also influence the overvoltage seen by the SiPM. It increases linearly with temperature, if it is not compensated with a flexible bias voltage [49]. For the used SiPMs, the PM3325-WB-B0 data sheet states a rise by 22.0 mV/K [60]. For the light-tightness measurement, the bias voltage is fixed and therefore a changing temperature will change the overvoltage. With the rise of the dark rate by 20 kHz/mm^2 each +1 V in overvoltage (180 kHz for the used 9 mm^2 SiPMs), as calculated from the PM3325-WB-B0 data sheet, the overvoltage-temperature relation translates this into a small additional rise of ∼20 kHz each 5 K, due to the thermal rise in over-voltage. This is negligible compared to the primary effect.

Even though the heating is stated to be small for the intense LED lamp, the temperature must be monitored. First to ensure that no significant temperature changes remain unnoticed. And second to improve the knowledge about the temperature behavior and this improve the comparability with the subsequent solar simulator measurements. For the temperature monitoring a thermistor was taped to the middle of PCB-A as it can be seen in Figure 4.12. The used sensor is the negative temperature coefficient thermistor GA10K3A1AM of TE connectivity, that has a stated temperature accuracy of ±0.05 K from 32 - 44°C [66]. Since the given range is above the expected measurement range, an uncertainty of ±0.1 K is being assumed at laboratory temperatures. The temperature was read out by hand from an KEITHLEY multimeter system, in the beginning, middle and end of each measurement.

PCB Version 2: The second iteration of the light-tightness test PCBs, included the features found in the leakage study (subsection 4.4.4). The through-hole vias were replaced by blind vias and the through-hole connectors by surface mounted versions. The interface area of the PCB, that is left blank instead of covering it with solder resist, is adjusted to fit the o-ring light shielding interface. The edges were metallized to prevent light entering at the tolerance gap from scattering below the ground plane and thus bypassing the o-ring sealing. Due to production processes, not the complete edges could be metallized, but two small areas on each edge were used to hold the PCB and were therefore not metallized. When looking closely, one can see it in the Figure 4.13 (a) between each M3 and the next M2 screw. One question was, if they influence the light-tightness. Thus they were taped after a first measurement as seen in Figure 4.13 (b).

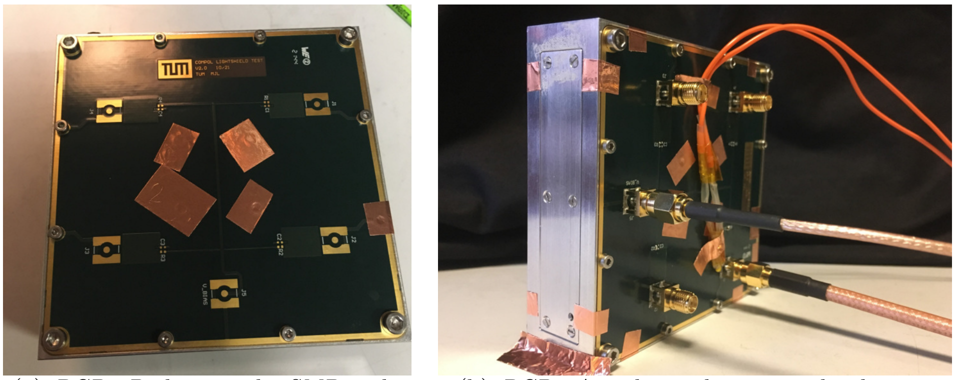

(a) *PCB2-B showing the SMD pads.* (b) *PCB2-A with taped non-metalized parts.*

Figure 4.13: *Second iteration of test PCBs. The metallization of the edges ends on the upper surface. The middle screw holes were all taped before measuring. The M2 screw next to channel B2 broke and the hole was taped to exclude light entering there. The production-conditioned eight non-metallized areas per PCB are sparsely visible in (a). They were left open for the first measurement and then taped as seen in (b).*

4.5.2 Experimental Approach and Definition of Physical Quantities

In the following p.e. spectra are taken first with the old test-PCBs (PCB-V1) as a reference, still assembled and taped like in Config-C in Figure 4.11. Afterwards the new PCB iteration (PCB-V2) was investigated, first with minimal taping (as in Figure 4.13 (a)) and then with additional taping above the small non-metalized parts at the edges (as in Figure 4.13 (b)). In the end, the results for the taped PCB-V1 and PCB-V2 are compared. The SiPMs that are soldered to the different PCBs, are of the same type, but not identical. They are very likely produced from different wavers and therefore will probably show slightly individual responses under the same condition. Therefore, it is important to record dark spectra for both PCBs to analyze the data only relative to their own dark counts.

The SiPMs were biased with $V_{bias} = 32$ V, corresponding to a nominal overvoltage of $V_{OV} = 5.1$ V at 21°C. This time, all measurements were taken in the dark box. The alphys-LED was fixed in the position as shown in Figure 4.12, and turned on/off from outside the dark box without opening the box. This reduces potential systematic uncertainties, since unintentional change to the placement of dark box tightness are prevented. The recorded data consists of the realtime t_r, the livetime t_l, and of the counts per ADC channel C/ADC, where the ADC channel is proportional to the pulse height[16] and thus to the amount of SiPM micro-cells that detected a

[16] More precise: the minimum, since the signal is inverted by the amplifier.

photon. Since the current resulting from each micro-cell is fixed, the SiPM output is quantized. In a perfect detector and readout this would lead to equally spaced delta peaks in the respective ADC channels corresponding to the signal of n micro-cells. In reality, it is a superposition of Gauß distributions, together forming the p.e. spectrum.

The goal is to **compare the SiPM p.e. spectra recorded in dark and illuminated conditions** to identify any light excess. SiPMs and p.e. spectra were introduced here. From the measured p.e. spectra it can already be seen qualitatively, whether there is an excess of counts at higher ADC channels, being the signature of more photons reaching the SiPM simultaneously. However, a quantified statement about the respective light excess will be obtained from the total count rate R, which is calculated from the total counts C^{tot} and the livetime t_l as given by CoMPASS.

$$R^{tot} = \frac{C^{tot}}{t_l} = \frac{\Sigma_{ADC}(C/ADC)}{t_l} \tag{4.3}$$

Then, the total dark rate R_d and total light rate R_l are compared by means of the relative excess rate R^{rel}_{ex} of the light over the dark rate:

$$R^{rel}_{ex} = \frac{R_l - R_d}{R_d} \tag{4.4}$$

The **needed measurement time** per light condition for a reasonable statistical accuracy was extrapolated on basis of previous auxiliary measurements.
These light and dark measurements, 130 s each, revealed that the resulting livetime was $\sim$ 30 s for both dark and light measurements. That is a realtime ratio t_l/t_r of only ~0.2, what was understood to be the intrinsic response of the digitizer to the already high dark count rate of ~1.6 MHz and slightly higher light count rate. The theoretical rate from the data sheet is 900 kHz at 21°C and 5 V overvoltage. In the 2 minutes the temperatures of in light and dark conditions were rising from 22.0°C to 22.3°C, and falling from 22.3°C to 22.1°C, respectively. With the relations introduced in subsection 4.5.1 (temperature sensor part) the +1.3°C added to the applied V_{OV} = 5.1 V result in an increase of the rate by only ~23 kHz and can by far not explain this difference. It is often true, that the data sheets merely give a rough indication and deviations of ±20% might occur. However, +20% could still only explain a rate of about $\sim$ 1.1 MHz. It is likely, that the deadtime is overestimated by CoMPASS, leading to a smaller livetime and overestimated count rate. This would be an one-sided systematic error on the livetime, since the deadtime is calculated the same way for all measurements. While this systematical error would not be negligible for absolute measurements, the objective is the relative comparison between the rates in dark and light conditions. For this the CoMPASS livetime can still be taken. It

must be noted, however, that the absolute rates are likely overestimated and only the relative comparison is meaningful.

The statistical uncertainty on the other hand inherits the Poissonian behavior of counting, namely $\sqrt{counts}$. While the systematical shift of the livetime might be large it is reasonable to assume a small relative statistical $\Delta^{rel}_{stat}(t_l)$ and thus the error propagation for the statistical uncertainty of the total rate simplifies to

$$\Delta_{stat}(R^{tot}) = \frac{\sqrt{C + \Delta^{rel}_{stat}(t_l)^2 C^2}}{t} \approx \frac{\sqrt{C}}{t} \quad \text{for small } \Delta^{rel}_{stat}(t_l). \tag{4.5}$$

To reach below a statistical uncertainty of $\Delta R^{tot} = 0.15$ kHz for a measurement similar to the dark auxiliary measurement, a livetime of $l_t \sim 72$ s is required. That results into a **realtime of at least 6 minutes** for the dark, and more for the light condition (as there higher rates might occur).

Recording these **6+ minutes in a single measurement**, would already mean a temperature **increase of nearly ~1 K for the low-heating alphys-LED and more for the future solar measurements**. From the recorded p.e. spectrum it is not possible to differentiate between the counts collected at different times, and thus different temperatures. To prevent too much warming during a single p.e. spectrum, it was decided to collect the data segmented in shorter recordings and combine them later. Like this, they first can be checked for the impact of the temperature (corrected if necessary) and afterwards be combined to joint a conclusion. While a temperature rise of ~1 K maybe still be acceptable, this approach was also choosen for a similar measurement approach for both LED and solar simulator illumination. From the auxiliary measurements it was seen that the temperature during the dark measurement returns to roughly the original temperature. This was utilized to keep the total temperature rise small by alternating measurements of illuminated and dark condition.

To assess whether measurements of different livetimes are comparable[17], measurements with different realtimes of 60 s (short), 72 s, 130 s (normal), and 300 s (long) were taken. To still have enough data for if they are not compatible, it was decided to **record a minimum of four normal and three short measurements**, resulting in a livetime of $\approx 6 \cdot 30\ s = 3$ minutes. The different lengths naturally result in the according differences in counts. Therefore, the usual p.e. spectra (absolute counts per ADC) diverge. To be able to still compare these spectra graphically, their **individual rates per ADC channel** $(C/ADC)/t_l$ are displayed in an histogram together with one **combined rate spectrum** for each measurement set of the same type (same lighting, same PCB).They are in a sense the average rate per ADC channel of all measurements combined, but instead of averaging over all individual rates, they

[17] This will become important later with the high intensity illumination and resulting higher heating.

were calculated by summing the counts of all nth ADC channels of the individual p.e. spectra an dividing by the summed livetime

$$\bar{R}/ADC = \frac{\Sigma_i(C_i/ADC)}{\Sigma_i(t_{l,i})} \tag{4.6}$$

with i denoting the individual measurements of the respective subset.

4.5.3 Conducted PCB Comparison and Results

First the individual measurement sets are briefly discussed, then they are compared by means of the relative rate excess of the LED measurements compared with the dark measurements. Both the relative rate excess per ADC channel and the integrated value over all channels are investigated.

For PCB-V1 in total nine dark measurement segments were taken: four 130 s, three 60 s, one 72 s and one 300 s long. With an average time ratio of 19% this resulted in a combined livetime of 203 s. The rate spectra of all nine measurement were found to be compatible with each other, no matter the realtime. They are displayed in Figure 4.14 (a) together with the combined rate spectrum (sum of all dark segments as in Equation 4.6) and overlap perfectly. Neither the different recording lengths, nor the small temperature changes from minimal (21.9 ± 0.1)°C to maximal (22.3 ± 0.1)°C lead to a deviation. The total combined dark rate, calculated from integrating the combined rate spectrum over all ADC channels, is (1589.67 ± 0.09) kHz and listed in Table 4.3 together with other values, that provide an overview about all alphys-LED measurements.
For the LED illumination the temperatures stayed in the same range as for the dark measurements only reversing the cooling. That makes them perfectly comparable with the dark measurements, as the contribution from the dark counts to the spectrum will be the same. Also, the individual segments should be equally compatible with each other. The total number of segments was reduced as one long data set and one 130 s data set was lacking. This lead to a total of only six light measurements for the PCB-V1, three of normal and short lengths each. It was not possible to add more recordings later, as PCB-V1 has already been replaced by PCB-V2 and the taping could not have been reproduced identically. Together, the available data sets accounted for a combined livetime of 103 s. The individual and combined rate spectra (Figure 4.14 (b)) were nearly all overlapping perfectly. Only one LED measurement showed a slightly higher rate per ADC Channel, visible in the first 7 peaks of the individual rate spectra, when looking carefully. Integrating this individual spectrum it also resulted in a higher total count rate of (1846.6 ± 0.3) kHz, than for all other segments, which were between $1584 - 1648$ kHz. The respective

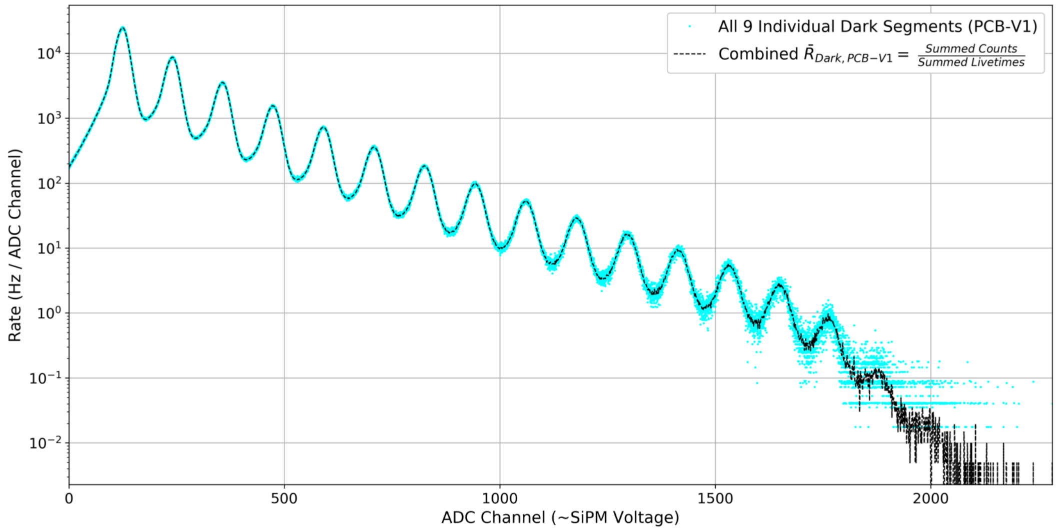

(a) *Rate spectra for all dark measurements with PCB-V1, overlapping perfectly.*

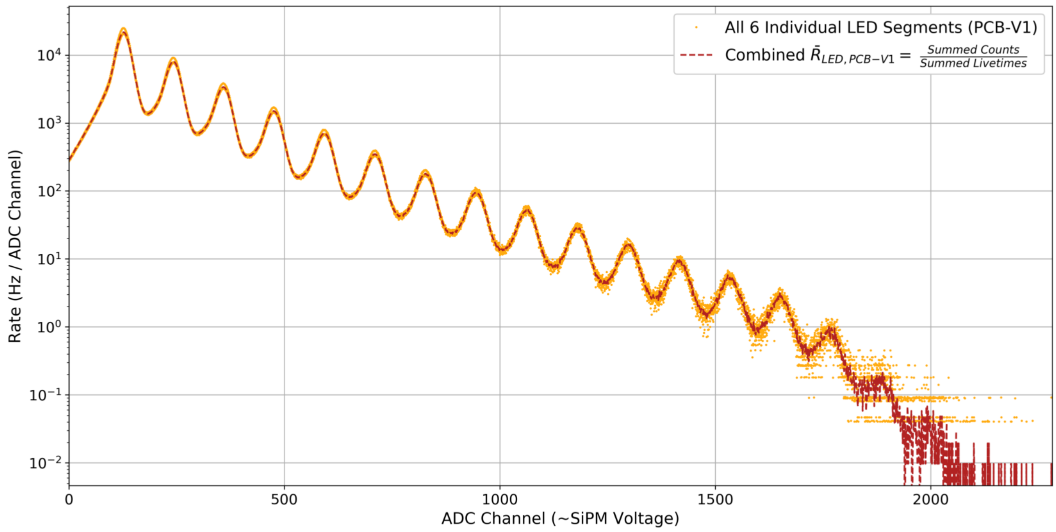

(b) *Rate spectra for all LED measurements with PCB-V1. One segment has a slightly higher count rate, barely visible in the first 7 peaks, which has a negligible impact on the combined rate.*

Figure 4.14: *Rates per ADC channel calculated from the p.e. spectra and the livetime. All individual measurement segments of one configuration are displayed together. Since the small temperature differences have no impact, they are summed up to a combined rate spectrum as defined in Equation 4.6 for each configuration separately.*

measurement was taken at one of the lowest temperature ranges recorded with the

Setup	Number of Segments	$\Sigma_i(t_{l,i})$	$\bar{R}^{tot}_{all}$ (kHz)	R^{tot}_i min-max (kHz)	T min-max (± 0.1°C)
PCB-V1 Dark	4x 130 s, 3x 60 s, 1x 72 s, 1x 300 s	203 s	1589.67 ± 0.09	$1533 - 1636$	$21.9 - 22.3$
PCB-V1 LED	3x 130 s, 3x 60 s	103 s	1662.93 ± 0.13	$1584 - 1847$	$21.9 - 22.3$
$R^{rel}_{ex}(V1)$			$(4.61 \pm 0.01)\%$		
PCB-V2 Dark	4x 130 s, 3x 60 s	131 s	1717.58 ± 0.11	$1523 - 1869$	$23.4 - 23.6$
PCB-V2 LED	4x 130 s, 4x 60 s, 1x 167 s	169 s	1753.26 ± 0.10	$1642 - 1965$	$23.4 - 23.7$
$R^{rel}_{ex}(V2)$			$(2.08 \pm 0.01)\%$		
V2 (taped) Dark	4x 130 s, 3x 60 s	127 s	1771.26 ± 0.12	$1573 - 1881$	$23.7 - 24.2$
V2 (taped) LED	4x 130 s, 3x 60 s	124 s	1795.01 ± 0.12	$1703 - 1984$	$23.7 - 24.0$
$R^{rel}_{ex}(V2t)$			$(1.33 \pm 0.01)\%$		

Table 4.3: *Overview of the p.e. measurements comparing PCB-V1 and PCB-V2. The light source is a 260 lm bright alphys-LED (Figure 4.12). The label 'taped' refers to the production-conditioned small non-metallized parts at the PCB-V2 edges (Figure 4.13). The table lists the amount of data sets of a respective realtime t_r length, the summed livetime (usually $\sim 0.2t_r$), the total count rate of all segments combined $\bar{R}^{tot}_{all}$, the range of the total rates R^{tot} of the individual segments as additional comparison, and the temperature range of all segments of the respective setup.*

alphys-LED (21.9 ± 0.1°C - 22.1 ± 0.1°C), so the temperature is not the reason. It was however found that, compared to all other PCB-V1 measurement segments (both dark and light) having a time ratio between 18 and 19%, it showed a slightly smaller time ratio of ~16%. This is most likely the reason. Since the deviation was however small, it was nevertheless included in the combined spectrum maintaining a (already small) total livetime of 103 s. Integrating the combined rate spectrum lead to a total rate of 1662.93 ± 0.13 kHz.

For PCB-V2 the measurements of the p.e. spectra were repeated before and after the non-metallized parts of the edges were taped. A separate set of dark recordings were acquired for the taped version. For once this allowed to still alternate between light and dark, with the dark condition as intermediate cooling phase capable of holding the setup at nearly the same temperature. Also, it added the advantage that the setup stood still between the taped LED and the dark taped measurements.

For the minimally taped PCB-V2 (non-metallized edge parts open), the standard[18] amount of seven segments were recorded in the dark, giving 131 s of data. For the LED illumination, an additional short and one long measurement were taken, enhancing the total livetime of this configuration to 169 s, recording long enough for a statistical uncertainty of only 102 Hz.
After taping the non-metallized edge parts, the standard seven segments were recorded for both dark and illuminated conditions. This resulted in 127 s and 124 s of data, respectively. Interestingly, both the dark and light rates of the taped setup were found to be higher in absolute numbers then the minimally taped PCB-V2. The livetime to realtime ratios were overall compatible for before and after taping. Instead it could be caused by the $\approx 0.5°$C increase in temperature. Therefore it is important to compare the LED measurements only with the dark measurements of the same setup.

The compatibility of the individual recordings was verified via the rate spectra. All data points for a single setup were found to form one indistinguishable spectral line, similar to the dark rate spectra in Figure 4.14 (a), just marginally broader, reflecting the greater minimal-maximal span of individual count rates that is stated in Table 4.3. Being of good compatibility they were all summed in the respective combined rate spectra. Instead of displaying all individual rate spectra as for PCB-V1, the combined rate spectra are directly shown in the comparison plot Figure 4.15 with all combined rate spectra together. The upper two panels show the absolute combined rate spectra $\bar{R}_{lighting,configuration}$ for each PCB-V1 (top) and PCB-V2 (middle) configuration. The lower panel displays the relative excess rate (Equation 4.4) of the combined light rate $\bar{R}_{LED,config}$ over the combined dark rate of the same configuration $\bar{R}_{Dark,config}$.

The light and dark measurements for PCB-V1, show a clear deviation already in the absolute combined rate spectra, even though it was still taped as in Config-C of Figure 4.11. For the PCB-V2, all combined rate spectra match up very well, leaving aside the noise part before the first p.e. peak. Neither PCB-V1 nor PCB-V2 showed a prominent excess at higher ADC channels compared to the dark. They tail off exactly like the dark rate spectra. Comparing both PCBs, one can see that the peak positions are slightly shifted for the new SiPMs on PCB-V2.

The deviation of the PCB-V2 light measurements from the dark is only visible in

[18] As inferred in subsection 4.5.2 from the approximated statistical uncertainty.

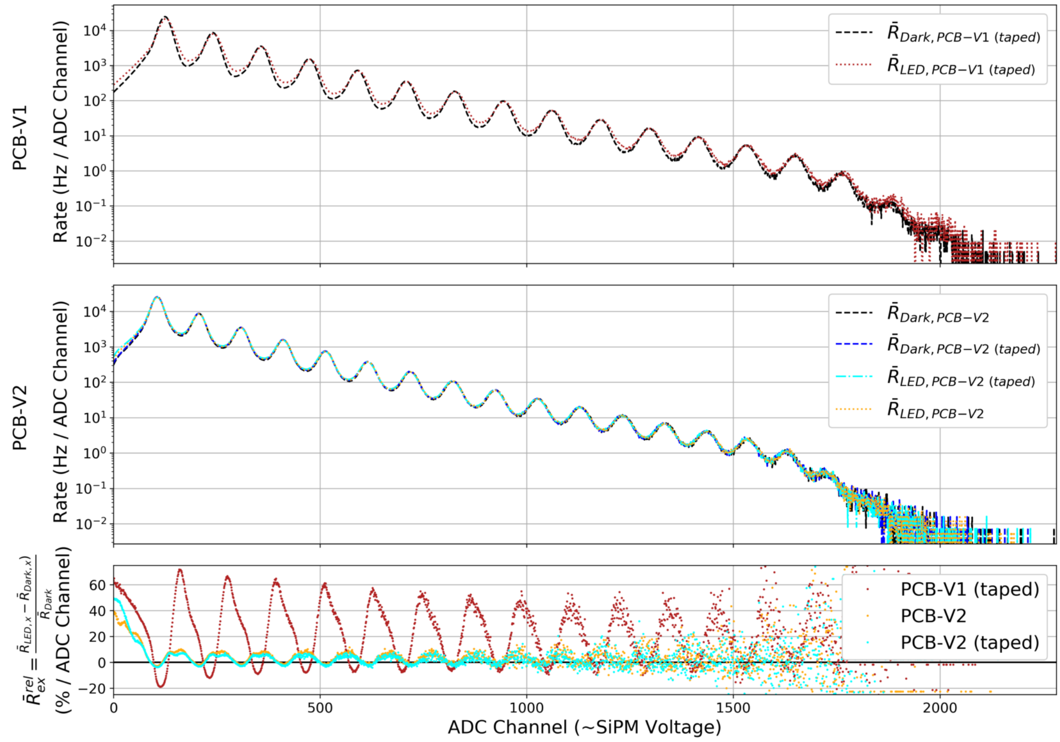

Figure 4.15: *Comparison of both PCBs. In the first two plots, the combined rates of all measurements for the same configuration (light, PCB) are displayed for PCB-V1 and PCB-V2, respectively. The last plot shows the relative excess rates (defined in Equation 4.4) of the LED measurements when compared to their respective dark rates. It is negative at the peaks, which are shifted between the two PCBs, and has a maximum in between. PCB-V2 is clearly better compared to the PCB-V1. The taping of the 16 non-metallized parts of the edges (see Figure 4.13 (b)) reduces the light excess slightly but is comparable with the (minimally taped) PCB-V2.*

the relative excess rate. All three $\bar{R}^{rel}_{ex}$ spectra reach a minimum at the ADC channels of the p.e. peaks and a maximum in between. The absolute rate in the p.e. peaks is even higher for the dark condition, turning the excess rate negative. The total measured counts are however larger. Together with the equally spaced peaks and the same about of peaks as in the dark condition, this means that also in each p.e. peak the number of counts get larger. The Gauss peaks under illumination become wider, resulting in a larger light excess per ADC channels for the region between the peaks.

For PCB-V1 the maximal light excess per ADC channel clearly overshoots 60% and the integrating over the full light excess spectrum yields $(4.61 \pm 0.01)\%$. PCB-V2 is a clear improvement compared to PCB-V1. Without taping it already reaches a more than halved relative light excess of $(2.08 \pm 0.01)\%$. After taping yet another small improvement can be seen both graphically and from the integrated relative light excess of $(1.33 \pm 0.01)\%$.

While the taped PCB-V1 reached the upper edges of the dark regime, it is however apparent from the clear improvement of PCB-V2, that the taping of PCB-V1 could not prevent the entrance of the light fully. The very good result of the PCB-V2 clearly confirms that the sources of light leakage that were found in subsection 4.4.4 were well enough suppressed for the applied illumination strength of the alphys-LED.

4.6 Evaluation with Solar Simulator

A solar simulator lamp was borrowed from the Institute of Astronautics (TUM) to verify the light-tightness of the best setup of the light shield (o-ring interface and improved PCB with taped non-metallized parts as in Figure 4.13 (b)) in a high luminosity environment similar to the expected condition for direct solar illumination or a high fraction of the light being reflected from the ISS surfaces. The lamp is introduced in subsection 4.6.1.

Moving from the single alphys-LED to the solar simulator lamp the light received by the SiPM increased drastically. This was immediately visible by a vast rise of the photo-current from the dark level below 1 μA to maximally 60 μA and was afterwards confirmed by the p.e. spectra. As it was clear that the light shield configuration that was found to be light-tight for the illumination level of the alphys-LED, was apparently not able to sufficiently shield neither the full nor the reduced intensity of the solar simulator, that accounted to $\sim$42% and $\sim$34% of the solar intensity in setup introduced in subsection 4.6.2. Subsequently the initially planned verification evolved into an evaluation of the light leakage under these extreme conditions. subsection 4.6.3 describes the results of this worst case leakage study, questioning the light-tightness of all critical parts of the light shield:

- Does the meander stay light-tight under extreme illumination?
- Does the strong light leak come from the edges of the PCB or the PCB itself?
- Can a close to dark performance be re-obtained? If so, how?

4.6.1 The Solar Simulator Lamp of the Astronautics Institute

The used solar simulator lamp of the Institute of Astronautics (TUM) is shown in Figure 4.16. It was specifically build to mimic the solar spectrum and while reaching the highest possible fraction of the solar intensity, while maintaining a preferable homogeneous illumination [67]. It consists of a LED-array of 120 *Golden Dragon LW W5SM white* LEDs and 12 *DECOSTAR 51 ECO (ES 48865FL)* Halogen lamps, both being commercial parts from OSRAM. The solar simulator is measured in [67] to reach an intensity of $I^{LED}_{80\text{ cm}} \sim 358$ W/m^2 and $I^{LED+HAL}_{80\text{ cm}} \sim 437$ W/m^2 for the LED-array alone and LEDs and halogen lamps combined, respectively. For the full illumination, this is about 32% of the average sunlight intensity of 1370 W/m^2 in space.

Figure 4.16: *Pictures of the solar simulator lamp of the Astronautics Institute. On the left the whole setup can be seen together with its bias box. The footage on the right shows the lamp at work with both the outer ring of 12 halogen lamps and the inner core of 120 LEDs illuminating the light shield setup placed parallel and concentric with respect to the lamp's center. Below, a detailed photo of the LED array shows parts of the cabling for the separate control of each LED row for the most homogeneous intensity distribution possible.*

4.6.2 Setup and Experimental Approach of the High Intensity Light Leak Study

Due to the size of the solar simulator and since the laboratory light is negligible compared to the illumination conditions produced by the solar simulator, the measurements were conducted outside the dark box. The light shielding was placed on the table concentric with the center of the solar simulator and at a distance of 70 cm. Since the intensities were measured in [67] for 80 cm, the intensity with the slightly reduced distance was enhanced to $I^{LED}_{70\text{ cm}} \sim 468$ W/m^2 and $I^{LED+HAL}_{70\text{ cm}} \sim 571$ W/m^2 for the LED-array and the full (LEDs and halogen) illumination of the solar simulator. With an average of 1370 W/m^2 for the solar intensity in space, this accounts to 38% and 42% of the expected solar radiation, respectively.

After the initial photo-current observation that reveled the current light shield configuration to be far away from light-tight at this light intensities, a light leakage study was conducted by taping specific areas with copper tape (analogous to subsection 4.4.4). Since the lamp was only available for a limited time-span, this time the preceding photo-current test was skipped despite the large leak and the p.e. spectra were recorded directly, accepting much larger dead-times due to the enhanced count rate.

The photo-current, however, was still used as rough[19] guide to figure out problematic areas, using the advantage of the immediate response. Also, before the start of the p.e. spectra recording, a quick first photo-current test was used to investigate, which orientation resulted in the largest light leak. With the open meander facing the lamp and the PCBs being perpendicular to the light source and thus less illuminated, the resulting maximal photo-current was 26 μA. With the PCBs parallel to the light source, it was enhanced to maximally 55 and 60 μA for PCB-A and PCB-B (not-biased side) facing the solar simulator, respectively. This already clearly shows that the PCBs contribute more to the leak than the meander. To conduct a worst case study, the following measurements of the p.e. spectra were conducted with PCB-B facing the light. Additionally, that helped to reduce the heating of the biased SiPMs, since their PCB was not directly illuminated and thus in total warmed up more slowly.

The p.e. spectra were recorded with the same setup as described in subsection 4.5.1 and the approach was directly analogous to 4.5.2. The segmented recording of the data with an alternation between light and dark measurement was used again: Intermediate recordings in the laboratory light replaced the function of the dark measurements to provide intermediate cooling and a comparison reference in the same unaltered position. Only this time, shorter recording segments of a realtime of

[19] Other than for the dedicated photo-current measurement, the fluctuations were not observed for a time-span.

30 s were chosen to keep the temperature difference occurring within one recording mostly below 0.4°C. If aiming the same amount of livetime as for the p.e. analysis in section 4.5, this would have resulted in more than 20 segments of each type not even taking into account the expected reduction of the livetime to realtime ratio yet. Due to limited availability, it was therefore decided to adopt a smaller total realtime with resulting higher statistical uncertainties on the measured rates. This however allowed to measure all taping configurations not only with the full power of the solar simulator but also with the LED core only[20]. So for each taping configuration and all three light condition about 7 segments were taken.

The taping configurations were:

- Minimally Taped PCB, what was the most light-tight result of subsection 4.5.3. The tape covered the non-metallized parts of the edges as well as the middle screw holes as seen in Figure 4.13 (b).
- Taping of all blind vias, as temporarily covering showed to reduce the photocurrent.
- All edges of the PCB were taped, similar to subsection 4.4.4, but this time with leaving the M2 screws in place.
- The meander opening
- As a final step the full PCB face was covered with a ≈90 x 90 m^2 sized sheet to copper tape

4.6.3 Temperature Impact and Analysis of the Light Rate Excess

The analysis was following the same approach as described in subsection 4.5.2, but this time the temperature rise was not negligible anymore, what altered slightly the approach taken.

Temperature Considerations

Despite additional short breaks between the recordings, not enough intermediate cooling was accumulated so that the overall temperature steadily drifted upwards. In total it spanned from 21.4 to 25.6°C. From the measurement of the first segment of each taping configuration to the last, the gradual heating within that one configuration accounted to about 3-4°C.

Thus, it was not reasonable anymore to combine all measurements of one configuration (lighting, taping). This was also apparent from the broadening of the

[20] This proved to be very important for the analysis of the recorded data.

fluctuation of the individual p.e. rate spectra as it can be seen in all figures of this section. Instead of averaging over all recordings of equal configurations, they were treated one by one. To keep the temperature impact as low as possible, the solar measurements were matched with the individual recording of the laboratory light that had the closest maximal temperature.

Since the notable rise in the detected rates between the taped and untaped dark measurements, as observed in subsection 4.5.3, might be accounted to the temperature increase of about $\sim$0.6°C (see Table 4.3). Therefore, all recordings under solar illumination that showed an absolute temperature difference of more than 0.6°C, either within the single measurement or between the maximal temperature of the closest laboratory light measurement, were excluded[21] from the analysis since they had no viable comparison basis.

The Laboratory Light Measurements

The recordings at the ambient laboratory light are taken as approximation to the dark condition. In Figure 4.17 the rate spectra of two of the taping configurations are shown compared to the average dark rate obtained for the best light shield setup of subsection 4.5.3. It shows that the light was not only negligible compared to solar simulator intensity, but that it generally was also in the same order of magnitude as the dark measurement. The visible shift in the peak locations corresponds to a shift in gain (photo-current per fired micro-cell), which is rising with the temperature as the location of the n-th peak is proportional to n times the current of one fired micro-cell.

From the figure it can also be clearly seen that the rate spectra for the different taping configurations were deviating. Since it is only an approximated, not a real dark measurement, this could be because of two explanations: it could come from slightly different positioning and thus different lab light illumination or from the temperature differences between the taping configurations. Since the differences of temperature within[22] one taping configuration are even larger than the rise between the configurations, most likely the position is the actual reason here. Therefore it was important to compare the LED measurement only with the dark rates of the same setup, even though both were dark measurements. Not respecting this would have resulted in a corrupted relative light excess.

[21] In total four solar recordings were excluded because they showed between 0.7 and 1.6°C difference to the next comparison measurement.

[22] The temperature rise within the configuration however lead to the apparent higher fluctuation of the rates in one configuration, visible by the broadening of the values depicted in one color.

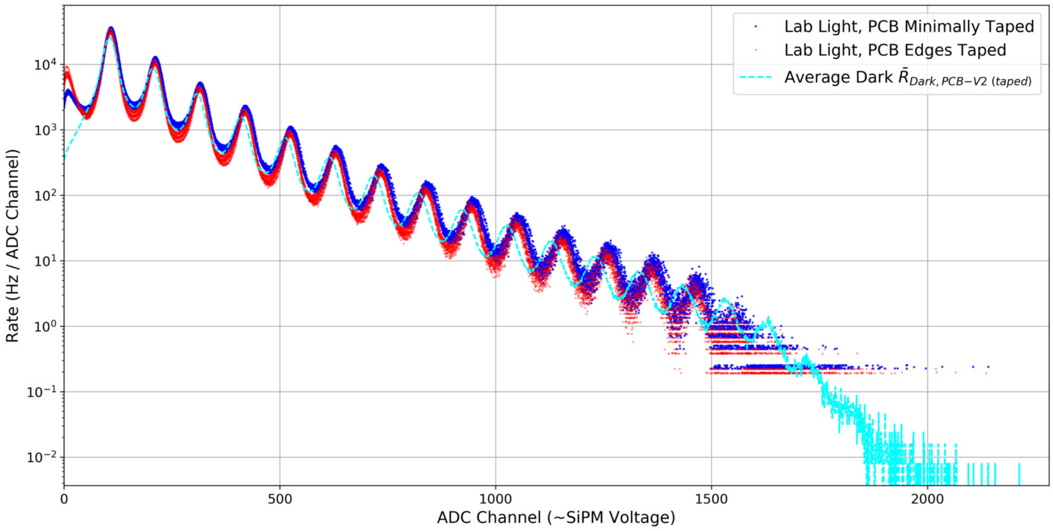

Figure 4.17: *Rate spectra of p.e. measurements under laboratory light illumination. Here, all measurements of two exemplary taping configurations are shown in comparison with the averaged dark rate of subsection 4.5.3. The other configurations lie between the two curves and are not shown for clarity. It shows the rate deviation between the configurations, the broadening of the distribution within one configuration, compared to the ones in Figure 4.14, and the overall compatibility with the level of the average dark rate spectrum.*

The Solar Measurements

Under the illumination with the solar simulator very high rates were accumulated. The rate spectra of all recorded measurements under illumination with the solar simulator are shown in Figure 4.18, separately for the LED-core and full illumination. The colors hereby denote the respective taping configuration. Looking at the p.e. rate spectra, it can be seen that particularly high rates led to a significant washout of the otherwise distinct photon-peaks. This effect was interpreted to come from the CEAN digitizer that could not process the high rate of signals anymore, missing or clipping a large amount of events. This assumption is reinforced by the drastically reduction of the livetime to realtime ratio to about 1-5% for all curves showing the washout, while it was already an incredibly low 10-12% for the other not washed-out curves. This effect was found to be predominantly present in all the data taken under the full (LED Core + Halogen) solar illumination. The recordings from the illumination with the LED-core only showed this effect in the minimally taped configuration.

The halogen lamps contribute 12% to the total intensity of $I_{80 \text{ cm}} = 437 \text{ W/mm}^2$

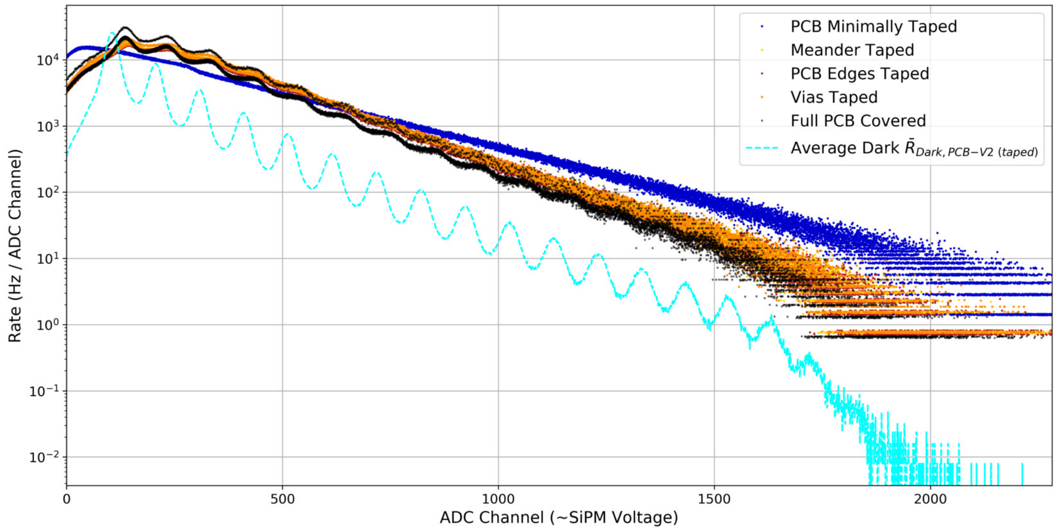

(a) *Rate spectra for all measurements under the full illumination of the solar simulator lamp.*

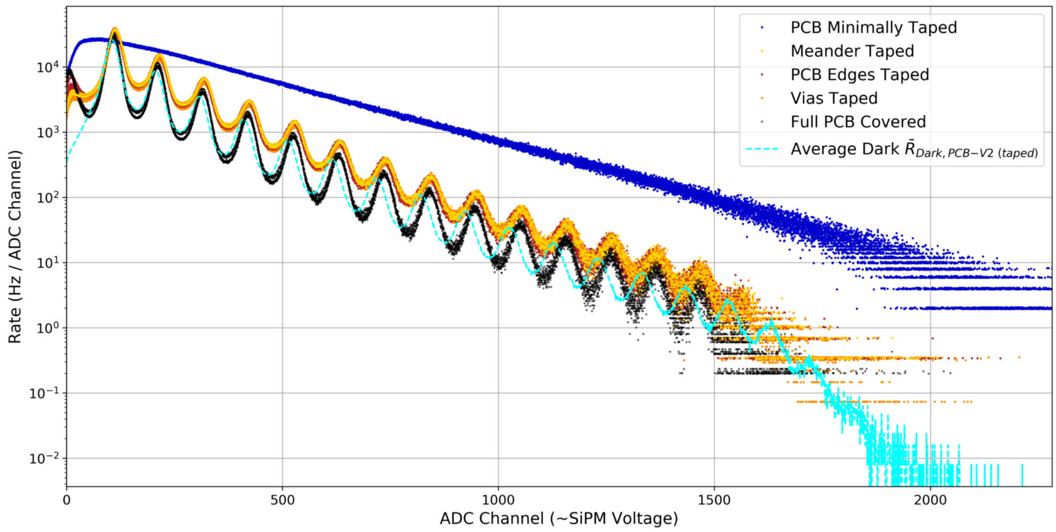

(b) *Rate spectra for all measurements, using only the LED-array of the solar simulator.*

Figure 4.18: *All individual rate spectra taken under illumination with the solar lamp with (a) the LEDs and halogen lamps, and (b) only the LED-array turned on. The colors denote the different tapings. For better comparison the averaged dark spectrum for the minimally taped PCB-V2 from subsection 4.5.3 was added. The wash-out of the p.e. peaks is present throughout all recordings in (a) and for the minimally taped recording of (b).*

reached by the solar simulator. Furthermore the LED core not only dominates the total intensity with its $I_{80\ \mathrm{cm}} = 358\ \mathrm{W/mm^2}$, but is even more dominant in the visual part, as the halogen lamps are specifically added to the solar simulator to approximate the solar spectrum in the infrared [67]. Though the halogen's contribution to the heating suggests that the observed wash-out is due to the temperature, this is not the case since the (taped) measurements with the LED-array at the same temperature do not show this behavior. With the minimally taped LED-array measurement also showing it, it is clear that the sheer strength of the illumination indeed leads to the above proposed struggle of the CAEN with enormous count rate. The resulting strong corruption of the data is confirmed by the following example: The rates calculated from the full illumination with taping of the vias was significantly larger for every single segment as for the minimally taped configuration, even-though the photo-current and LED-core measurements confirm the contrary. Due to the apparent strong alteration and unaccountable enhancement of the undetected portion of the real light excess rates for all full illumination measurements, only the recordings with the LED Core alone were taken into account for the further analysis. For the minimally taped configuration, the resulting light excess will be only a lower bound. When talking about solar illumination in the following, always the array of the 120 LEDs is meant.

Resulting Relative Light Rate Excess per Configuration

The relative light rate excess, calculated as Equation 4.4 for every selected pair of solar LED-array and Laboratory light recordings are shown in Figure 4.19 together with the average value for each taping configuration. A step-wise reduction from a light excess of more than 3 times the laboratory light to about 5% was measured. In the list below the averaged values are discussed together with the interpretation of the findings and conclusion for every configurations.

- **Minimally Taped PCB:** Since the rate was so high that the peaks of the p.e. spectra were washed out (see Figure 4.18) the resulting high excess of $(310.61 \pm 0.1)\%$ is most likely an underestimated value due to event losses in the digitizer.
- **The blind vias:** Taping the blind vias reduced the light leakage to an average of $(66.12 \pm 0.03)\%$. This is a reduction of at least $\sim$79% of the original light leakage, since there only lower limit could be measured. Most likely the light is entering in the small separation between the ground plane and the signal-carrying via track, that can be seen in Figure 4.3. It is therefore crucial to not leave them without light shielding means.
- **The vias and the meander:** A slightly higher average value of $(74.37 \pm 0.03)\%$ was obtained after additionally covering the meander. Since the vias

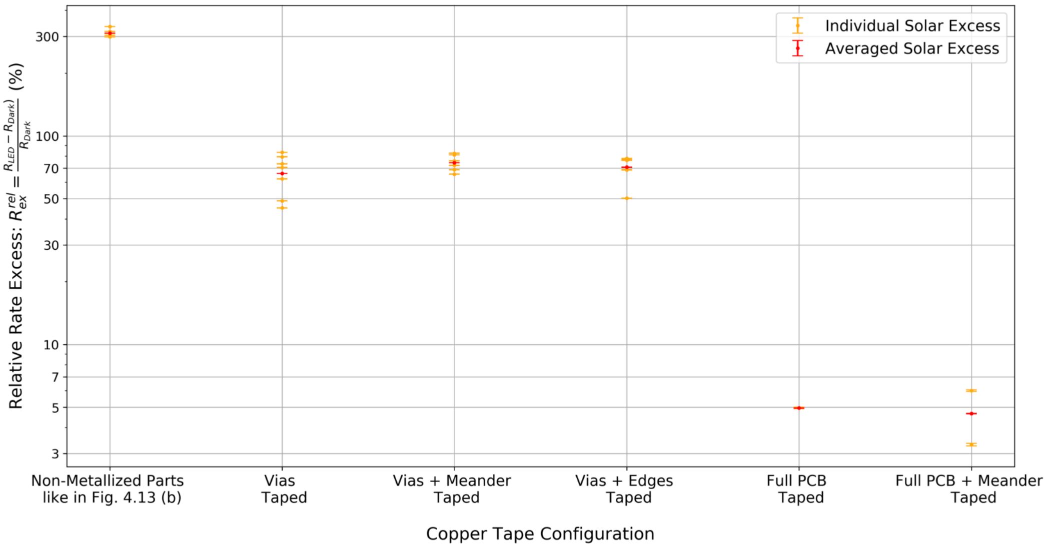

Figure 4.19: *The relative excess of the rates measured by the shielded SiPMs under illumination with the LED array of the solar simulator lamp compared to the ambient laboratory light are displayed in % on a logarithmic scale. For each taping configuration both the individual and the average results are shown.*

are still covered, the true value must lie equal or lower than the vias alone. The small rise can therefore not be significant even if the statistical uncertainty obtained by the error propagation of the Poissonian count uncertainty is smaller than the change. All individual measurements are compatible with the results of the via alone. Since the meander result is of great importance an additional series of p.e. measurements, not further discussed here, taken with the taped and untaped meander facing the solar lamp. This equally did not show a notable reduction of the count rate at a closed meander. Taken together, all measurements **confirm that the meander is indeed light tight even at highest illumination.**

- **The vias and PCB edges:** For the resulting average of $(70.79 \pm 0.03)\%$ the same argumentation as for the meander result is true. It is in the same range as the individual measurements with the vias only. Therefore it can be concluded, that **the combination of the metallized edges and the o-ring interface is light-tight.**

- **Full PCB taped:** Only by covering the full PCB it was possible to further reduced the leakage to $(4.96 \pm 0.01)\%$. The major part of the remaining leakage thus stems from the PCB itself. An additional test with covering of the meander resulted in an average light rate excess of $(4.66 \pm 0.01)\%$ and showed that the meander is not the origin of the remaining $\sim$5% of the light excess.

4.7 Summary and Conclusions for the Shielding Concept

The first part of this chapter discussed the design details of the light shield. The combination of the competing requirements to be light but not gas tight was solved with a venting meander. The other critical design questions were the design of the interface between the light shield and the PCBs as well as the light tightness of the PCBs themselves. In the second part of the chapter, the three-stage test measurements are described, that were conducted to evaluate, improve and re-evaluate its light-tightness of multiple configurations. The following list summarizes the conducted measurements and gives an overview about the answers to the design questions, plus additional findings.

1. Manual measurement of the immediate photo-current change for multiple configurations illuminated with an LED of rather low brightness and the diffuse laboratory light:
   - The meander itself was found to be light-tight under this illumination, anodization is not needed.
   - The edges between the light shield and the PCBs was found to be the major light-leakage source. To close this leak the interface was iteratively re-designed.
   - The O-ring interface reduced the photo-current to a level close to the dark current.
   - The screws in the PCB surface were not light-tight. They should be avoided where possible. If inevitable they need to be covered with black epoxy.
   - The through hole connectors were not light tight. For the readout PCBs SMD connectors must be used.
2. Photo electron spectrum acquisition for the O-ring design and two PCB versions illuminated with a 260 lm bright LED by alphys:
   - The revised PCB iteration included metallized edges with a footprint matching the O-ring interface, surface mounted connectors and blind vias.
   - The new PCB was found to have an improved light-tightness compared to the (taped) PCB-V1 and thereby verified the notable influence of the above stated areas.

- The relative light excess of the new PCB was reduced to a very low level of $(1.33 \pm 0.01)\%$ for a setup with covered small non-metallized areas.

3. Evaluation of the O-ring design and the second PCB iteration in a very high luminosity environment created by an array of the 120 LEDs of the solar simulator, creating an intensity of about $I^{LED}_{70\ \mathrm{cm}} \sim 468\ \mathrm{W/m^2}$:
   - In the best configuration from before, an extreme light leakage was visible in both the steep photo-current increase and an light excess rate in the p.e. spectrum of about 311% above the laboratory light condition
   - The buried vias in the PCB-V2 were found to be the major cause and accounted of about 79% of the initial leakage. For ComPol-ISS either all vias must be covered (e.g., with black epoxy as for the screws) or the previous stages of the light shielding concept must reduce the illumination level enough to eliminate the impact.
   - The remaining light excess of ... was not notably reduced neither by covering the meander nor the PCB edges with copper tape. Both are light-tight.
   - Only covering the full PCB face reduced the light excess down to $(4.66 \pm 0.01)\%$ above the laboratory light condition.

The light shield alone can not shield the full expected solar radiation, even in it's best configuration. It therefore can not be the only component of the light shielding concept but the in subsection 3.5.1 mentioned option of the onion approach must be necessarily implemented.

The 1U-casing needs to shield as much of the incident light as possible. The meander approach is light tight even for direct illumination with 34% of the solar intensity, so that it is also a viable solution for the light-tight venting of the outer directly illuminated 1U-casing as briefly mentioned in section 4.1. The major portion of the light will enter through the window of the 1U-casing even though the metallized foil (selected here subsection 3.5.2) it will reflect a major part of the visual light. Since it will directly radiate onto the SDD-PCB, it must be tested if the remaining percentage of light can penetrate through the buried vias. In that case, the vias would need to be additionally sealed against light anyway and it might be an option to use through-hole vias plus an external covering. Depending on the tightness of the then used sealing option this could be equally good. However, if no additional covering is used or if it is not necessary because a reduced (less direct) illumination is expected due to the mechanical layout (as for the $CeBr_3$-PCB) and therefore the effort of additional covering would outweigh the benefit, the use of buried vias is recommended. Only the testing of the full light shielding concept will however show if the added shielding stages are sufficient or if an additional thin shielding by, e.g., a thin aluminum plate with a cutout of the window size might be needed to stop most of the light coming from the window from arriving on PCB.

Chapter 5

Summary and Outlook

This thesis was dedicated to the preparation of the in-orbit-verification mission ComPol-ISS, that will serve as crucial test platform for the future ComPol instrument. ComPol is a planned, scientific CubeSat mission with a Compton polarimeter aiming to determine the polarization of the black-hole binary Cygnus-X1 between 20 and 300 keV. For the preceding IOV mission a completely new mechanical setup was designed in the course of this thesis. ComPol-ISS will be launched to the International Space Station (ISS). It will be mounted there on an external platform, being the first real-life demonstration of the detector system in space environment. The detector system is a Compton camera, consisting of Silicon Drift Detectors (SDDs) and a $CeBr_3$ calorimeter crystal read out by an array of SiPMs. Though the instrument will be turned off when the sun is in the field of view, the portion of sunlight reflected from the ISS surfaces will be present whenever the ISS is on the day-side of it's orbit. With the SDD and especially the SiPM detectors being highly sensitive to optical photons, they must be shielded as good as possible against visual light. Therefore a dedicated shielding strategy against the expected high illumination was the main focus hereby.

For the CAD model, the major objective was to design the layout of the first combined prototype version of ComPol, accommodating the preliminary detector prototypes of the individual collaborating groups, while making everything fit in the targeted volume of one CubeSat-Unit (1U). Relevant information was gathered from the different groups and continuously updated to the latest status. On this basis, various design options for specific sub-components were thoroughly thought through, resulting in design-changing decisions: The subsystem PCBs of the instrument were defined to a common size of 90 x 90 mm^2. The electrical connections of the subsystem PCBs of the instrument were decided to be connected via 90° connectors and a common backplane PCB. The distance of the SDDs and the $CeBr_3$ were chosen to be 6.1 mm. From this the distance of the SDD-PCB and $CeBr_3$-PCB results in 25 mm. This gap is spanned by the light shield, an aluminum frame, forming the central part of the light shielding strategy. The complete setup is covered with an 1U-sized aluminum case with a window cutout. This cutout was limited to the size of the projection of the SDD detector, reducing the field of view but also reducing the background influence, especially from solar radiation.

The light shielding concept is a multi-staged shielding that is reducing the light step-wise. The outer layer is a metalized PET foil, selected on basis of fabrication availability, light shielding strength, dust protection properties, and permeability for X-rays. The innermost stage is the packaging of the SiPMs that will be crafted by the team from the CEA, providing the $CeBr_3$ crystal. The main stage is the light shield that was designed and evaluated in this thesis. The challenge was to make it light-tight while space-safety requirements prohibit gas-tight volumes. The solution was a meandering venting hole in one side that was found to be light tight even at the illumination with 34% of the solar illumination. The critical parts of the light shield were identified and improved in an iterative loop of light-tightness tests and re-designing. The most critical parts of the initial design were: the edges of the PCB, showing the strongest contribution of 36 - 67% of the initial leakage, followed by the electrical through-hole connectors with about 14 - 32%. Both issues were addressed by an updated PCB. The final configuration of the light shield was comprised of the aluminum frame with a groove for an o-ring sealing and PCBs with metalized edges, surface mounted connectors and buried vias. At the testing under 34% of the solar intensity the o-ring sealing and PCB edges were confirmed to be light tight. The PCB itself and mainly the buried vias however were not tight at this illumination but resulted in a strong leak to three times the strength of the laboratory light used as reference measurement. It could only be reduced by covering the whole PCB face.

With the evaluated first stacking model, that made the dimensions of all previously differently scaled prototype compliant with each other and proofs it to fit into the desired volume of 1U and the development of a multi-staged shielding strategy for optical photons, the fundamental steps towards the mechanical ComPol-ISS setup are accomplished. However, until a flight-ready design among others the following future steps should be addressed:

- Completing the recently commenced transformation of the stacked model into the slide-in model as explained in (page 46) and additional small adaptations of the CAD design as summarized in section 3.6.
- Test of the light shielding strength of the full onion approach. Answer, if it reduces the illumination level enough or if further prevention measures must be taken (e.g., vias with epoxy and other covering of the SDD PCB). This test should be conducted with the new version of the light shield, that incorporates changed screw position and a slightly altered routing of the o-ring sealing groove

to accommodate the new electrical connector with guiding posts as briefly mentioned in subsection 3.2.2.

- Test of the foil:
  (1) Verification of the calculated X-ray permeability.
  (2) Test in the final assembled setup as part of the onion-approach for the overall shielding against optical photons.

- Temperature tests:
  (1) Behavior of SDD glue joint at heating/cooling (glue: Epotec 920FL),
  (2) Fot the cold temperatures as present in the eclipse phases: Occurrence and impact of condensation of remaining humidity inside the light shield volume or the 1U-case.

- Verification of a fast enough light shield depressurization of the meander to exclude that small tube effects slow down the dynamics of the outflowing gas too much.

Appendix A: Mechanical Drawings

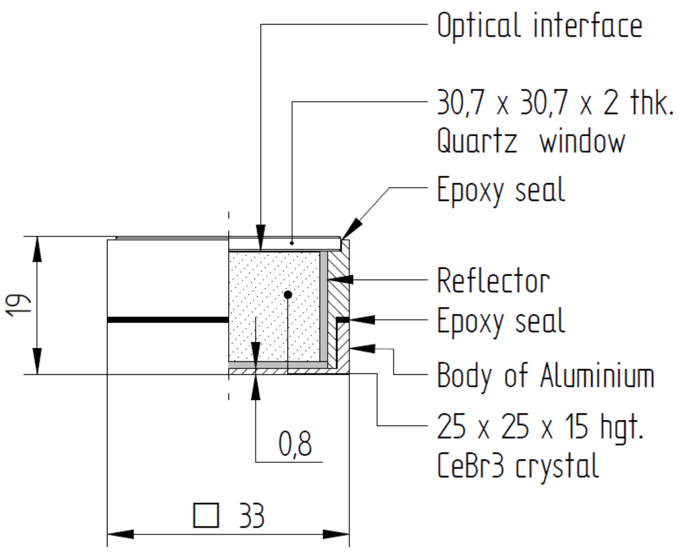

Figure 1: *Technical drawing of the housing, that protects the hygroscopic* $CeBr_3$, *as provided by the company SCIONIX.*

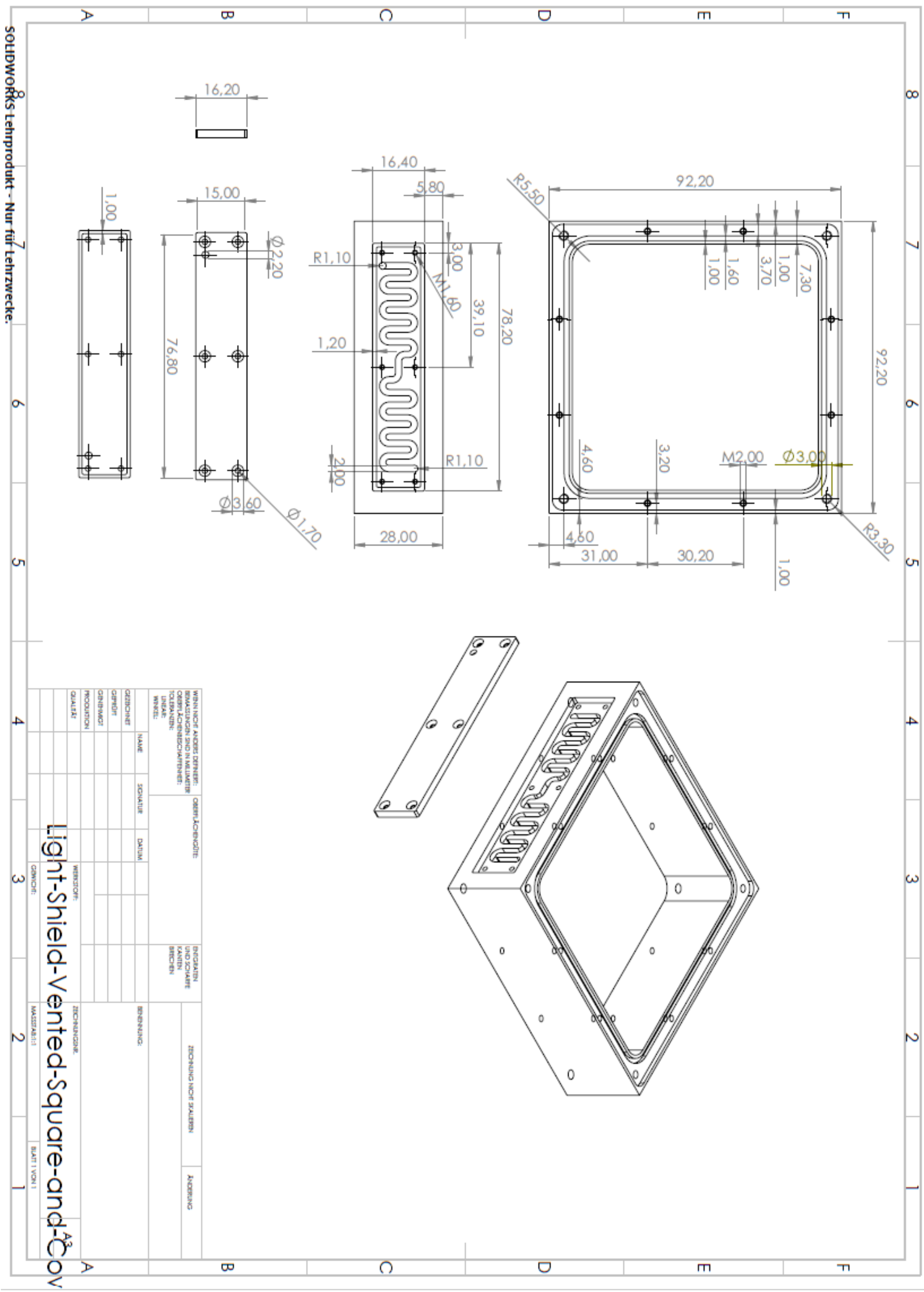

Figure 2: *Technical drawing of the interface with the o-ring interface as produced and tested in subsection 4.4.6*

Bibliography

[1] Matthias Meier. "TRISTAN Fly High - Design Studies for a CubeSat Compton Telescope." MA thesis. Technical University of Munich, 2019.

[2] Jérôme Rodriguez et al. "Spectral state dependence of the 0.4–2 MeV polarized emission in Cygnus X-1 seen with INTEGRAL/IBIS, and links with the AMI radio data." In: *The Astrophysical Journal* 807.1 (2015), p. 17. DOI: 10.1088/0004-637X/807/1/17.

[3] Shuang-Nan Zhang. "Black hole binaries and microquasars." In: *Frontiers of Physics* 8.6 (2013), pp. 630–660.

[4] S Bowyer et al. "Cosmic X-ray sources." In: *Science* 147.3656 (1965), pp. 394–398.

[5] B Louise Webster and Paul Murdin. "Cygnus X-1 — a Spectroscopic Binary with a Heavy Companion?" In: *Nature* 235.5332 (1972), pp. 37–38.

[6] Mark J. Reid et al. "The Trigonometric Parallax of Cygnus X-1." In: *The Astrophysical Journal* 742.2 (Nov. 2011), p. 83. DOI: 10.1088/0004-637x/742/2/83.

[7] J. Ziółkowski. "Determination of the masses of the components of the HDE 226868/Cyg X-1 binary system." In: *Monthly Notices of the Royal Astronomical Society: Letters* 440.1 (Feb. 2014), pp. L61–L65. ISSN: 1745-3925. DOI: 10.1093/mnrasl/slu002.

[8] J. LaSala et al. "The orbital period of HDE 226868/Cyg X-1." In: *Monthly Notices of the Royal Astronomical Society* 301.1 (Nov. 1998), pp. 285–288. ISSN: 0035-8711. DOI: 10.1046/j.1365-8711.1998.02064.x.

[9] T.M. Belloni. "States and Transitions in Black Hole Binaries." In: *The Jet Paradigm: From Microquasars to Quasars*. Ed. by Tomaso Belloni. Berlin, Heidelberg: Springer, 2010, pp. 53–84. ISBN: 978-3-540-76937-8. DOI: 10.1007/978-3-540-76937-8_3.

[10] Marek Gierliński et al. "Radiation mechanisms and geometry of Cygnus X-1 in the soft state." In: *Monthly Notices of the Royal Astronomical Society* 309.2 (1999), pp. 496–512.

[11] Jörn Wilms et al. "Long term variability of Cygnus X-1-IV. Spectral evolution 1999–2004." In: *Astronomy & Astrophysics* 447.1 (2006), pp. 245–261. DOI: 10.1051/0004-6361:20053938.

[12] V Grinberg et al. "Long term variability of Cygnus X-1-V. State definitions with all sky monitors." In: *Astronomy & Astrophysics* 554 (2013), A88.

[13] Juri Sugimoto et al. "MAXI observations of long-term variations of Cygnus X-1 in the low/hard and the high/soft states." In: *PASJ* 68, S17 (June 2016), S17. DOI: 10.1093/pasj/psw004. arXiv: 1601.02740 [astro-ph.HE].

[14] Michael A Nowak et al. "Rossi X-ray timing explorer observation of Cygnus X-1. II. Timing analysis." In: *The Astrophysical Journal* 510.2 (1999), p. 874.

[15] Thomas Gleissner et al. "Long term variability of Cyg X-1-II. The rms-flux relation." In: *Astronomy & Astrophysics* 414.3 (2004), pp. 1091–1104.

[16] NASA Official: Phil Newman. *About RXTE. The PCA*. https://heasarc.gsfc.nasa.gov/docs/xte/learning_center/pca.html. 2011.

[17] Floriane Cangemi et al. *High energy spectral study of the black hole Cygnus X-1 with INTEGRAL*. 2018. DOI: https://doi.org/10.48550. URL: https://arxiv.org/abs/1810.12049.

[18] Philippe Laurent and Lev Titarchuk. "The converging inflow spectrum is an intrinsic signature for a black hole: Monte Carlo simulations of Comptonization on free-falling electrons." In: *The Astrophysical Journal* 511.1 (1999), p. 289. DOI: 10.1086/306683.

[19] RP Fender, J Homan, and TM Belloni. "Jets from black hole X–ray binaries: testing, refining and extending empirical models for the coupling to X–rays." In: *Monthly Notices of the Royal Astronomical Society* 396.3 (2009), pp. 1370–1382.

[20] Mark L McConnell et al. "The soft gamma-ray spectral variability of Cygnus X-1." In: *The Astrophysical Journal* 572.2 (2002), p. 984.

[21] Philippe Laurent et al. "Polarized gamma-ray emission from the galactic black hole Cygnus X-1." In: *Science* 332.6028 (2011), pp. 438–439.

[22] Cynthia Glas. "Background studies for the ComPol Cube-Satellite." MA thesis. Technical University of Munich, 2022.

[23] NASA Science Official: Neil Gehrels. *The CGRO Mission (1991 - 2000) - High Energy Astrophysics Science Archive Research Center*. https://heasarc.gsfc.nasa.gov/docs/cgro/. 2016.

[24] European Space Agency. *Official INTEGRAL Website*. https://www.cosmos.esa.int/web/integral/. Including Sub-pages 'Mission Overview' and 'Instruments'. Accessed: May 2022. 2022.

[25] Alicia Johnstone. *CubeSat Design Specification (1U – 12U) Rev 14.1*. Tech. rep. San Luis Obispo, CA: California Polytechnic State University (Cal Poly), 2022. URL: https://static1.squarespace.com/static/5418c831e4b0fa4ecac1bacd/t/62193b7fc9e72e0053f00910/1645820809779/CDS+REV14_1+2022-02-09.pdf.

[26] Arash Mehrparvar. *CubeSat Design Specification (CDS) REV 13*. Tech. rep. San Luis Obispo, CA: California Polytechnic State University (Cal Poly), 2022. URL: https://explorers.larc.nasa.gov/APMIDEX2016/MO/pdf_files/11-cds_rev13_final2.pdf.

[27] RM Curado da Silva et al. "CIPHER, a polarimeter telescope concept for hard X-ray astronomy." In: *Experimental Astronomy* 15.1 (2003), pp. 45–65.

[28] A Coleman and M McConnell. "COMPTEL Search for Gamma-Ray Polarization in Gamma-Ray Bursts and Solar Flares." In: *American Astronomical Society Meeting Abstracts # 235*. Vol. 235. 2020, pp. 206–04.

[29] Marco Agnan, Jordan Vannitsen, and Yun-Peng Tsai. *Feasibility Study for the COMPOL Mission*. ODYSSEUS Space Inc. 2018.

[30] *Technology Readiness Levels Handbook for Space Applications*. Tech. rep. 1.6 (TEC-SHS/5551/MG/ap). ESA, 2008. URL: https://artes.esa.int/sites/default/files/TRL_Handbook.pdf.

[31] John C Mankins (Advanced Concepts Office). *Technology readiness levels. A White Paper*. Tech. rep. Office of Space Access and Technology, NASA, 1995. URL: https://spacese.spacegrant.org/SEModules/Technology%5C%20Mods/Mankins_trl.pdf.

[32] Tatehiro Mihara et al. "Gas Slit Camera (GSC) onboard MAXI on ISS." In: *Publications of the Astronomical Society of Japan* 63.sp3 (Nov. 2011), S623–S634. ISSN: 0004-6264. DOI: 10.1093/pasj/63.sp3.S623.

[33] Hiroshi Tomida et al. "Solid-State Slit Camera (SSC) Aboard MAXI." In: *Publications of the Astronomical Society of Japan* 63.2 (Apr. 2011), pp. 397–405. ISSN: 0004-6264. DOI: 10.1093/pasj/63.2.397.

[34] COSI Team. *COSI: The Compton Spectrometer and Imager - Compton Telescope Basics*. https://cosi.ssl.berkeley.edu/instrument/design/. 2022.

[35] S.M. Seltzer M.J. Berger J.H. Hubbell. *XCOM: Photon Cross Section Database (Version 1.5)*. https://dx.doi.org/10.18434/T48G6X. National Institute of Standards and Technology, Gaithersburg, MD. 2010.

[36] Si Chen et al. "Measurement of deeply virtual compton scattering with a polarized-proton target." In: *Physical review letters* 97.7 (2006), p. 072002.

[37] Wikimedia Commons contributor 'Napy1kenobi'. *File:Compton camera Principle.svg — Wikimedia Commons, the free media repository*. 2020. URL: https://commons.wikimedia.org/w/index.php?title=File:Compton_camera_Principle.svg&oldid=520784453.

[38] Sascha Trippe. "Polarization and polarimetry: a review." In: *arXiv preprint arXiv:1401.1911* (2014).

[39] Andreas Christian Zoglauer. "First Light for the Next Generation of Compton and Pair Telescopes." Dissertation. München: Technische Universität München, 2005. URL: https://mediatum.ub.tum.de/603105.

[40] Tod E Strohmayer and Tim R Kallman. "On the statistical analysis of X-ray polarization measurements." In: *The Astrophysical Journal* 773.2 (2013), p. 103.

[41] Matteo Gugiatti. "Presentation: Everything you wanted to ask about SDDs and you never had the courage to." 2021.

[42] Susanne Mertens et al. "A novel detector system for KATRIN to search for keV-scale sterile neutrinos." In: *Journal of Physics G: Nuclear and Particle Physics* 46.6 (2019), p. 065203.

[43] S Mertens et al. "Sensitivity of next-generation tritium beta-decay experiments for keV-scale sterile neutrinos." In: *Journal of Cosmology and Astroparticle Physics* 2015.02 (2015), p. 020.

[44] Martin Descher. "Presentation: Introduction to Digitizers. And their Application for TRISTAN." 2021.

[45] WM Higgins et al. "Crystal growth of large diameter LaBr3: Ce and CeBr3." In: *Journal of Crystal Growth* 310.7-9 (2008), pp. 2085–2089. DOI: 10.1016/j.jcrysgro.2007.12.041.

[46] Adrien Laviron et al. "Optimization of CeBr3 position-sensitive calorimeter module." In: *Nuclear Instruments and Methods in Physics Research Section A: Accelerators, Spectrometers, Detectors and Associated Equipment* 1007 (2021), p. 165379. ISSN: 0168-9002. DOI: https://doi.org/10.1016/j.nima.2021.165379. URL: https://www.sciencedirect.com/science/article/pii/S0168900221003636.

[47] Aleksandar Gostojic Gostojić. "Development of a Compton Telescope with 3D Imaging Calorimeter for Gamma-Ray Astronomy." Theses. Université Paris Saclay (COmUE), Apr. 2016. URL: https://tel.archives-ouvertes.fr/tel-01333558.

[48] Solid State Devision. *MPPC: Multi Photon Pixel Counter. S14161-4050HS-06 Datassheet*. HAMAMATSU PHOTONICS. 2020. URL: https://www.hamamatsu.com/eu/en/product/optical-sensors/mppc/mppc_mppc-array/S14161-4050HS-06.html.

[49] *Introduction to the Silicon Photomultiplier*. Tech. rep. Rev. 6.0. sensL - sense ligh, 2017. URL: https://sensl.com/downloads/ds/TN%20-%20Intro%20to%20SPM%20Tech.pdf.

[50] Slawomir S Piatek. "Physics and Operation of an MPPC." In: *Hamamatsu Corporation and New Jersey Institute of Technology* (2014). URL: https://zeus.phys.uconn.edu/halld/siliconPM/MPPC_physics_of_operation_2014.pdf.

[51] AIRBUS. *Bartolomeo. Easy access to low-earth orbit*. https://www.airbus.com/en/products-services/space/in-space-infrastructure/bartolomeo. 2021.

[52] JH Hubbell and SM Seltzer. "X-Ray Mass Attenuation Coefficients. NIST standard reference database 126." In: *Gaithersburg, MD: National Institute of Standards and Technology* (1996). DOI: 10.18434/T4D01F.

[53] AIRBUS. *Bartolomeo Datasheet*. https://www.airbus.com/sites/g/files/jlcbta136/files/2021-10/202011_Bartolomeo_Datasheet_fin.pdf. 2021.

[54] Goodfellow. *Product Information on Polyethylene Terephthalate (PET)*. https://www.goodfellow.com/de/en-us/information/larger-quantities/513/536/polymers/polyethylene-terephthalate-pet. 2020.

[55] Goodfellow. *Product Information on Polycarbonat (PC)*. https://www.goodfellow.com/de/en-us/information/larger-quantities/513/530/polymers/polycarbonate-pc. 2020.

[56] Mikhail N. Polyanskiy. *Refractive index database*. https://refractiveindex.info. 2021.

[57] H.-J. Hagemann, W. Gudat, and C. Kunz. "Optical constants from the far infrared to the x-ray region: Mg, Al, Cu, Ag, Au, Bi, C, and Al2O3." In: *J. Opt. Soc. Am.* 65.6 (June 1975), pp. 742–744. DOI: 10.1364/JOSA.65.000742. URL: http://opg.optica.org/abstract.cfm?URI=josa-65-6-742.

[58] Private communication about NASA Safety Regulations with Martin Losekamm. 2021.

[59] Larry Chesterfield. *Surface Roughness Before and After Anodizing*. https://www.pfonline.com/articles/surface-roughness-before-and-after-anodizing. 2002.

[60] *Product Data Sheet: SiPM – Silicon Photomultiplier PM3325-WB-B0*. KETEK GmbH. URL: https://www.ketek.net/wp-content/uploads/2017/09/KETEK-PM3325-WB-B0-Datasheet.pdf.

[61] Stack Exchange Ask Different user's *ecnepsnai* answer about iPhone 4 lamp to the issue: *iPhone 5 flashlight strength*. https://apple.stackexchange.com/questions/129388. 2014.

[62] Quora user's *Chiharu Inukai* answer about iPhone 6 to question: *How bright is the LED flashlight on the iPhone?* https://www.quora.com/How-bright-is-the-LED-flashlight-on-the-iPhone. 2019.

[63] *User Manual UM5960. CoMPASS Multiparametric DAQ Software for Physics Applications - Rev. 18.* CAEN S.p.A. 2022.

[64] alphys. *LED-Strahler weiß.* https://alphys.de/produktreihe-led/led-strahler-weiss. 2020.

[65] *Product Data Sheet: SiPM – Silicon Photomultiplier PM3325-WB-D0, Rev. 2020-A.* KETEK GmbH. 2020. URL: https://www.ketek.net/wp-content/uploads/2018/12/KETEK-PM3325-WB-D0-Datasheet.pdf.

[66] TE Connectivity. *Datasheet: 10K3A1AM SERIES VI Thermistor.* https://www.te.com/usa-en/product-GA10K3A1AM.html. 2015.

[67] Manuel Burkart. *Mechanical and Electrical Design and Experimental Validation of an LED based Solar Simulator for CubeSat Environmental Testings (Term Paper: RT SA 2014/NN).* Institute of Astronautics Database. 2014.

Acknowledgements

I would like to say a big THANK YOU to all the amazing people that helped me with this thesis:

- Susanne, thank you for the opportunity to conduct a thesis on the edge between astrophysics, particle physics and aerospace. I could not have asked for a better project! Thank you for joining in most of the internal ComPol meetings and for giving me honest feedback!
- Martin, you were always around when I had questions. You introduced me to the TUM workshop and how to get parts. Talking with you about the SiPM measurement was a great help. Thank you especially for organizing the solar simulator. You have contributed a great deal to the success of this thesis.
- Mike, thank you for the times that we met and for your feedback.
- Matthias, for the enjoyable discussion about Compton telescopes, multi-gauss fitting, matplotlib and much more. You are explaining things easy and well.
- Alexander Sedlak, for 3D-printing my parts in basically no time
- Carina Schlammer, for finding the right laser-cutting settings for the protection foil and providing me with a handy storage case
- Everyone who helped me correcting my writing, especially Mark.
- Mein liebster Andreas, du warst mein treuster und zuverlässigster Korrekturleser. Danke, dass ich auf dich zählen konnte! Deine oft erfrischenen Kommentare waren ein Segen im Endspurt der Korrekturphase, haben sie mich doch oft zum Schmunzeln gebracht.
- My parents, dafür, dass ihr mir den Rücken freigehalten habt und mich immer unterstützt hab. Ihr habt mir auch bei physikalischen Überlegungen geduldig zugehört, und mir allein dadurch schon oft geholfen. DANKE! Insbesondere will ich auch meiner Mama danken, die mir mit vielen Feeback-Kommentaren geholfen hat. Dadurch hast du meine Arbeit so viel besser gemacht!
- All members of the KATRIN/TRISTAN group - for the welcoming positive atmosphere in the rare occasions I was not in home office, but at MPP.